Prenatal low-dose methylmercury (MeHg) exposure causes premature neuronal differentiation and autism spectrum disorder (ASD)-like behaviours in a rodent model

Allison Loan

A thesis submitted in partial fulfillment of the requirements for the

Doctorate in Philosophy degree in Biology

Department of Biology

Faculty of Science

University of Ottawa

Abstract

Methylmercury (MeHg) is a global pollutant that can elicit a range of adverse health effects in both humans and wildlife populations. Humans are often exposed to MeHg through the consumption of contaminated seafood. Developing fetuses are especially susceptible to the effects of MeHg as it can cross the blood-brain barrier and the placenta. At high doses *in utero* MeHg causes developmental disorders and congenital disabilities, but long-term low-dose effects are still not fully known. Using a culture model of cerebral cortex development, our lab has shown that low-dose MeHg promotes premature neuronal differentiation. Autism spectrum disorder (ASD) has been associated with prenatal MeHg exposure and is correlated with neuronal overproduction, but a cause-effect relationship has not been shown. In this thesis, I aim to test the hypothesis that prenatal exposure to low-dose MeHg can cause ASD-like symptoms in the offspring following premature neuronal differentiation. My results showed that adult mice prenatally exposed to MeHg exhibited key ASD characteristics including impaired communication, reduced sociability, and increased restrictive repetitive behaviours. Furthermore, I explored the underlying cellular and molecular mechanism that promotes premature neuronal differentiation caused by prenatal MeHg exposure. To reverse the MeHg-induced premature neuronal differentiation, I utilized metformin, an FDA-approved diabetes drug. Overall, these findings provide insights into the toxicology of MeHg and its relationship with ASD etiology, including the underlying mechanism, and a potential therapeutic strategy.

Acknowledgments

First, I would like to thank my supervisors, Dr. Laurie Chan and Dr. Jing Wang, my TAC members, and all the past and current Wang and Chan lab members. Second, I want to thank my parents, Lorna Wiens, and Aleric Loan. I could not have done this without your love and support. Finally, I would like to thank my two cats, Chaos and Doom, who were instrumental in the completion of this Ph.D.

Table of contents

List of abbreviations

ADHD	Attention Deficit/Hyperactivity Disorder
ASD	Autism Spectrum Disorder
ASI	Adult Social Interaction
ASK1	Apoptosis Signal-Regulating Kinase-1
BBB	Blood-Brain Barrier
BSA	Bovine Serum Albumin
BTBR	BTBR T+Itpr3tf/J
Ca^{2+}	Calcium
CBP	Creb Binding Protein
cDNA	Complementary DNA
cGE	Caudal Ganglionic Eminence
CI	Confidence Interval
CNS	Central Nervous System
CNV	Copy Number Variation
CP	Cortical Plate
CREB	cAMP Response Element-Binding Protein
DAPI	4′,6-Diamidino-2-Phenylindole
DCX^{+}	Doublecortin-Positive
DG	Dentate Gyrus
DZ	Dizygotic
E	Embryonic Day
E/I	Excitation and Inhibition

FC	Fear Conditioning
FG	Fusiform Gyrus
FGF2	Fibroblast Growth Factor 2
GABA	Gamma-aminobutyric acid
GAPDH	Glyceraldehyde-3-Phosphate Dehydrogenase
GCL	Glutamate–Cysteine Ligase
GE	Ganglionic Eminences
GPx	Glutathione Peroxidase
GSH	Glutathione
GSSG	Oxidized Glutathione
GW	Gestational Week
H2O2	Hydrogen Peroxide
HBSS	Hanks' Balanced Salt Solution
hESCs	Human Embryonic Stem Cell
Hg	Mercury
Hg^{0}	Elemental Mercury
Hg^{1+}	Mercurous Mercury
Hg^{2+}	Mercuric Mercury
HgSe	Mercury Selenide
HO-1	Heme Oxygenase-1
IP	Intermediate Progenitor
IP^{+}	Intermediate Progenitor-Positive
IQ	Intelligence Quotient

iSVZ	Inner-Subventricular Zone
IZ	Intermediate Zone
JNK	C-Jun N-Terminal Kinase
Keap1	Kelch-Like Ech-Associated Protein 1
KID	Kinase-inducible domain
KIX	Kinase-inducible domain interacting domain
LAT	L-Type Large Neutral Amino Acid Transporter Systems
M.O.M.	Mouse on Mouse
MAPK	Mitogen-Activated Protein Kinases
MAPK	P38 Mitogen-Activated Protein Kinases
MeHg	Methylmercury
mGE	Medial Ganglionic Eminence
MIA	Maternal Immune Activation
Mn-SOD	Manganese-Superoxide Dismutase
mPFC	Medial Prefrontal Cortex
MWM	Morris Water Maze
MZ	Marginal Zone
MZ	Monozygotic
N^+	Neuronal-Positive
NADPH	Nicotinamide Adenine Dinucleotide Phosphate
NE	Neuroepithelial Cell
NGS	Normal Goat Serum
Nlgn	Neuroligins

NMDA	N-Methyl-D-Aspartate
NOR	Novel Object Recognition
Nrf2	Nuclear Factor Erythroid 2-Related Factor 2
Nrxn	Neurexins
NSC	Neural Stem/Progenitor Cell
O_{2^-}	Superoxide Anion
OCD	Obsessive-Compulsive Disorder
OCT	Optimal Cutting Temperature Compound
OCT1	Organic Cation Transporter 1
OFC	Orbital Frontal Cortex
OPC	Oligodendrocyte Progenitor
oRGP	Outer Radial Glial Precursor
oSVZ	Outer-Subventricular Zone
P	Postnatal Day
p-S133 CREB	CREB Phosphorylation at Ser133
p-S436 CBP	CBP Phosphorylation at Ser436
PBS	Phosphate-Buffered Saline
PBST	1X PBS with 0.3% Triton X-100
PCA	Principal Component Analysis
PFA	Paraformaldehyde
PLA	Proximity Ligation Assay
PLO	Poly-L-Ornithine
POR	Prevalence Odds Ratio

PMAT	Plasma Membrane Monoamine Transporter
PMSF	Phenylmethylsulfonyl Fluoride
PP	Preplate
PVDF	Polyvinylidene Difluoride
RG^+	Radial Glial-Positive
RGP	Radial Glial Precursor
RGP1	Radial Glial Precursor 1
RGP2	Radial Glial Precursor 2
ROS	Reactive Oxygen Species
RT-qPCR	Real-Time Quantitative Polymerase Chain Reaction
scRNA-seq	Single-Cell RNA-Sequencing
SDS-PAGE	Sodium Dodecyl Sulfate–Polyacrylamide Gel Electrophoresis
Se	Selenium
Sec	Selenocysteine
selenol	Selenohydryl
SEM	Standard Error Of The Mean
SeMet	Selenomethionine
SGZ	Subgranular Zone
SNP	Single Nucleotide Polymorphism
SNPC	Short Neural Precursor Cell
SNV	Single Nucleotide Variant
SP	Subplate
STS	Superior Temporal Sulcus

SVZ	Subventricular Zone
SVZ/IZ	Subventricular Zone/Intermediate Zone
T2D	Type 2 Diabetes
TBS-T	Tris-Buffered Saline + 0.1% Tween-20
TDI	Tolerable Daily Intake
thiol	Sulfhydryl
tRGP	Truncated Radial Glial Precursor
Trx	Thioredoxin
TrxR	Thioredoxin Reductase
Tubb3	βIII-Tubulin
UMAP	Uniform Manifold Approximation And Projection
USV	Ultrasonic Vocalization
VPA	Valproic Acid
vRGP	Ventricular Radial Glial Precursor
VZ	Ventricular Zone
WHO	World Health Organization

List of figures

List of tables

Author contributions

A.L. performed all behavioral testing, embryonic cortical precursor culture, immunocytochemistry, immunohistochemistry, PLA assay, and qPCR. J.L. and A.L. performed experiments related to embryonic *in vivo* animal work including MeHg drinking water preparation, tissue preparation, sectioning, and immunohistochemistry. A.L., J.L. and D.C. performed multiplexing single-cell RNA-seq experiments. D.C. and A.L. performed bioinformatic analysis for single-cell RNA-seq dataset. C.K. performed USV analysis and grooming analysis. B.V. provided the resource for multiplexing single-cell RNA-seq. J.W. and H.M.C. contributed to the conceptualization, funding, and project management.

Chapter 1: Introduction

1.1. Mercury (Hg) in the environment

According to the World Health Organization (WHO), mercury (Hg) is considered one of the top ten chemicals of major public health concern [1]. There are three forms of Hg: elemental (Hg^0), inorganic (Hg^{1+}, mercurous mercury, and Hg^{2+} mercuric mercury), and organic Hg. Organic Hg occurs when Hg is combined with carbon. Types of organic Hg include methylmercury (MeHg/CH_3Hg^+), ethylmercury (EHg/$C_2H_5Hg^{1+}$), and dimethylmercury (C_2H_6Hg). Hg^0 is present in the environment naturally and is released from volcanoes, weathering rocks, and forest fires. Hg is also commonly released by anthropogenic sources such as coal burning and mining. Heating Hg^0 results in a colourless, odourless gas that is then transported into the atmosphere [2]. In the atmosphere, Hg^0 is photo-oxidized to form Hg^{2+}. Photo-oxidation of Hg^0 is a slow process that results in atmospheric circulation and long-range transportation of Hg^0 [3]. Hg^{2+} is less volatile and is deposited back onto the earth's surface via wet and dry deposition (Figure 1.1A) [4]. In aquatic environments, Hg^{2+} is methylated by microorganisms to form the more toxic, MeHg (Figure 1.1B) [5].

The most common source of exposure to organic Hg is via MeHg. Human exposure to MeHg most commonly occurs through the ingestion of contaminated food such as fish, shellfish, and marine mammals [6,7].

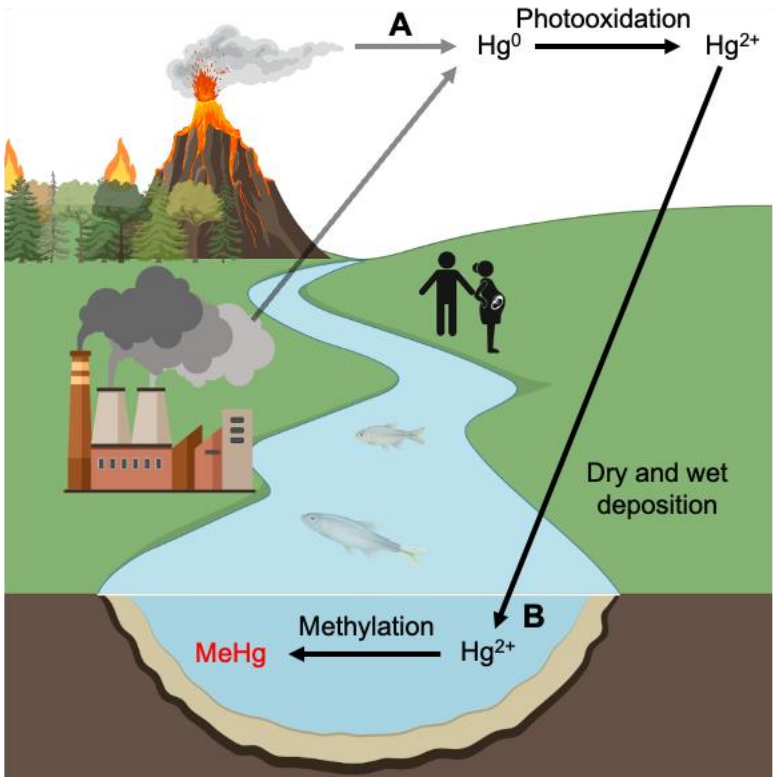

Figure 1.1. Production of MeHg in the environment.
(A) Hg^0 is released into the environment from natural and anthropogenic sources. Hg^0 is then photo-oxidized in the atmosphere to form Hg^{2+}, which is deposited onto the earth's surface. (B) Hg^{2+} is methylated by microorganisms to form MeHg. MeHg then bioaccumulates and biomagnifies in aquatic organisms. Abbreviation: Hg^0, elemental mercury; Hg^{2+}, mercuric mercury; MeHg, methylmercury. Created with BioRender.com

1.2. MeHg absorption, distribution, metabolism, and excretion

1.2.1. Absorption

Routes of exposure for MeHg include dermal, inhalation, and ingestion. However, data on dermal and inhalation exposure is lacking. Ingestion of MeHg is the most common and most studied route of exposure. Approximately 90-95% of MeHg is absorbed by the gastrointestinal tract through passive diffusion or L-type neutral amino acid transporters (LAT) into intestinal epithelial cells [7,8]. Multiple factors affect the bioaccessibility of Hg. Cooking methods like boiling and frying fish prior to consumption were shown to reduce Hg bioaccessibility by 40% and 60%, compared to raw fish [9]. Other factors that affect bioaccessibility are fat content [10,11], co-ingestion of foods such as black coffee, tea, or garlic [9,12], and the presence of selenium (Se) [13–16].

1.2.2. Distribution

The positive Hg group within MeHg is essential for its distribution within the body. This positive Hg group makes MeHg readily combine with anions. MeHg commonly forms bonds with sulfhydryl (thiol) groups and interacts readily with cysteine thiol groups on erythrocytes, glutathione (GSH), and albumin. Hg also forms bonds with selenohydryl (selenol) groups and, as a result, interacts readily with selenol groups on selenomethionine (SeMet), selenocysteine (Sec), and selenoproteins. MeHg chloride is lipophilic, having a water solubility of only 0.100g/L in water at room temperature. MeHg has a molecular weight of 215.63 g/mol and a logP of 0.49, making it slightly lipophilic [7]. Due to its lipophilicity, MeHg takes approximately 20-30 h to distribute into the bloodstream, at which point it is transported by erythrocytes [17]. Within erythrocytes, MeHg binds to cysteine residues on the α- and β-chain of hemoglobin [7,18]. MeHg can also be somewhat distributed in the plasma bound to proteins such as albumin (Figure 1.2A)

[19–21]. A portion of MeHg from the bloodstream is taken up by the hair and nails making it a useful non-invasive biomarker that reflects exposure over time [22,23].

The MeHg-cysteine complex mimics the amino acid L-methionine, an endogenous substrate of LAT. This allows MeHg-cysteine to target endothelial cells of the blood-brain barrier (BBB) and enter the central nervous system (CNS) via LAT1/2 transporters [18,24]. Within the CNS, the amount of MeHg that accumulates is brain region-dependent. A study using adult female guinea pigs found that after 71 days of exposure to radiolabeled MeHg, the brain regions with the least to most MeHg were: the cerebellum, the hypothalamus, the calcarine cortex, the frontal lobe, the occipital lobe, and the caudate nucleus [25].

MeHg is also transported through the placenta to target the fetal CNS and influence neurodevelopment. To determine the mechanism that facilitates placental transport, pregnant rats were administered MeHg on embryonic day 18 (E18), and fetal blood was collected for analysis. Researchers determined that MeHg transport was suppressed by the co-injection of L-methionine. This suggests that MeHg is transported into fetal blood via the MeHg-cysteine complex and can be suppressed by the administration of competitive L-methionine (Figure 1.2B) [26].

After birth, MeHg continues to pass from the mother to the infant through breast milk [27]. The mechanism that facilitates MeHg transfer in breast milk is poorly understood. In both CD-1 mice and humans, MeHg was transferred from the plasma to the breast milk as a MeHg-albumin complex [19]. Therefore, breast milk represents another source of exposure for newborns and another method of excretion for mothers.

1.2.3. Metabolism

Metabolism of MeHg occurs by demethylating MeHg to Hg^{2+}. The specific enzymes that facilitate this are unknown. Cytochrome P450 enzymes play an important role in metabolism and demethylation; however, in the mouse liver, cytochrome P450 is not involved [28]. Early studies have shown that MeHg is demethylated in the gastrointestinal tract by intestinal flora to Hg^{2+} (Figure 1.2F) [29,30]. A rodent study where mice were given a single dose of MeHg chloride showed that mice co-treated with antibiotics to reduce gut flora had retained more MeHg. Furthermore, mice not co-treated with antibiotics had more Hg^{2+} in the liver and the kidneys [30].

Early work in the human fetal liver conducted by Suzuki et al., (1984) found that 27-60% of total Hg was inorganic Hg. To confirm that demethylation takes place in the fetal liver they incubated 10^{-3}M MeHg with chopped fetal liver tissue *in vitro*. After 24 h, approximately 1% of the MeHg was demethylated, which confirms that demethylation takes place in the liver [31]. These results have been confirmed in the mouse [28] and dolphin liver [32], suggesting that the liver is a major source of demethylation (Figure 1.2E).

MeHg demethylation in the human [33] and monkey brain [34] is a very slow process (Figure 1.2C). Moreover, in the fetal brain, there is evidence that very little demethylation occurs [31]. Demethylation of MeHg to Hg^{2+} may also result in independent toxicity. At high doses, Hg^{2+} can result in kidney failure and gastrointestinal damage. Hg^{2+} is also less mobile, which prevents it from crossing the BBB [35]. Therefore, once MeHg is demethylated in the brain it may illicit independent damage.

1.2.4. Excretion

Approximately 90% of MeHg is excreted through the bile and feces, consistent with its slightly lipophilic nature [7]. MeHg is transported to the liver and the kidneys via the bloodstream

for excretion. Within hepatocytes of the liver, MeHg forms a complex with GSH which is hydrolyzed to MeHg-cysteine and demethylated to Hg^{2+}. MeHg-GSH from the liver is also partially circulated into the intestines via the bile through the process of enterohepatic circulation [36]. MeHg-GSH is hydrolyzed, releasing the MeHg-cysteine complex into the gastrointestinal tract. A portion of MeHg is demethylated by intestinal microflora to form Hg^{2+}, which is then excreted in the feces (Figure 1.2E-F).

Approximately 10% of MeHg is excreted in urine as Hg^{2+} [7]. MeHg-albumin complexes in the plasma are transferred to the kidneys where MeHg binds to GSH, at which point GSH is hydrolyzed to form MeHg-cysteine which is then excreted through the urine as Hg^{2+} (Figure 1.2D) [20]. The half-life of MeHg is difficult to assess due to variations in the method of assessment and inter-individual variability [37]. Overall, in the blood, where ~85% of Hg is MeHg, the approximate half-life is 44-50 days. In comparison, the whole-body half-life of total Hg, including demethylation, is approximately 70-96 days [7,38,39].

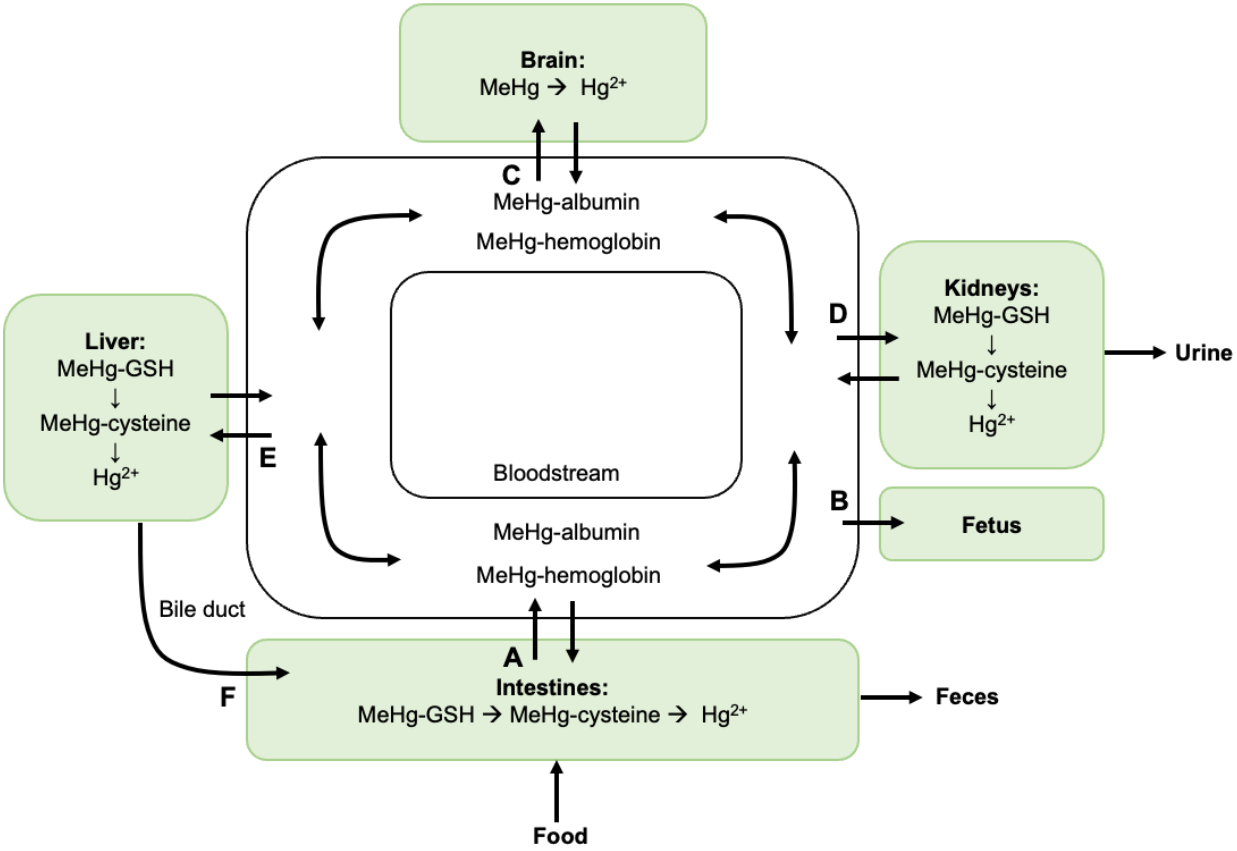

Figure 1.2. Absorption, distribution, metabolism, and excretion of MeHg.
(A) Once MeHg enters the gastrointestinal tract, it is transported by erythrocytes and plasma bound to hemoglobin and albumin, respectively. (B) MeHg-cysteine enters the placenta (C) and the brain. (D) MeHg is primarily transported into the kidneys by albumin, at which point it binds to GSH and is then hydrolyzed and demethylated to Hg^{2+}. Roughly 10% of the total body burden is eliminated by the urine. (E) In the liver, MeHg-GSH is hydrolyzed and partially demethylated to Hg^{2+}. MeHg-GSH is also partially recirculated into the intestines via the bile duct. (F) In the intestines, MeHg can be demethylated by the gut flora. Roughly 90% of MeHg is eliminated via feces. Abbreviation: Hg^{2+}, mercuric mercury; GSH, glutathione; MeHg, methylmercury.

1.3. At-risk populations

Human exposure to MeHg most commonly occurs through the ingestion of contaminated food such as fish and shellfish. Guidelines for tolerable daily intake (TDI) vary between agencies and populations. Based on research from the WHO conducted in 1972, the Canadian Bureau of Chemical Safety recommended a TDI of 0.47 micrograms per kilogram body weight per day (μg/kg BW/day) for adults. As further research on the neurodevelopmental consequences of fetal and infantile exposure to MeHg emerged, this TDI recommendation was lowered. Currently, Health Canada has a TDI of 0.2μg/kg BW/day for pregnant women and young children [35]. Other populations that are particularly susceptible to MeHg toxicity are those who consume large amounts of seafood, those who live in high latitudes, and those who live and work near gold mining facilities.

1.3.1. MeHg in seafood

Human ingestion of MeHg is particularly harmful due to bioaccumulation and biomagnification. Bioaccumulation is the gradual accumulation of a toxic agent that is consumed at a greater rate than can be degraded. MeHg accumulates to elicit neurotoxicity, teratogenic toxicity, and carcinogenicity and disrupts reproduction and cardiovascular health [7]. Biomagnification occurs when a toxin is accumulated in larger predatory organisms due to the consumption of other lower-order plants and animals. This makes MeHg particularly dangerous for humans due to their size, life expectancy, and position in the food chain [40].

In Canada, the maximum content of MeHg permitted within commercially available fish is currently 0.5ppm. Fish that contain over 0.2ppm include barracuda, marlin, sea bass, shark, swordfish, and types of tuna [35].

1.3.2. Long-range transport of Hg^0

Gaseous Hg^0 in the atmosphere has a long lifetime ranging from 6 months to 2 years [41]. This results in long-range atmospheric transport of Hg^0 to higher latitudes through tropospheric circulation patterns. Other major transport pathways are rivers and ocean currents.

In Arctic and Antarctic regions, during early spring, a sudden decrease in gaseous Hg^0 to form Hg^{2+} occurs. This is called an atmospheric Hg depletion event [3]. This large deposition of Hg^{2+} in polar aquatic environments results in enhanced production of MeHg [5]. As a result, Northern populations that consume fish or fish-eating mammals are at a higher risk of MeHg exposure. This is a very pertinent topic for Canadian health as Indigenous communities in Northern Canada are disproportionally more affected by MeHg exposure due to their location and traditional fish diet [42,43].

1.3.3. Gold mining

Hg^0 is commonly used during gold mining to collect small gold particles from sediment. Hg^0 and gold are combined to create an amalgam alloy which is then heated to separate the Hg^0 from the gold. Gaseous Hg^0 contaminates nearby waterways and is ultimately methylated into MeHg. Overall, this results in occupational exposure and the contamination of local fish populations. This most commonly occurs in artisanal and small-scale gold mining operations that have fewer health and safety regulations.

A recent study investigated MeHg exposure in Colombian communities with known local artisanal and small-scale gold mining operations. The average MeHg in the hair of non-amalgam burners was 0.71ppm, compared to amalgam burners, 2.3ppm [44]. This data demonstrates a clear occupational risk for amalgam burners.

1.4. The dose-dependent effect of MeHg on human health

1.4.1. High-dose adult exposure

The public health risks associated with high-dose MeHg exposure were highlighted by two major disasters. The first occurred in Minamata Japan in 1956 [45], and the second occurred in rural Iraq in 1971 [46]. Minamata was the first and most famous example of MeHg poisoning, and as a result, severe MeHg poisoning is now known as Minamata Disease. Local fish populations around the city of Minamata were contaminated by industrial wastewater from the Chisso Corporation. Consumption of the contaminated fish led to severe neurological disorders. Seafood in the bay was recorded to contain between 5.61 and 35.7ppm MeHg [47]. Comparatively, the maximum content of MeHg permitted within fish in Canada is currently 0.5ppm [35].

Symptoms of high-dose exposure included dysarthria, ataxia, muscle weakness, tremors, visual impairment, hearing loss, and in severe cases death [45]. A 1971 population-based survey in Minamata found that residents had impaired intelligence (prevalence odds ratio (POR) = 5.2, 95% confidence interval (CI): 3.7, 7.3) and increased mood and behavioural dysfunction (POR = 4.4, 95% CI: 2.9, 6.7) compared to the surrounding communities [48]. Based on data from the Ministry of Environment Japan, 2,955 individuals have been declared Minamata Disease patients [49].

The Iraq poison grain disaster occurred in 1971 when grain treated with a MeHg fungicide was mistakenly consumed as food by residents. People suffered similar symptoms to those observed in Minamata. Over 6,000 Iraqi citizens developed symptoms from the contaminated wheat [46]. Hair MeHg of residents ranged from 50 to 100ppm. For reference the government of Canada has determined that 10ppm is TDI for MeHg in maternal hair [35].

1.4.2. High-dose prenatal exposure

Developing fetuses are particularly susceptible to the effects of MeHg due to their rapid organ development. MeHg can cross the placenta and the blood-brain barrier to cause neurodevelopmental deficits in the developing fetus [26]. The consequences of high-dose MeHg exposure to developing fetuses have been extensively studied following the disasters in Japan and Iraq.

In Minamata, children prenatally exposed to high doses of MeHg experienced cerebral palsy, developmental delays, and microcephaly, while exposed mothers had only mild symptoms or were completely asymptomatic [50,51]. Similar symptoms were observed in a 5-year study on children exposed *in utero* during the Iraq disaster. Researchers reported that the children had hyperreflexia, motor delays, delayed mental development, and cerebral palsy [52].

1.4.3. Low-dose prenatal exposure

Following research on the disastrous effects of high-dose prenatal MeHg exposure, there was a push to understand the effects of moderate MeHg exposure from fish consumption during pregnancy. Epidemiological evidence has shown that low levels of prenatal MeHg exposure may cause neuro-cognitive effects during early childhood (3-7 years) [53–55], youth [56,57], and/or adulthood [58,59]. Longitudinal prospective epidemiological studies of interest for low-dose prenatal exposure are from the Republic of the Seychelle and Faroe Islands. These populations are highly dependent on fish consumption and, as a result, have been highly studied in relation to moderate MeHg exposure.

In the Seychelles Islands, a 66-month study of 711 children assessed the effects of prenatal MeHg on intelligence and development. The average maternal hair MeHg concentration was 6.8ppm. The researchers found no correlation between prenatal MeHg and developmental

abnormalities [60]. Similarly, a follow-up study on the children of the Seychelles Islands found no adverse effects on cognition at 19 years old [59]. In the Faroe Islands, 1022 children were assessed at 7 years old to determine the relationship between MeHg and development. Neurobehavioral examinations revealed dysfunctions in language, attention, and memory following prenatal MeHg exposure. The average maternal hair MeHg concentration was 4.27ppm, comparable to the Seychelle Islands [53]. The prenatally exposed children were then re-assessed at age 14 and age 22. Researchers found that the cognitive effects first discovered at age 7 persisted into adolescence and adulthood [57,58]. This study has been instrumental in determining TDI guidelines for pregnant women and young children.

In Canada, Inuit populations in Arctic Québec are highly dependent on fish as a part of their traditional diet [43]. Muckle et al., sought to investigate the relationship between prenatal MeHg exposure and behavioural problems in school-age children. Researchers found that prenatal MeHg exposure was associated with low intelligence quotient (IQ) [61] and attention deficit/hyperactivity disorder (ADHD) symptomology [62]. Overall, the studies conducted in the Seychelles and those conducted in Canada and the Faroe Islands are contradictory, and the long-term effects of low-dose MeHg exposure during pregnancy remains elusive.

1.5. The cerebral cortex

Neuroepithelial cells (NEs) form the neural plate, which closes the neural tube. The neural tube then subdivides into three primary vesicles: the forebrain, the midbrain, and the hindbrain. The hindbrain then further divides into the myelencephalon and metencephalon, while the forebrain further divides into the telencephalon and diencephalon (Figure 1.3) [63]. The ventral telencephalon includes the ganglionic eminences (GE), where gamma-aminobutyric acid (GABA)ergic interneurons originate [64]. The dorsal telencephalon then gives rise to the cerebral

cortex [63]. During development, the preplate (PP) is the first stage in corticogenesis. The PP then separates into two components, 1) the marginal zone (MZ), which contains Cajal-Retzius cells and 2) the subplate (SP). Four additional cortical layers exist during both human and mouse embryogenesis. These are the ventricular zone (VZ), the subventricular zone (SVZ), the intermediate zone (IZ), and the cortical plate (CP) [65].

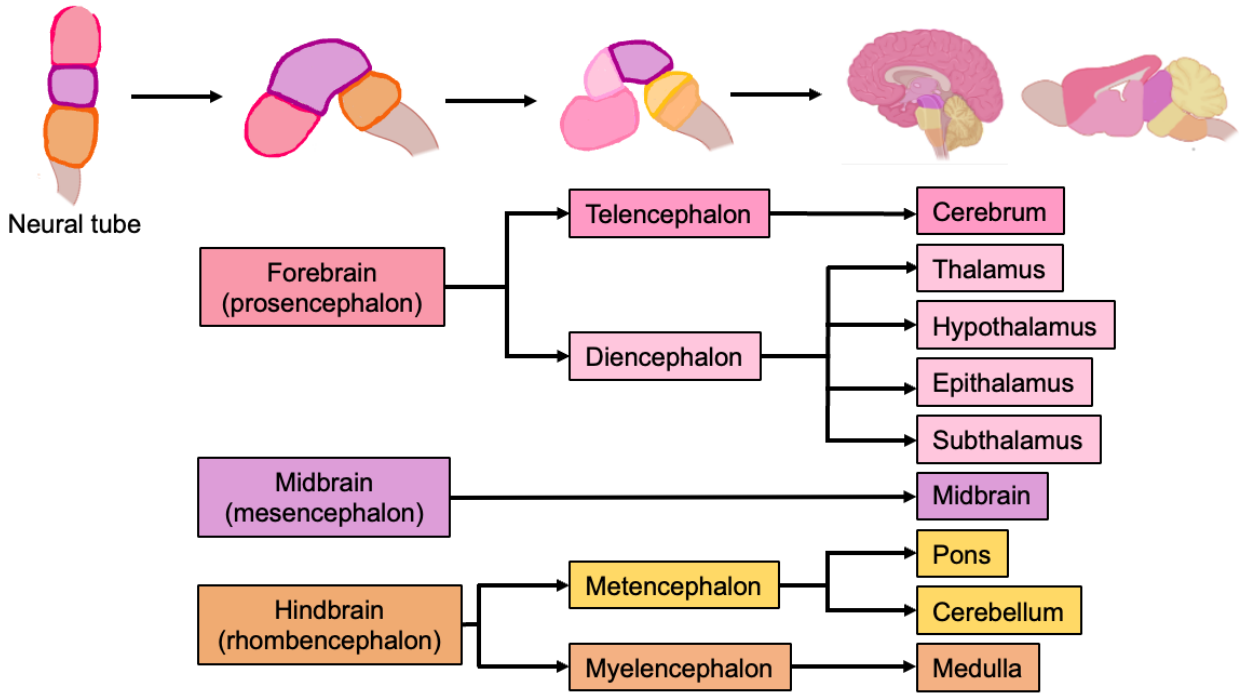

Figure 1.3. Schematic of neural tube and brain formation in embryo.

NEs are the earliest type of neural stem/progenitor cells (NSCs) (including NEs, radial glial precursors (RGPs), and intermediate progenitors (IPs)) in the cerebral cortex. NEs initially divide symmetrically to proliferate and expand the NSC pool. At ~E8 in mice [66] or gestational week 4-8 (~GW4-8) in humans [67,68], NEs start to divide asymmetrically to generate ventricular RGPs (vRGPs) (also called apical RGPs). These reside in the VZ of the cortex and begin to express glial markers while maintaining their bipolar morphology, with the apical endfoot facing the lateral ventricle, and basal process out, touching the pia surface. RGPs give rise to other progenitors in both humans and mice. First, short neural precursor cells (SNPCs) (also called apical IPs) reside in the VZ and lack basal attachment. SNPCs have limited neuronal production as they are only programmed to generate neurons via symmetric differentiation in mice and humans [68,69]. Second, outer RGPs (oRGPs) (also called basal RGPs) lack apical attachments and reside in the outer part of the SVZ (oSVZ) [68]. Third, basal IPs divide symmetrically and then detach from the apical surface to migrate radially to the SVZ to give rise to neurons. Finally, truncated RGPs (tRGPs) remain on the VZ surface and have discontinuous radial fibers [68]. In combination, these progenitors give rise to the cerebral cortex.

Mice and humans have a few major cortical neurodevelopmental differences which contribute to structural differences in the fully developed brain. First, humans have larger, highly folded gyrencephalic cortices, whereas mice have smooth lissencephalic cerebral cortices. Second, there are differences in cell type in the cerebral cortex. Unlike mice, oRGPs are especially abundant in humans and other mammals with complex gyrencephalic cortices. Finally, neuronal organization in rodents is less well-defined, and there is less evidence for the presence of columnar structures [70].

1.5.1. Cerebral cortex development in mice

In mice, at ~E10-11, vRGPs divide asymmetrically at the VZ surface to self-renew and generate projection neurons. Migrating immature neurons (neuroblasts) then detach from the apical surface to migrate radially out of the VZ through the IZ to form the PP [71,72].

As neurogenesis continues from ~E13-16, RGPs give rise to IPs which detach from the apical surface to migrate radially to the SVZ. IPs then divide symmetrically to give birth to two identical neurons. Newborn cortical neurons produced from RGPs or IPs migrate along the basal processes of RGPs. Earlier-born neurons form the deep layers of the CP (layers 5 and 6), and later-born neurons migrate outward past the deep layers to establish the superficial or upper layers (layers 2-4) glutamatergic pyramidal neurons in an inside-out manner. After migration, neurons undergo maturation, involving axon growth and synapse formation [70].

Gliogenesis starts at ~E17 and continues into early postnatal. Here, RGPs form astrocytes and oligodendrocyte progenitor cells (OPCs). These are then incorporated into the six layers of the cerebral cortex (Figure 1.4) [73].

1.5.2. Cerebral cortex development in humans

In humans, neurogenesis begins at ~GW5-7, at which point vRGPs divide asymmetrically at the VZ surface to self-renew and generate a projection neuron to form the PP [67,70]. Between ~GW8-GW15 vRGPs divide asymmetrically at the VZ surface to self-renew and give rise to SNPCs which are capable of generating IPs that can give rise to deep-layer cortical neurons. This stage is named infragranular neurogenesis [68].

A major difference between mice and humans is the existence of an inner SVZ (iSVZ) and an oSVZ. At GW15-GW16, vRGPs begin to give rise oRGPs which radially migrate to the oSVZ. These oRGPs differentiate into IPs which can divide multiple times to give rise to cortical

neurons, ultimately increasing total neuronal production. In mice, continuous radial glial fiber connections exist between ventricular and pial surfaces of the cortex, even at the end of neurogenesis. However, in humans starting at ~GW15-GW16, oRGPs separate from the ventricle/vRGPs creating a tRGP which remains on the VZ surface and an oRGPs which inherits a discontinuous radial fiber from the vRGPs to produce and guide the migrating of upper-layer cortical neuron production, this process is called supragranular neurogenesis [69].

At ~GW23, gliogenesis begins and continues into early postnatal. Here, tRGPs generate IPs which then differentiate into OPCs and astrocytes (Figure 1.4) [68].

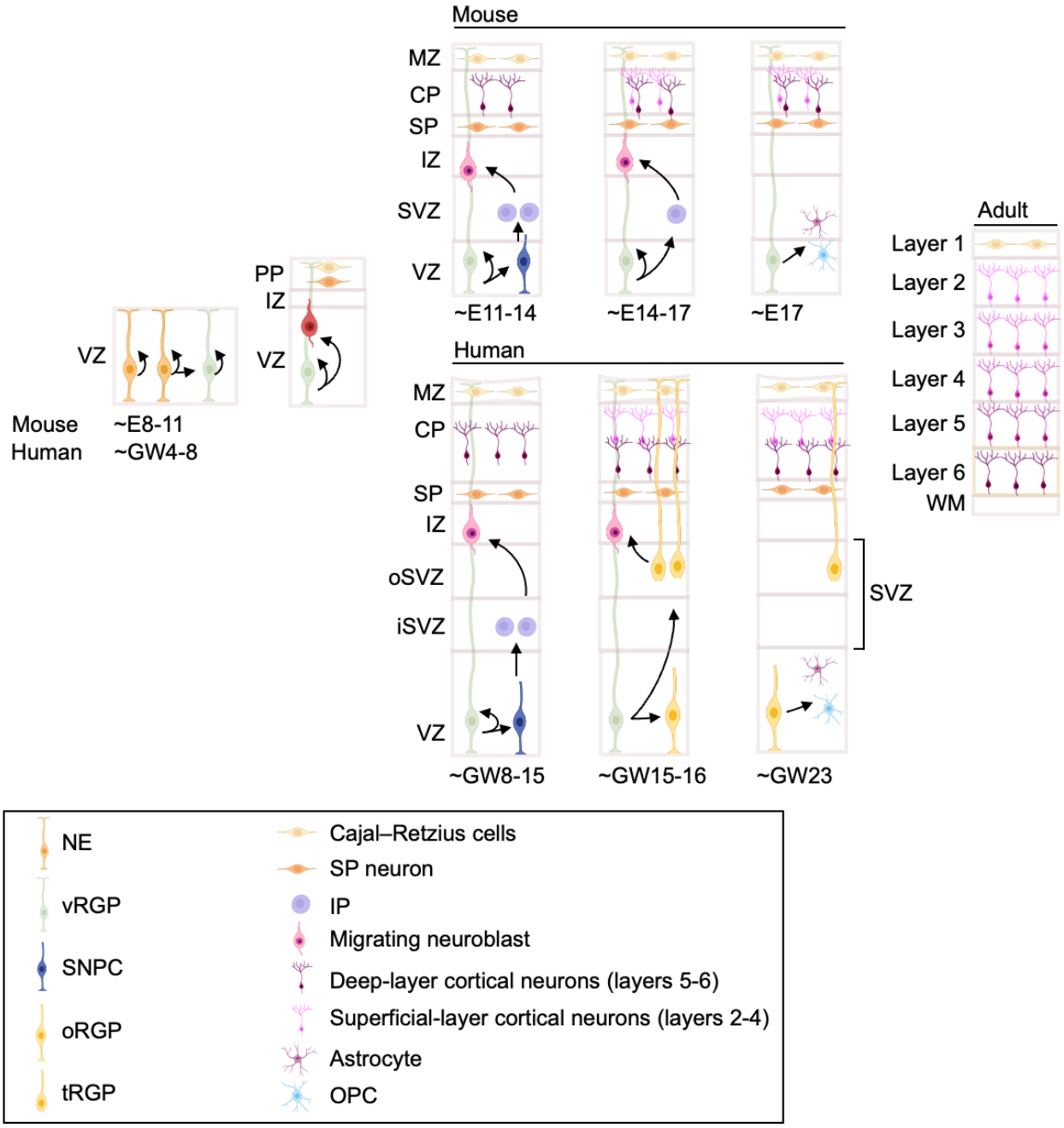
Mouse
MZ
CP
SP
IZ
SVZ
VZ
~E11-14
~E14-17
~E17
Human
MZ
CP
SP
IZ
oSVZ
iSVZ
VZ
~GW8-15
~GW15-16
~GW23
SVZ
Adult
Layer 1
Layer 2
Layer 3
Layer 4
Layer 5
Layer 6
WM
PP
IZ
VZ
VZ
Mouse ~E8-11
Human ~GW4-8
NE
vRGP
SNPC
oRGP
tRGP
Cajal–Retzius cells
SP neuron
IP
Migrating neuroblast
Deep-layer cortical neurons (layers 5-6)
Superficial-layer cortical neurons (layers 2-4)
Astrocyte
OPC

Figure 1.4. Cerebral cortical development in embryo for mice and humans.
NEs initially divide symmetrically to proliferate and expand the NSC pool. NEs start to divide asymmetrically to generate vRGPs. vRGPs produce migrating immature neurons, which migrate through the IZ to form the PP. In mice, SNPCs and vRGPs give rise to IPs which divide symmetrically to produce neurons. RGPs form astrocytes and oligodendrocyte progenitor cells (OPCs). In humans, during infragranular neurogenesis vRGPs divide asymmetrically to generate SNPCs which give rise to deep-layer cortical neurons. During supragranular neurogenesis, vRGPs give rise to oRGPs to produce and guide migrating upper-layer cortical neurons. tRGPs produced from vRGPs generate IPs which then differentiate into OPCs and astrocytes. In both mice and humans, earlier-born neurons form the deep layers of the CP (layers 5 and 6), and later-born neurons migrate outward past the deep layers to establish the superficial or upper layers (layers 2-4). Abbreviations: CP, cortical plate; E, embryonic day; GW, gestational week; IP, intermediate progenitor; iSVZ, inner subventricular zone; IZ, intermediate zone; MZ, marginal zone; NE, neuroepithelial cell; OPC, oligodendrocyte progenitor; oRGP, outer radial glial precursor; oSVZ, outer subventricular zone; PP, preplate; SNPC, short neural precursor cell; SP, subplate; SVZ, subventricular zone; tRGP, truncated radial glial precursor; vRGP, ventricular radial glial precursors; VZ, ventricular zone; WM, white matter.

1.5.3. The cerebral cortex in adulthood

The mammalian cerebral cortex is divided into five lobes the frontal lobe, parietal lobe, temporal lobe, occipital lobe, and limbic lobe. These lobes are then further divided into 48 Brodmann areas based on cytoarchitecture and function [74,75]. In the cerebral cortex, pyramidal cells are the major excitatory neuron type and represent ~70–85% of all neurons in the mammalian cortex [76]. Cortical interneurons are mostly generated from neural progenitors located in the medial GE (mGE) and caudal GE (cGE). Inhibitory interneurons make up ~25% of neurons in the cerebral cortex [77].

The adult cerebral cortex is comprised of six layers. Layer 1 is closest to the pia matter and contains mostly axons and dendrites of pyramidal neurons, Cajal-Retzius cells, and glial cells and is referred to as the molecular layer. Layer 2, the external granular layer, contains densely packed stellate cells and granular cells. Layer 3, the external pyramidal layer, contains loosely packed stellate cells and pyramidal cells. Layers 2-3 primarily communicate via afferent and efferent connections within the cortex. Layer 4, the internal granular layer, contains densely packed stellate cells which receive inputs from the thalamus. Layer 5, the internal pyramidal layer, contains large pyramidal cells. Efferent connections from layer 5 exit the cortex and reach other subcortical areas. Layer 6, the multiform layer, is closest to the white matter and contains multiple types of cells including stellate cells and pyramidal cells [78].

Layers of the cerebral cortex can be identified using layer-specific protein markers such as Satb2, Ctip2, Cux1, and Tbr1. Tbr1 and Satb2 are exclusively expressed in excitatory neurons [79,80], while Ctip2 and Cux1 are primarily expressed in excitatory neurons and, to a lesser degree, in inhibitory interneurons within the cerebral cortex [81,82].

1.6. MeHg neurotoxicity in the adult brain

1.6.1. Behavioural and pathological hallmarks in humans

The brain is the primary target of MeHg toxicity. As introduced previously, exposure to high doses of MeHg during adulthood results in dysarthria, ataxia, muscle weakness, tremors, visual impairment, and hearing loss. Following the Minamata Japan disaster in 1956, the brains of adults who had been exposed to fatal doses of MeHg were assessed. Takeuchi et al., 1962 found lesions in three distinct brain regions. First, lesions and a loss of granular cells were found within the cerebellum, a brain region essential for coordination, posture, and balance. Second, lesions and neuronal loss were found in the calcarine sulcus located within the occipital lobe. This area is concentrated within the primary visual cortex. Finally, lesions were also seen in the central sulcus of the cerebral cortex, an area that divides the sensory cortex from the motor cortex [45]. MeHg targets these brain regions and results in motor, vision, hearing, and cognitive impairments typically observed following high-dose MeHg exposure in adulthood.

1.6.2. Behavioural and pathological hallmarks *in vivo*

At high doses, MeHg causes severe motor impairments in animals similar to the effects seen in humans. The earliest study of MeHg in animals was an epidemiological investigation conducted in Minamata Japan. Local cats who were fed fish from the contaminated bay exhibited movement disorders colloquially referred to as “dancing disease”, ultimately resulting in death [83]. In non-human primates, MeHg 1.5mg/kg BW/day for 2 weeks caused akinesia, motor dysfunction, and Hg accumulation in the cerebellum [84]. Similarly, a study using Swiss mice found that exposure to 40ppm over 7, 14, or 21 days caused a time and dose-dependent decrease in motor ability [85].

At lower doses, MeHg in adult animal models also impairs motor coordination and memory. In dogs, 0.5ppm MeHg resulted in the accumulation of Hg within the occipital lobe and elicited visual and motor deficits after 5 to 8 weeks of exposure [86]. In adult Wister rats, MeHg caused deficits in social memory marked by the social recognition test and reduced memory marked by the Morris Water Maze (MWM) test [87]. These i*n vivo* studies on animal behaviour are critical parameters for understanding the mechanisms of MeHg-induced neurotoxicity.

1.6.3. The underlying mechanism of neurotoxicity

The underlying mechanism of MeHg-induced neurotoxicity involves a complex interplay of cellular, subcellular, and molecular events which will be discussed in tandem below.

1.6.3.1. Mitochondrial dysfunction

Extensive research has been conducted on MeHg-induced oxidative stress and mitochondrial dysfunction. MeHg disrupts the mitochondrial electron transport chain, leading to the increased formation of reactive oxygen species (ROS), such as hydrogen peroxide (H_2O_2) and superoxide anion (O_2^-) (Figure 1.3C).

Isolated mitochondria from adult mouse brains following MeHg treatment had increased H_2O_2 generation and a simultaneous decrease in mitochondria viability [88]. *In vivo*, MeHg was administered to Wistar rats for 5 days, which caused increased H_2O_2 and O_2^- production in the cerebellum and increased O_2^- production in the liver. The formation of H_2O_2 and O_2^- primarily occurred at complexes II and III of the electron transport chain [89]. Similarly, Swiss mice treated with MeHg for 21 days showed increased ROS formation in brain mitochondria [90]. A study in adult Wister rats investigated the effects of long-term low-dose MeHg exposure on the hippocampus, a critical area for memory. They found that MeHg caused neuronal and astrocytic

cell death in multiple areas of the hippocampus. Cell death was accompanied by increased ROS formation and deficits in memory [87].

Further contributing to ROS generation, MeHg is known to interact with the cysteine-containing enzyme manganese-superoxide dismutase (Mn-SOD). Mn-SOD is a part of the ROS scavenging systems within the mitochondria capable of reducing O_2^- to H_2O_2. H_2O_2 is subsequently reduced to H_2O and O_2. MeHg causes a decrease in Mn-SOD activity which further prevents ROS reduction [91,92]. Overall, MeHg results in increased formation of ROS, which results in apoptotic cell death of neurons and astrocytes in critical brain regions.

1.6.3.2. Glutamate and calcium (Ca^2)

Glutamate is a major excitatory neurotransmitter in the CNS. Glutamate plays an essential role in development, learning, and memory. When glutamate is released in high levels within the synaptic cleft it acts as a toxicant eliciting excitotoxicity. It's been shown in multiple models that MeHg results in increased glutamate release.

MeHg administered in rats can significantly increase glutamate release [93] and reduce glutamate reuptake by astrocytes (Figure 1.3A) [94]. In combination, these two factors result in increased extracellular glutamate leading to excitotoxicity and excessive stimulation of N-methyl-d-aspartate (NMDA) receptors (a metabotropic glutamate receptor) [95]. NMDA receptor activation regulates intracellular ions, including calcium (Ca^{2+}). Overstimulation of NMDA receptors leads to increased intracellular Ca^{2+} resulting in cell death and ROS generation (Figure 1.3B). Based on these findings, we can conclude that MeHg can also generate ROS through heightened intracellular Ca^{2+} caused by excitotoxicity [96].

1.6.3.3. Glutathione (GSH) and thioredoxin (Trx)

GSH is an antioxidant and the most abundant thiol in animals. GSH is an essential component in ROS reduction. Two GSH molecules in combination with the enzyme glutathione peroxidase (GPx), form oxidized glutathione (GSSG). This results in the reduction of ROS from H_2O_2 to H_2O [90].

As previously discussed MeHg has an affinity for GSH to form the MeHg-GSH complex, catalyzed by the enzyme glutathione-S-transferases [36]. As a result, this complex reduces the total amount of GSH in circulation. This was confirmed *in vitro* by Kaur et al., 2006, who found that cerebellar neurons and astrocytes had a significant increase in ROS and a significant reduction in GSH after treatment with 5μM MeHg [97]. Similarly, isolated mitochondria from adult mouse brains following 10, 30, and 100μM MeHg treatment showed a significant decrease in GSH content [88]. This evidence highlights that MeHg decreases the amount of circulating GSH capable of reducing ROS. These disruptions are further exasperated by MeHg's ability to reduce GPx activity, an enzyme required for the reduction of ROS from H_2O_2 to H_2O. This was observed in male Swiss mice who showed reduced GPx activity in the brain following treatment with 40mg/L MeHg for 21 days (Figure 1.3C) [90].

As previously introduced, MeHg readily binds to Se forming the MeHg-Se complex. Se is an essential nutrient for humans found in seafood, poultry, and dairy. SeMet is a common source of Se from diet and can be transformed into Sec. Inorganic Se (also called selenite) or Sec can be transformed into selenide, which is used to synthesize selenoproteins like GPx and thioredoxin (Trx). Furthermore, selenide can interact with either Hg^{2+} or MeHg to form insoluble mercury selenide (HgSe). HgSe then reduces Hg bioavailability and toxicity [98]. When Se is depleted due to HgSe complexes, resources are channeled into producing selenoenzymes like thioredoxin

reductase (TrxR). TrxR is responsible for the reduction of thiol groups in many proteins. Under HgSe conditions, oxidized Trx is reduced by TrxR [99]. Oxidized Trx is an inhibitor for apoptosis signal-regulating kinase-1 (ASK1). When Trx is reduced, ASK1 activates downstream c-Jun N-terminal kinase (JNK) and p38 mitogen-activated protein kinases (MAPK), causing apoptosis [100].

Overall, we can conclude that MeHg leads to increased ROS production via two pathways. 1) Through the disruption of complexes II and III of the electron transport chain [89] and 2) through heightened intracellular Ca^{2+} caused by excitotoxicity [96]. MeHg then reduces circulating Mn-SOD [91,92], GSH [88] and GPx [89,90] to prevent ROS reduction. In combination, these factors lead to increased cell damage and death.

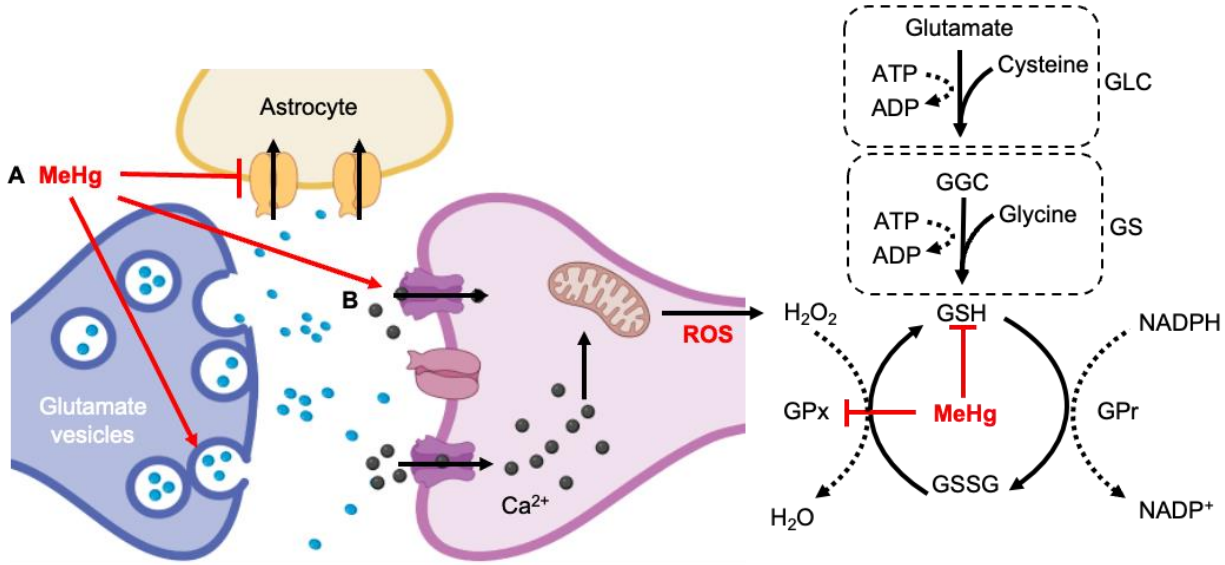

Figure 1.5. The underlying mechanism of MeHg-induced neurotoxicity in the brain. (A) MeHg promotes glutamate release from glutamate vesicles in the presynaptic cleft. MeHg simultaneously inhibits glutamate reuptake by astrocytes, leading to increased extracellular glutamate. (B) Overstimulation of NMDA receptors triggers increased intracellular Ca^{2+}, which generates ROS. MeHg independently triggers increased H_2O_2 production by disrupting the electron transport chain while simultaneously inhibiting GSH and GPx, preventing the reduction of H_2O_2 to H_2O. Abbreviation: ADP, adenosine diphosphate; ATP, adenosine triphosphate; Ca^{2+}, calcium; GGC, γ-glutamylcysteine; GLC, glutamate–cysteine ligase; GPr, glutathione reductase; GPx, glutathione peroxidase; GS, glutathione synthetase; GSH, glutathione; GSSH, oxidized glutathione; H_2O, water; H_2O_2, hydrogen peroxide; MeHg, methylmercury; NADPH, reduced nicotinamide adenine dinucleotide phosphate; NADP+, nicotinamide adenine dinucleotide phosphate; O_2^-, superoxide anion; ROS, reactive oxygen species. Created with BioRender.com.

1.6.4. Cytoprotective effects of MeHg

1.6.4.1. CREB-Akt pathway

There is evidence to suggest that MeHg has dose-dependent cytoprotective effects. cAMP-response element binding protein (CREB) is known to play an important role in neurogenesis, synaptogenesis, and cell survival [101–104]. Interestingly, human neuroblastoma cells treated with MeHg (0.5-1μM) had increased Akt phosphorylation at serine 473 and showed a significant increase in downstream CREB phosphorylation at serine 133 (pS133-CREB), an activated form of CREB, which protected the cells against apoptosis. At higher doses (10μM), this pathway was disrupted, and apoptosis occurred [105]. These findings suggest the CREB plays a critical role in cytoprotection.

Other studies have shown increased CREB phosphorylation in the cerebral cortices of rodents [106] and in a neuroblastoma culture model following MeHg exposure [107]. These studies suggest that the CREB pathway is an underlying mechanism for MeHg-induced cerebral cortical neuronal degeneration. In the neuroblastoma culture model, the cells were exposed to 750nM for 24h to trigger apoptosis [107]. 1-6h post-MeHg exposure, Fujimara et al., observed an increase in CREB phosphorylation; however, by 24h, there was no significant difference compared to the control. In combination, these results suggest that CREB phosphorylation may exert an initial protective effect that is depleted by high doses of MeHg [105,107].

1.6.4.2. Nrf2-Keap1 pathway

The Nrf2-Keap1 pathway is another key cytoprotective mechanism that has been well studied in astrocytes [108] and microglial [109]. Kelch-like ECH-associated protein 1 (Keap1) contains a cysteine residue that MeHg is able to bind to. Under stress conditions, electrophiles and ROS bind to Keap1, which causes nuclear factor erythroid 2-related factor 2 (Nrf2) to

migrate from the cytoplasm into the nucleus leading to transcription of glutamate–cysteine ligase (GCL) and antioxidant heme oxygenase-1 (HO-1) [108–110]. GCL is the rate-limiting step in antioxidant GSH synthesis, making GCL production critical to further antioxidant production [90].

1.7. MeHg neurotoxicity in the fetal brain

As introduced previously, high-dose prenatal exposure to MeHg can cause cerebral palsy, developmental delays, and microcephaly in the afflicted offspring and as such, the effect of MeHg on neurodevelopment has been a key area of study in toxicology. However, the effects of prenatal exposure to MeHg on the development of other organs and systems remain less characterized. Recent literature has found that even nanomolar MeHg can affect the viability of undifferentiated human embryonic stem cells, which provides insight into the pervasive effects of MeHg on embryonic development [111]. Furthermore, animal models have found that prenatal MeHg exposure can affect the cardiovascular [112] and renal system [113].

1.7.1. Behavioural and pathological hallmarks in humans

During high-dose congenial MeHg exposure, the effects are much more generalized compared to adult exposure. Following the Minamata Japan disaster, Takeuchi et al., 1962 found lesions throughout the cerebral cortex and cerebellum of infants exposed prenatally accompanied by degeneration of neurons and astrocytes in the cerebrum and cerebellum [45]. Disrupted lamination of superficial layers of the cerebral cortex was also observed in human case reports following the Iraq grain disaster [114].

1.7.2. Behavioural and pathological hallmarks *in vivo*

Following the Minamata Japan disaster, animal models have been used to elucidate the behavioural and pathological hallmarks of low-dose prenatal MeHg exposure. High-dose MeHg exposure during mouse gestation caused altered wheel running (3ppm) [115] and decreased

working memory (6-8ppm) [116]. The offspring of mice exposed to low doses (0.5ppm) of MeHg during gestation experienced memory impairments and depressive behaviours [117]. At even lower doses (0.01ppm), the offspring of mice exhibited impaired motor abilities and coordination [118].

These behavioural changes are accompanied by pathological changes. Offspring of pregnant mice given a single dose of 20ppm MeHg *in utero* experienced reduced brain weight, enlarged lateral ventricles, and simplified cerebral folial [119]. At lower doses (1ppm), pregnant hamsters had neurodegeneration in the cerebellum [120] consistent with human pathology [45]. Furthermore, disturbed cortical layering has also been observed in rodents [121–124], consistent with human exposure data [114]. These studies suggest that gestational exposure to MeHg causes memory and movement disorders in rodent models by altering the cerebrum and cerebellum.

1.7.3. Underlying mechanism of neurotoxicity and embryonic neurogenesis

The mechanisms that elicit neurotoxicity in adulthood still apply in the fetal brain [125]; however, there are unique processes during fetal development that are critical towards understanding MeHg-induced fetal toxicity. These processes are 1) proliferation and 2) differentiation of NSCs, and 3) migration of neurons within the cerebrum and cerebellum.

1.7.3.1. Proliferation

Proliferation is the process by which NSCs can increase the total number of NSCs present in the fetal brain. This process occurs via symmetric division whereby a NSC divides to give rise to two identical daughter cells. The pool of NSCs sustained by proliferation determines the total number of neural cells generated from the NSCs. Therefore, alterations to proliferation during development can have a severe impact on the total number of neurons and glial cells present in the adult brain [126].

In vitro studies in rat [127–130] and mouse NSCs [126,131] have shown that low-dose MeHg exposure reduces the proliferation of NSCs. A paper previously published in our lab by Yuan et al., (2021) is the first study to show the effect of low-dose MeHg on mouse NSCs. Here, our lab showed that NSCs exposed to low-dose MeHg (250nM) reduced proliferation [126].

1.7.3.2. Differentiation

During brain development, NSCs give rise to multiple neural cell types, such as neurons and glial cells. Once NSCs are committed to a differentiated cell type, they are integrated into the brain. MeHg has been recognized to impact the production of new neurons [126,132–134] and glial cells [125].

MeHg has been shown to inhibit neuronal differentiation in rat hippocampal NSCs [134] and rat cortical NSCs [132,133] after nanomolar MeHg exposure (2.5nM). However, mouse cortical NSCs treated with 250nM MeHg showed increased neuronal differentiation [126]. These contradictory results might be explained by their use of model organism. A study conducted in several mammalian species showed that the binding coefficients for rats in the kidneys, liver, and brain are about 10-fold lower than other mammalian species. This highlights that rats may be a poor model organism for studying the human brain [135]. Interestingly, a culture model using mouse cortical NSCs found that low-dose MeHg (30-300nM) also promoted glial differentiation [125]. Overall, MeHg can alter differentiation in a dose and tissue-dependent manner.

1.7.3.3. Migration

There are two major migratory routes in the cerebral cortex. First, radial migration functions using proliferative RGPs within the ventricular zone. These generate excitatory neurons, which radially migrate toward the surface of the cerebral cortex along RGPs [136]. The second migratory route is tangential migration. Here, inhibitory interneurons migrate from the

GE to the cerebral cortex. This process occurs in multiple waves starting at ~E11.5 in mice where inhibitory interneurons from the mGE migrate dorsolaterally onto the PP. Later stages of cortical interneurons arise from the mGE and cGE and enter via the MZ, SP, and IZ/SVZ migratory streams [64,137].

MeHg has been shown to inhibit neuronal migration in multiple models [114,122,138,139]. First, samples of two newborn full-term human brains whose mother had ingested contaminated bread during the Iraq bread disaster showed abnormal or incomplete neuronal migration, disordered cortical organization, and toxic levels of MeHg in their blood [114]. *In vivo,* researchers investigated changes in the primary motor and the primary somatosensory areas following prenatal MeHg exposure at multiple time points. They found that prenatal treatment with MeHg disrupted inside-out neuronal migration [122]. *In vitro*, decreased migration has been shown in a primary culture of neonatal cerebellar cells (100nM) [138] and human embryonic stem cell (hESCs) derived neural crest cells (50nM) [139].

1.8. Autism spectrum disorder (ASD)

Autism spectrum disorder (ASD) was first characterized by Kanner (1943) [140] as a neurodevelopmental disorder that is defined by impairments in social communication and social interaction combined with repetitive behaviours, restricted interests, and behavioural inflexibility. Following the Diagnostic and Statistical Manual of Mental Disorders, Fifth Edition, ASD is now characterized as a spectrum of mental disorders, including autistic disorder, Asperger's syndrome, childhood disintegrative disorder, and pervasive developmental disorder [141]. Currently, there are no biomarkers for diagnosing ASD and no specific medications to treat ASD symptoms.

ASD prevalence is increasing due to a variety of factors, including enhanced awareness and improved screening. However, the etiology of ASD remains largely unknown since there is extreme variation in its symptomology and severity, development of comorbidities, sex differences, and environmental and genetic contributions. Symptom severity ranges from slight to profound, and the severity of these symptoms are based on the required level of support. Required support ranges from requiring some support to requiring very substantial support [141].

1.8.1. Comorbidities

The second source of heterogeneity in ASD onset is the presence of comorbidities. Common comorbidities observed in individuals with ASD include ADHD, anxiety, depressive disorders, epilepsy, intellectual disabilities, sleep disorders, sight impairment, hearing impairment, and gastrointestinal syndromes [142]. The occurrence of any of these comorbidities varies between individuals and contributes to ASD heterogeneity.

1.8.2. Sexual dimorphisms

The third source of heterogeneity is biological sex. ASD is more prevalent in males than females, with a male:female sex ratio ranging from 2:1 to 4:1 [143–146]. There are multiple theories which attempt to explain the male bias of ASD. First, there may be a gender bias in the diagnostic criteria causing females to be under-identified. Various autistic traits that have been well characterized in boys present differently in girls. 1) Social isolation has been commonly described in males with ASD. However, females with ASD are more likely to be described as obsessive [147,148]. 2) Females with ASD also present with different restrictive interests, including celebrities, makeup, or clothing. These interests may be considered “normal” by the diagnosing clinician leading to an underdiagnosis of female ASD patients [147,149]. 3) Restrictive and repetitive behaviours [150] and language impairments [148,151] are more profound in boys rather than girls. All

of these factors may impair accurate female diagnosis leading to a skewed male bias. The second potential theory that has been proposed to explain the male bias is the Extreme Male Brain theory, with posits that people with ASD view their surrounding through an inherently 'male' lens and, as a result, will take an interest in stereotypically male topics while simultaneously struggling to understand stereotypically female topics/tasks [152]. The final potential theory is the Female Protective Model, which proposes that females display resilience to genetic and environmental insults and, as a result, have a higher required insult threshold to display ASD symptoms. Therefore, they require a greater number of genetic mutations [153,154]. Overall, biological sex differences in ASD etiology are still poorly understood and require more research.

1.8.3. Genetics

The final sources of ASD heterogeneity are genetics and environment. The earliest studies attempting to study the relationship between ASD and genetics studied the occurrence of ASD in monozygotic (MZ) and dizygotic (DZ) twins. Many studies have found that MZ twins were more likely to share a diagnosis than DZ twins, highlighting a clear genetic influence [155–158]. Huguet and Bourgeron (2016) studied the known body of literature on MZ and DZ twins in relation to ASD and found that the concordance for ASD is roughly 45% for MZ twins and 16% for DZ twins [159]. This suggests that there is a large portion of ASD, ~50%, that is non-genetic. Following twin studies, large-scale genetic studies were conducted on ASD patients to identify potential risk genes.

ASD can be broadly classified into non-syndromic and syndromic. In syndromic ASD, a known monogenic syndrome exhibits a phenotypic overlap with ASD. These disorders include Fragile X Syndrome (*Fmr1*), Tuberous Sclerosis (*Tsc1*, *Tsc2*), Angelman and Prader-Willi Syndromes (*UbesA, Gabrb3*), Rett Syndrome (*Mecp2*), and Phelan-McDermid syndrome

(*Shank3*) [160]. Overall, syndromic ASD makes up a small percentage of ASD patients. Non-syndromic ASD, also called "idiopathic autism", has an often unknown etiology.

The first genetic component of ASD onset is inherited common single nucleotide polymorphisms (SNPs). SNPs are the most common genetic mutation in the population. These are a variation that occurs when a single nucleotide (adenine, thymine, cytosine, or guanine) is substituted. These common SNPs are known to be the largest contributing factor in ASD onset. More than 1000 SNPs have been identified, but each is associated with a very low risk of ASD onset; this makes it difficult to identify the causative SNPs [161,162]. The second genetic component of ASD onset is inherited rare single nucleotide variants (SNVs). SNVs are similar to SNPs and are also variations that occur when a single nucleotide is substituted. The key difference between SNVs and SNPs is that SNVs are rarer. For SNPs to be considered common, they must occur within at least 1% of the population. The third genetic component for ASD onset is inherited copy number variations (CNVs). CNVs are genetic variants, including duplications, deletions, inversions, and translocations of segments of DNA present in the genome of an individual [159,160].

From genetic studies, researchers were able to develop genetically modified mice to further understand the underlying mechanism of ASD. Common genetically modified mice target genes include *Nlgn, Shank3, Ube3a, Fmr1*, *Pten*, *Tsc1/Tsc2*, *Mecp2*, and *Nrxn*. These genetically modified mice exhibit key behavioural characteristics of ASD, including impaired ultrasonic vocalizations (USVs), repetitive behaviours, anxiety-like behaviours, deficits in social behaviours, olfactory sensation, and motor coordination [163].

1.8.4. Environment

As highlighted above, ASD has a key genetic component; however, there are roughly ~50% of ASD cases that are not related to any genetic mutations. This suggests that other

factors, such as environmental insults, could play a role in disorder onset [159]. The potential environmental causes of ASD are vast and include maternal diseases or infections during pregnancy, maternal or paternal medication use, and pesticide or heavy metal body burden.

Mouse models of environmental-induced ASD also exist. The two most common are 1) the maternal immune activation (MIA) model and 2) the valproic acid (VPA) model. First, the MIA model is a process where inflammation in the blood and amniotic fluid of mothers can trigger perturbed fetal CNS development [164]. Second, VPA is a medication that is primarily used to treat epilepsy and bipolar disorder. VPA exposure during embryo can cause ASD, which has been validated in clinical trials [165,166]. Both of these environmental mouse models of ASD show key behavioural phenotypes of ASD, such as impaired sociability and repetitive behaviours [164,165].

Environment x gene interactions also contribute to ASD etiology. These are 1) *de novo* CNVs and 2) de novo SNVs. These are mutations that are present for the first time in one family member as a result of a variation in a germ cell. In combination, these *de novo* variants contribute to 9.5% of ASD occurrences [159].

1.8.5. Neuroanatomical abnormalities

1.8.5.1. Humans

Various brain regions and systems underlying cognitive functions are compromised with ASD. First, restrictive repetitive behaviours have been linked to the cortico-striatal-thalamo-cortical pathway [167]. This pathway involves connections between the cerebral cortex, striatum, and the thalamus. This circuit is important for movement and habit formation and has already been implicated in the formation of restrictive-compulsive behaviours in obsessive-compulsive disorder (OCD) [168]. Increased striatal connectivity was found in the limbic cortices and brainstem

of children with ASD [169]. Furthermore, changes in striatal volume have been correlated to restrictive repetitive behaviours in multiple studies of ASD children and adolescents [170–172].

Second, deficits in sociability have been linked to multiple areas of the "social brain", including the fusiform gyrus (FG), medial prefrontal cortex (mPFC), the inferior and the middle frontal gyrus, the amygdala, the orbital frontal cortex (OFC), and the superior temporal sulcus (STS). These areas work in tandem to recognize, and process faces, emotions, and voices, and subsequently monitor and adjust self-behaviors [173]. ASD children exposed to fearful faces showed lower activation of the amygdala and right STS, while exposure to a happy face caused less activation in the right inferior frontal gyrus [174]. Furthermore, adolescents and adults with ASD show reduced activation of the FG compared to neurotypical controls [175,176].

Finally, deficits in language have been linked to the inferior and middle frontal gyrus, Broca's area, and Wernicke's area [177–179]. MRI studies have shown key differences in the activation of these areas for both children and adults with ASD. Children with ASD have significantly greater activity in the inferior frontal gyrus than controls [179]. Conversely, adolescents with ASD had reduced activation of the inferior and middle frontal gyrus [178]. Adults with ASD show more activation in Wernicke's area and less activation in Broca's area [177]. Inconsistencies among studies may be a result of the heterogeneous nature of ASD.

Macrocephaly is often associated with ASD and causes the circumference of an infant's head to be larger than normal [140]. Macrocephaly can be caused by megalencephaly (an enlargement of the brain); however, it is important to note there are other causes that do not affect brain size [180]. Accelerated early brain development is well documented in children with ASD. Studies have shown that total brain volume is increased in younger individuals with ASD [181,182], but older individuals with ASD show decreased brain volume or no difference compared

to matched controls [183]. A recent longitudinal study assessed volumetric brain changes in individuals with ASD. Researchers found that from age 10-15, brain volume of individuals with ASD decreases relative to controls [184]. Researchers sought to determine if there are specific neuroanatomical abnormalities in children with ASD, which potentially facilitates increased total brain volume. Overall, researchers have commonly observed an increase in ventricles [184–186], gray matter [187,188], white matter [188–190], cortical thickness [191–193], neuron population [194,195], and density of cortical minicolumns [189,194].

1.8.5.2. Rodents

Various brain regions have been proposed as key mediators of ASD-like behaviours in rodents. First, restrictive repetitive behaviours have been correlated to many brain regions across many mouse models of ASD, including the striatum, cortex, thalamus, hippocampus, cerebellum, hypothalamus, and amygdala [196,197]. Second, in rodent models, sociability has been associated with the olfactory bulb, the mPFC, the nucleus accumbens, the paraventricular nucleus of the hypothalamus, the amygdala, the bed nucleus of the stria terminalis, and the ventral tegmental area [198]. Finally, brain areas associated with deficits in communication in rodents are the least studied and understood. However, recent findings have shown that the cerebral cortex is not required for USV production. This suggests that rodent communication may arise from subcortical regions [199].

Similar to human ASD patients, an increase in total brain volume [200], gray and white matter volume [201], cortical thickness [202,203], and neuronal overproduction were observed in various rodent models of ASD [204,205]. However, it is important to note that some mouse models of ASD show reduced total brain volume [206], reduced gray and white matter volume [207], and reduced cortical thickness [208].

There are a few intrinsic problems with using ASD rodent models. First, ASD is difficult to diagnose in humans and even more difficult to diagnose in rodents. This is because ASD is not defined by biomarkers but instead by core symptoms [145]. Furthermore, the symptoms of ASD highly overlap with the symptoms of attention-deficit/hyperactivity disorders (ADHD), further complicating diagnosis [145]. Second, deficits in social interaction can only be approximated in rodents. This is because we cannot interpret a rodent's feelings or intentions. Finally, deficits in social communication can also only be approximated in rodents. Rodents can vocalize via USVs, but they do not possess verbal language.

1.8.6. Underlying mechanism

Researchers next aimed to determine the underlying mechanisms of ASD onset. Unlike other neurodevelopmental and neurodegenerative disorders, ASD does not have a unifying cellular or molecular mechanism. Here, I will discuss 1) impaired neurogenesis, proliferation, and migration, 2) overgeneration or under-pruning of synaptic connections, 3) and excitatory/inhibitory (E/I) imbalance. These hypothesized mechanisms do not function in isolation and will be discussed in parallel below.

Impaired neurogenesis, proliferation, and migration have been considered in relation to ASD/macrocephaly. A few factors support this hypothesis. First, as previously discussed, neuron overproduction has been observed in human ASD patients [194,195] and rodent models of ASD [204,205]. Second, many ASD-related genes are involved in the canonical Wnt pathway, which is essential for the regulation of cell proliferation, differentiation, and apoptosis (*Chd8, Tbr1*) [209]. Finally, similar to prenatal MeHg, ASD can cause disrupted neuronal migration/cortical lamination in superficial layers of the cerebral cortex in ASD human postmortem brains [210,211]. Similar to humans, ASD can also disrupt superficial layer neuronal migration in rodent ASD

models. In mice, overproduction of superficial pyramidal neurons in the cortex has been shown to trigger ASD-like behaviours [204]. Some researchers have also observed changes in deep-layer neuron production in a 16p11.2del-ASD mouse model. Here, researchers observed an overproduction in deep-layer neurons marked by Tbr1, and a decrease in the number of superficial-layer neurons marked by Satb2 [212]. In contrast, other researchers have observed no change in the number of Tbr1, Ctip2, or Satb2 in the BTBR-ASD mouse model [213]. Overall, this research suggests that neurogenesis, proliferation, and migration may play a critical role in ASD etiology.

Synaptic formation and function is a key underlying mechanism associated with ASD. Excitatory neurotransmitter glutamate is involved in synaptogenesis. Neurexins (Nrxn) and neuroligins (Nlgn) are a family of proteins encoded by genes implicated in ASD etiology. At a glutamatergic synaptic cleft, pre-synaptic Nrxn binds to post-synaptic Nlgn [214]. This forms a Nrxn-Nlgn complex which recruits neurotransmitter receptors and scaffolding proteins to promote synaptogenesis. Overexpression of either Nrxn or Nlgn can lead to enhanced synaptogenesis and E/I imbalance.

E/I balance regulated by glutamatergic and GABAergic neurotransmission is implicated in ASD pathogenesis. A few factors support this hypothesis. First, increased glutamatergic signalling [215–217] and reduced GABAergic signalling has been observed in ASD patients [215,217]. Second, various ASD-related genes encode for proteins related to glutamate receptors and signalling (*Grin*) [218,219], glutamate pre-synaptic proteins (*Nrxn*) [214], and glutamate post-synaptic proteins (*Nlgn, Shank3*) [220–224]. Finally, treating glutamate excitotoxicity with ionotropic glutamate receptor antagonists relieves ASD symptoms in rodent models [225]. It has shown

promising results in human clinical trials [226,227] Overall, this highlights the critical role glutamate plays in ASD etiology.

1.8.7. Prenatal Hg and ASD

As mentioned above, heavy metal exposure is a potential environmental cause of ASD. In the past, Hg has been suspected of causing ASD, primarily through vaccines containing thimerosal. Thimerosal is an ethylmercury-containing compound that was widely used as a preservative in various drugs, including vaccines. However, vaccines containing thimerosal have been deemed safe [228], and the link to ASD development has been disproven [229]. Here we will examine the current literature on the relationship between prenatal MeHg/Hg exposure and ASD onset in humans and rodent models and the potential underlying cellular and molecular mechanisms which may mediate this.

1.8.7.1. Epidemiology

Longitudinal prospective studies attempting to study the long-term effects of moderate fish intake in the Faroe Islands and the Seychelles found contradictory results. Integrative analyses attempted to resolve the findings of these studies and found that each μg/g increase in maternal hair Hg was associated with a decrease in child IQ between 0.18-0.7 [230,231]. Interestingly, ASD is also strongly associated with intellectual disability [232].

Other epidemiological research investigating the relationship between ASD and MeHg exposure is inconsistent. Various studies have shown a relationship between Hg exposure and ASD in children measured by Hg in blood [233], urine [234], hair [235–239], and baby teeth [240]. However, it is important to note that other studies have observed no relationship between Hg exposure and ASD measured by Hg in blood [241–243], urine [243,244], hair [234,243,245–251], baby teeth [252], and brain [253]. Further contributing to the uncertainty between Hg and ASD, some studies have found a

negative relationship between Hg in hair and ASD [254,255]. Interestingly, Majewska et al., 2010 compared hair Hg between two age groups of ASD children to neurotypical children. Majewska found that younger ASD patients had lower hair Hg than old ASD patients [256]. Holmes et al., hypothesized that this was a result of impaired Hg excretion into the blood during pregnancy which may slow Hg concentration in postnatal hair samples [254].

However, a few key flaws exist in apprising epidemiological research investigating MeHg exposure and ASD. These are 1) biomarkers used to assess Hg exposure and 2) the medium of exposure. First, as highlighted above, Hg is assessed via biomarkers of internal exposure. Common biomarkers used are blood, hair, urine, and baby teeth. Biomarkers like urine, hair, and blood are commonly used to evaluate the body burden of Hg. However, due to human variability, they may not accurately reflect Hg exposure and toxicity. Differences in renal function and hydration may affect Hg concentration in urine. In hair samples, it's difficult to evaluate endogenous versus exogenous Hg exposure. Blood anti-coagulants and whole versus separated blood analysis will affect Hg exposure estimation accuracy [257]. Second, the medium of exposure to MeHg/Hg is an important factor in ASD onset. The most common way humans are exposed to MeHg is via fish consumption. Fish contain beneficial long-chain polyunsaturated omega-3 fatty acids and Se, both of which can have advantageous characteristics. Polyunsaturated omega-3 fatty acids are known to aid prenatal development [258] and provide protective effects against Hg toxicity [11]. Furthermore, Se is also known as a protective agent against Hg toxicity [13–16]. Based on this, the effect of prenatal MeHg exposure via maternal fish consumption may have a diminished effect. Overall, using rodent models to study the isolated effect of MeHg may be critical to further our understanding.

1.8.7.2. Rodents

No prenatal rodent models have been employed to study the relationship between MeHg and ASD. However, the relationship between MeHg and ASD has been investigated in rodents following adult exposure. Two studies have found that adulthood exposure to MeHg exacerbates abnormalities seen in the BTBR T+ Itpr3tf/J (BTBR)-ASD mouse model [259,260]. Al-Mazroua et al., 2022 found that MeHg enhanced marble burying, self-grooming, and impaired sociability in the BTBR mouse line [259], while Attia et al., 2022 found that MeHg worsened DNA repair and the oxidant/antioxidant imbalance [260]. Overall, there is a potential relationship between ASD and MeHg exposure in rodents. However, there remains a gap in the literature regarding the causal effect of prenatal MeHg exposure on ASD in rodents.

1.8.7.3. Underlying mechanism

Here, I will aim to draw parallels between known cellular, subcellular, and molecular effects of Hg exposure and ASD pathology. MeHg has an affinity for GSH and forms a MeHg-GSH complex [36]. This reaction is critical for MeHg demethylation and subsequent detoxification. Numerous studies have found that individuals with ASD have lower levels of both GSH and cysteine [261–263]. Similarly, James et al., 2009 has shown that cells derived from ASD children had lowered GSH and elevated levels of GSSG compared to controls [264]. This could impair MeHg elimination and enhance MeHg-induced toxicity. However, because GSH levels were not assessed *in utero,* a key question remains. Is MeHg exposure reducing GSH levels in ASD patients? Or are GSH levels already reduced in ASD patients, which enhances their susceptibility to MeHg toxicity?

Polymorphisms in glutathione-S-transferase genes associated with increased/normal glutathione-S-transferase function have been shown to reduce Hg body burden. In a study

conducted by Barcelos et al., 2012 individuals with the *GSTT1* wildtype genotype had lower hair Hg. In contrast glutathione-S-transferases genes associated with reduced glutathione-S-transferase function have also been shown to heighten Hg body burden. Barcelos et al., 2012 also showed that *GSTT1* and *GSTM1* homozygous deletion carriers had higher levels of hair and blood Hg compared to controls. Suggesting that glutathione-S-transferases genes are critical to Hg detoxification [265]. Pregnant mothers carrying a non-functional *GSTT1* had higher blood Hg levels and gave birth to children with significantly lower birth weights [266]. A study in Jamaican children with ASD found that GSTP1 Ile105Val (missense substitution causing an isoleucine to valine substitution) had a higher incidence of ASD than controls [267]. Furthermore, Hodgson et al., 2014 found that male ASD patients had a significantly larger reduction in GSH than female ASD patients, further contributing to the possible mechanism mediating ASD sexual differences [268].

Similar results have been observed in GCL (the rate-limiting step in GSH synthesis) genes, where the GCLM-588 TT (cytosine to thymine nucleotide substation at position 588 lowering functionality) genotype had significantly higher Hg in erythrocytes [269]. Together, these results suggest that the reduction in GSH occurs prior to MeHg exposure caused by an increased genetic susceptibility; however, more research is required to confirm this phenomenon.

As highlighted previously, MeHg leads to increased ROS through glutamate ecotoxicity [96]. Increased glutamatergic signalling [215–217] and reduced GABAergic signalling has also been observed in ASD patients [215,217]. Again, a key question remains; is MeHg exposure increasing glutamate levels in ASD patients? Or are glutamate levels already increased in ASD patients, which enhances their susceptibility to MeHg toxicity?

1.9. Metformin

Type 2 diabetes (T2D) is a chronic condition whereby the body becomes resistant to the effects of insulin, resulting in high levels of glucose in the bloodstream (hyperglycemia). Over time, hyperglycemia can lead to damage to various organs and tissues in the body. Metformin is an FDA-approved drug for the treatment of patients with T2D. Due to its safety and affordable price, metformin is now the most commonly prescribed oral anti-diabetic agent worldwide, taken by over 150 million people annually [270]. Metformin works to treat T2D by several pathways. First, metformin can decrease glucose production by inhibiting gluconeogenesis in the liver. Second, metformin increases glucose uptake by the muscles, which results in decreased blood glucose. Finally, metformin enhances insulin sensitivity in the liver, muscle, and adipose tissue, which results in lower blood glucose levels [271].

Metformin is an oral medication that is absorbed in the small intestine by a combination of passive diffusion and active transport by plasma membrane monoamine transporter (PMAT) and organic cation transporter 1 (OCT1) transporters in enterocytes [272]. Once absorbed, metformin is transported to the hepatocytes of the liver and renal endothelial cells of the kidneys. Metformin is primarily eliminated unchanged in the urine. However, a small amount of metformin is metabolized in the liver to form an inactive metabolite, guanidine [273,274]. The elimination half-life is approximately 3-6h [275].

1.9.1. Metformin in the brain

Metformin is also known to cross the BBB as metformin has been measured in the brains of rodents [275,276] and has been extensively studied as a potential treatment for human neurological conditions [277–279]. Furthermore, under both physiological and pathological conditions, metformin can promote adult neurogenesis *in vivo* [280–282]. The mechanism by which metformin crosses the

BBB is still controversial. Early studies showed that OCTs are present in the BBB of rodents [283] and, as a key transporter of metformin, may be required for BBB transport. However, more recent work has put forward that OCT1-3 are not present in the BBB and, therefore, are not required to facilitate the transport of metformin [284]. Due to this, the exact mechanism by which metformin crosses the BBB is still unknown. Furthermore, metformin can cross the placental barrier of humans [285,286] and rodents via OCT3 [287].

Our earlier work showed that metformin was able to promote the differentiation of cortical precursors through the AMPK-aPKC-CBP pathway. Metformin acts on this pathway to phosphorylate AMPK, which subsequently phosphorylates atypical protein kinase C ζ/ι (aPKCζ/ι) to phosphorylate CBP at serine 436 (pS436-CBP) [280]. pS436-CBP sustains the interaction between CREB and CBP. Thus, aPKC-mediated pS436-CBP acts as a compensatory mechanism when CREB-pS133 is lacking [288,289]. Alternatively, pS133-CREB recruits CBP binding to transcribe downstream CREB target genes [290].

Furthermore, both pS133-CREB and pS436-CBP cannot co-exist [288,291], possibly due to the negative charge on the phosphorylation groups. The S133 phosphorylation site on CREB lies within the kinase-inducible domain (KID) and binds to the kinase-inducible domain interacting domain (KIX) located on CBP [292]. Within 150bp exists the S436 phosphorylation site just adjacent to the CH1/TAZ1 binding domain of CBP. The proximity of these two phosphorylation sites and their charge is a potential mechanism mediating CREB/CBP repulsion (Figure 1.6).

As previously introduced, human neuroblastoma cells treated with MeHg at nanomolar concentrations showed a significant increase in pS133-CREB [105]. This suggests that metformin may represent a potential therapeutic strategy for prenatal low-dose MeHg exposure due to the potential for CREB/CBP repulsion.

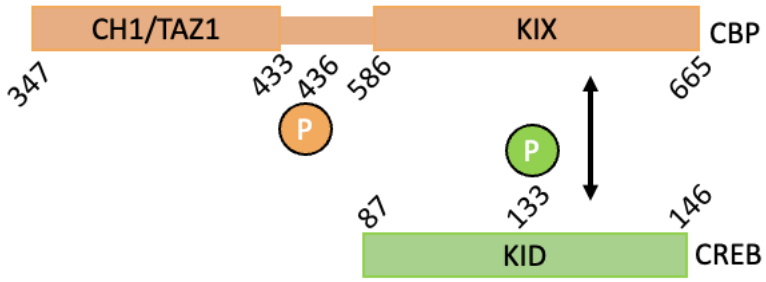

Figure 1.6. Proposed mechanism of pS133-CREB and pS436-CBP interaction.

1.10. Rationale, hypothesis, and aims

1.10.1. Rationale

Our lab found that sub-micromolar (250nM) MeHg induced premature neuronal differentiation of cultured embryonic cortical precursors without causing cell death [126]. Post-doctoral fellow Dr. Joseph Leung confirmed this phenomenon *in vivo* and found that prenatal exposure to 0.2ppm MeHg promotes premature differentiation of cortical precursors in the VZ to generate newborn neurons at the expense of their proliferation.

Here, I will investigate the underlying cellular and molecular mechanism that mediates this and determine if prenatal MeHg exposure results in behavioural abnormalities consistent with ASD.

1.10.2. Hypothesis and aims

I *hypothesize* that fetal low-dose MeHg treatment induces premature neuronal differentiation of embryonic cortical precursors via the CREB/CBP pathway and results in ASD-like behavioural abnormalities in young adulthood. To test this hypothesis, I will perform the following three aims:

Aim 1: Investigate the underlying cellular mechanism that causes low-dose MeHg-induced premature differentiation through single-cell RNA-sequencing (scRNA-seq) of prenatal cerebral cortices.

Aim 2: Probe CREB activity/CREB-CBP interaction as an essential molecular mechanism to drive MeHg-induced premature neuronal differentiation.

Aim 3: Determine the long-term behavioural consequences of prenatal MeHg exposure.

I present my experiments and results in the following 5 chapters. Chapter 2 presents the materials and the general methods used to complete all experiments. Chapters 3, 4, and 5 present the results of experiments targeted in each of the three aims presented above. Chapter 6 is the concluding chapter summarizing key findings and discussing their significance. A majority of the results of this thesis have been published in the peer-reviewed journal *iScience* entitled "Prenatal low-dose methylmercury exposure causes premature neuronal differentiation and autism-like behaviors in a rodent model". Authored by Allison Loan, Joseph Wai-Hin Leung, David P. Cook, Chelsea Ko, Barbara Vanderhyden, Jing Wang, and Hing Man Chan published in 2023. https://doi.org/10.1016/j.isci.2023.106093.

Chapter 2: Materials and methods

2.1. Animals

All animal use was approved by the Animal Care Committee of the University of Ottawa in accordance with the Canadian Council of Animal Care policies. CD-1 mice were purchased from Charles River and C57BL/6J mice were bred in house. CD-1 mice were specifically used to study embryonic cortical development because they produce large litters. However, CD-1 mice go blind with age, therefore, C57BL/6J mice were used for all subsequent behavioural testing. All mice were maintained on a 12h light/12h dark cycle with ad libitum access to food and water. Experimental animals were kept in both group and single-housed cages dependent on litter size. Both male and female mice were used for all tests. Sex differences of C57BL/6J mice used during behavioural testing were assessed and notable sex differences were reported.

2.2. Single-cell RNA-sequencing (ScRNA-seq)

2.2.1. Experimental treatments

For scRNA-seq pregnant CD-1 mice were treated with 0ppm, or 0.2ppm MeHg via drinking water starting from E0 to E13.5. 0.2ppm MeHg drinking water was prepared by diluting a stock solution of 1000ppm MeHg(II)Cl (cat#33553, Alfa Aesar) in distilled water.

2.2.2. Multiplexing samples

Six embryos from 2 pregnant mice for each treatment (0ppm or 0.2ppm MeHg) were dissected, and cerebral cortices were collected after the removal of the meninges from the brains of embryos. The cortical tissues were incubated in papain solution at 37ºC for 20 min. Afterward, papain solution was removed, and the tissues were dissociated by a bovine serum albumin (BSA) coated Pasteur pipette in the neurobasal medium (cat#21103049, Thermo Fisher Scientific) containing 500uM GlutaMAX Supplement (cat#35050061, Thermo Fisher Scientific), 2% B27 supplement (cat#17504044, Thermo Fisher Scientific), 1% penicillin-streptomycin

(cat#15140122, Thermo Fisher Scientific), and 40 ng/ml FGF2 (cat#10018B, PeproTech). The tissue debris was then allowed to settle for 1 min. The supernatant was collected and centrifuged at 300g for 2 min. After centrifugation, the supernatant was removed, and the cell pellet was resuspended in the medium by gently pipetting 20 times. The cell suspension was finally passed through a 40μM sterile cell strainer (Fisherbrand).

Multiplexing was performed according to the protocol [293]. Dissociated cortical cells from 0ppm (control) and 0.2ppm MeHg treatment were labelled with different DNA barcodes using lipid-modified oligonucleotides (LMOs) to stabilize the barcodes within the plasma membrane. Briefly, cells from each group (0ppm / 0.2ppm MeHg) were duplicated and divided into two samples (250,000 cells/sample). The cells were then resuspended and pelleted in a 1.5mL Eppendorf tube at 500 × g for 5 min. Then the four samples were labelled with four different barcodes. For the barcode labelling, the resulting pellet was resuspended in 80μl of 250nM anchor mix and 2uL of a 10uM unique barcode (kindly provided by Prof. Zev Gartner from the University of California, San Francisco). Samples were then incubated on ice for 10 min. Afterward, 10μl of 2μM the co-anchor LMOs was added to each sample and incubated for 5 min. Then 200μL of phosphate buffered saline (PBS) with 1% BSA was added to each sample, and the samples were pelleted at 500 × g for 5 min. Each sample was resuspended and pelleted in 200uL PBS with 1% BSA at 500 × g for another 5 min. Subsequently, the four samples were pooled together into a new Eppendorf tube and were pelleted at 500 × g for 5 min. After centrifugation, the cell pellet was resuspended by PBS containing 1%. The final concentration of cell suspension was 500-1000 cells/μl. Viability and cell counts were assessed using a Countess II Cell Counter and Viability Analyzer (Life Technologies). Only samples with a viability ≥ 80% were further processed.

2.2.3. Library preparation and sequencing

The scRNA-seq library preparation and sequencing were performed at StemCore laboratories from the Ottawa Hospital Research Institute. The multiplexed suspension was processed for 3' scRNA-seq (v3) with the 10x Genomics Chromium System, targeting to capture 20,000 cells. As described in McGinnis et al. [293], barcode cDNA libraries were isolated from the gene expression library during initial size exclusion and processed independently. Gene expression libraries were prepared according to the manufacturer's protocol. Libraries were sequenced using the high-output 75 cycle kit on the NextSeq500 (Illumina), achieving an average coverage of 20,558 reads per cell. The resulting 20,535 cells had an average of 2248 unique genes detected and 5120 UMI counts per cell.

2.2.4. Processing of raw sequencing reads

Raw sequencing reads were processed using cellranger v4.0.0 and the mm10 build of the mouse genome. Except for explicitly setting–expect-cells=20000, default parameters were used for all samples. MULTI-seq barcode libraries were simply trimmed to 28bp using Timmomatic v0.36 prior to demultiplexing [294].

2.2.5. Demultiplexing expression data

Barcode reads were matched to the reference sequences, and the incorporated cell barcode was used to assign the barcode count to an individual cell. The distribution of counts for each barcode across all cells was assessed, and a threshold was defined to deem a cell positive for the barcode by identifying the minima between the bimodal (signal in negative/positive populations) distribution. Cells positive for more than one barcode are classified as multiplets. Only cells positive for a single barcode are retained for downstream analysis.

2.2.6. Analysis

Quality control was first performed on all four samples concurrently, including multiplets and negatives. The expression matrix was loaded into R as a Seurat (v4.0.1) object (Table 2.1). First, cells with less than 200 genes detected were removed. Second, contaminated cells (red blood cells) were removed by correlating library size and gene detection in each cell and removing outliers. Finally, cells with more than 10% mitochondrial reads were removed. The top 2000 variable genes were detected in Seurat using the "vst" selection method. Expression values were scaled, and the following technical factors were regressed out: percentage of mitochondrial reads and number of RNA molecules detected. Principal component analysis (PCA) was performed on the highly variable genes, and Uniform Manifold Approximation and Projection (UMAP) embeddings were calculated from the first 30 principal components with 0.2 resolution.

Any additional cell populations that highly expressed red blood cell markers *Hbb-y* and *Hba-x* were subset out. Clusters were identified by the expression of known cell-type markers. The markers *Fabp7* and *Cenpf*, *Fabp7* and *Hes5*, *Eomes*, *Dcx*, *Sox5*, *Reln*, *Gad1*, *Igfbp7*, and *Rgs5* were used to identify the basic cell types, radial glial precursor 1 (RGP1), radial glial precursor 2 (RGP2), intermediate progenitors, immature neurons, mature neurons, layer 1 cortical neurons, interneurons, endothelial cells, and pericytes, respectively. I also assessed additional genes discriminating these clusters by performing a simple Wilcoxon rank-sum test with the FindAllMarkers() function in Seurat. I next isolated the transitional cell subset and reprocessed the subset using the same normalization and integration approach. After data visualization for both the total cell population and the transition cell population, multiplets and negatives were subset out, and 0ppm and 0.2ppm were separated for further downstream analysis.

2.2.7. Transitional state analysis

For UMAP visualizations cells were considered positive for markers of a cell type if the mean expression of a group of cell type marker genes was > 0.5 log normalized expression. Canonical markers were used to differentiate cell types. Radial glial-positive (RG^+) markers used were *Sox2, Fabp7, Pax6, Hes1,* and *Hes5*. Intermediate progenitors-positive (IP^+) markers used were *Eomes*, *Sstr2, Gadd45g,* and *Mfap4*. Neuronal-positive cells (N+) markers used were *Tubb3, Neurod1, Sox11, Neurod6, Dcx, Bcl11b,* and *Sox5*.

2.2.8. RNA velocity

PCA and UMAP embeddings that were produced during the initial analysis step were embedded using Seurat. Velocity estimates were calculated using the scVelo (v0.2.2.) python package with default parameters (Table 2.1). Velocity vectors and velocity graphs were computed and then projected on UMAP embeddings. Velocity vector analysis was conducted using Image J (Table 2.1).

2.2.9. Pseudotime analysis (Monocle 2)

A pseudotime trajectory of all cells was constructed using the DDRTree method implemented in Monocle 2 [295]. This is a computational method that performs lineage trajectory reconstruction based on single-cell transcriptomics data. The root state argument was called and defined as the branch containing canonical genes known to be the earliest in neurodevelopment [296,297].

Table 2.1. Softwares used.

Softwares	Source	Identifier
Image J	NIH	https://imagej.nih.gov/ij/download.html
Zeiss Axiovision	Carl Zeiss Microscopy	https://carl-zeiss-vision-axiovision-viewer.software.informer.com/4.8/
UltraVox XT	Noldus	https://www.noldus.com/ultravox-xt
Ethovision XT	Noldus	https://www.noldus.com/ethovision-xt
R studio	Posit	https://posit.co/
Pycharm	Jetbrains	https://www.jetbrains.com/pycharm/
Graphpad	Prism	https://www.graphpad.com/scientific-software/prism/
AriaMx	Agilent	https://www.agilent.com/en/product/real-time-pcr-%28qpcr%29/real-time-pcr-%28qpcr%29-instruments/ariamx-software-download

2.3. Primary cell culture

Primary cortical precursors were obtained from E11-12 pooled cortices dissected from CD-1 mice (Charles River Laboratories) as previously described [126]. Briefly, embryos were transferred to ice-cold Hanks' balanced salt solution (HBSS) (cat#14175103, Fisher Scientific), and the cerebral cortices were isolated from the brain after the meninges were removed. The cortical tissue was mechanically triturated with a plastic pipette and seeded on coverslips in a 24-well plate or directly into a 6-well plate (Thermo Fisher Scientific), both pre-coated with 15% poly-L-ornithine (PLO) (cat#72302, Sigma-Aldrich) and 5% laminin (cat#CB40232, Thermo Fisher Scientific). For immunocytochemical experiments, cells were plated in a 24-well plate at a density of 200,000 cells/ml. For western blotting experiments, 1,000,000 cells were seeded in each well of a 6-well plate. The cortical precursors were cultured in a neurobasal medium (cat#21103049, Thermo Fisher Scientific) containing 500uM GlutaMAX supplement (cat#35050061, Thermo Fisher Scientific), 2% B27 supplement (cat#17504044, Thermo Fisher Scientific), 1% penicillin-streptomycin (cat#15140122, Thermo Fisher Scientific), and 40 ng/ml fibroblast growth factor 2 (FGF2) (cat#10018B, PeproTech). The sex of cells is not reported as cell isolation occurred in embryo.

2.3.1. Experimental treatments

Primary cultured cells were exposed to 0nM, 250nM MeHg [126], 500uM metformin [280], or 250nM MeHg + 500uM metformin for 4 or 72 h. 250nM MeHg was achieved by a 1:250 dilution of 62.5µM MeHg that was freshly prepared from a stock solution of 4mM MeHg(II)Cl (cat#33553, Alfa Aesar) through serial dilution with the culture medium. 500µM metformin was made by 1:400 dilution of a stock solution of 0.2M metformin (cat#PHR1084, Sigma-Aldrich) in the culture medium.

2.3.2. Western blotting and densitometry

Mouse cortical precursors were cultured as previously described. After culturing for 4 h in the neurobasal medium, the cortical precursors were lysed in cold lysis buffer containing 1mM sodium orthovanadate (Sigma-Aldrich S6508-10G), 20 mM sodium fluoride (cat#AC201295000, Fisher Scientific), 1mM phenylmethylsulfonyl fluoride (PMSF) (cat#P7626-5G, Sigma-Aldrich), 10 μg/mL aprotinin (Fisher Scientific, cat#PI78432) and 20 μg/mL leupeptin (cat#PI78436, Fisher Scientific). Protein concentration was determined using the bicinchoninic acid assay (cat#23225, Fisher Scientific) and BSA as a standard. Equal amounts of protein (10-20μg) were boiled in sample buffer, separated by 12% sodium dodecyl sulfate–polyacrylamide gel electrophoresis (SDS-PAGE) gels, and transferred to 0.2μm polyvinylidene difluoride (PVDF) membrane 1 h at 100V. Membranes were blocked in 3% BSA in tris-buffered saline + 0.1% Tween-20 (TBS-T) for 1 h at room temperature and then incubated overnight at 4°C with primary antibodies. After washing with TBS-T, membranes were incubated with secondary antibodies in a blocking solution for 1 h at room temperature. Detection was performed using the Electrochemiluminescence reagent (cat#PI32209, Fisher Scientific) and autoradiography films (cat#E3018, Denville Scientific). Membranes were subsequently stripped washed with TBS-T and re-probed as described above. Densitometry was performed using Image J (Table 2.1).

For western blots, the primary antibodies were rabbit anti-paPKCζ/ι (T410/403) (cat#9378, Cell Signaling, 1:500), mouse anti-aPKCζ/ι (cat#610175, BD Pharmingen, 1:500), rabbit anti-p-CREB (S133) (cat#9198S, Cell Signaling, 1:500), mouse anti-CREB (cat#9104S, Cell Signaling, 1:500). Secondary antibodies for western blots were HRP-conjugated goat anti-mouse, anti-rabbit (cat#7074, cat#7076, Cell Signalling, 1:3000) (Table 2.3).

2.3.3. Reverse transcription quantitative real-time polymerase chain reaction (RT-qPCR)

Mouse cortical precursors were cultured as previously described. RNA was extracted from the cortical precursor cells using the PureLink RNA Mini Kit (cat#12183020, Thermo Fisher). Complementary DNA (cDNA) was synthesized using QuantiTect Reverse Transcription Kit (cat#205311, Qiagen). The RT-qPCR was performed with a SensiFAST SYBR Lo-ROX Kit (cat# BIO-94005, Bioline) on an Mx3000P qPCR System (Agilent, Santa Clara, CA, USA). All qPCRs were performed using the same protocol (95°C, 30 s; 95°C, 5 s for 1 cycle; 60°C, 15 s; 72°C, 10 s for 40 cycles). All qPCR samples were performed in technical duplicates and then averaged. Glyceraldehyde-3-phosphate dehydrogenase (GAPDH) was used as an endogenous normalization control and the fold expression relative to GAPDH was determined by the standard curve method. PCR primer sequences were selected from published sequences [298–300] (Table 2.2). Primers were validated by running gel electrophoresis and experimental conditions were optimized. Data were analyzed using AriaMX (Agilent, Santa Clara, CA, USA) (Table 2.1).

Table 2.2. Primer sequences for RT-qPCR.

Primer	Forward	Reverse
cfos	ATCCTTGGAGCCAGTCAAGA	ATGATGCCGGAAACAAGAAG
FosB	GATCGCCGAGCTGCAAAAAG	CCTTAGCGGATGTTGACCCTGG
Jund	GGAGCTGGAGAGGCTGATCAT	GGGTAGAGGAACTGCGTACTGG
GAPDH	AGGTCGGTGTGAACGGATTTG	TGTAGACCATGTAGTTGAGGTCA

2.3.4. Proximity ligation assay (PLA)

Mouse cortical precursors were cultured as previously described. Cells were fixed in 4% paraformaldehyde for 10 min after 4h in culture and were incubated in 1x PBS with 0.3% Triton X-100 (PBST) for 1h at room temperature for permeabilization. Cells were blocked in Duolink blocking solution for 1 h at 37°C. Primary antibodies were diluted in Duolink antibody diluent and incubated in a humid chamber at 4 °C overnight. Slides were then washed with Duolink 1x wash buffer A two times for 5 min. PLUS and MINUS PLA probes were diluted 1:5 in the Duolink antibody diluent and added to the coverslips which were incubated for 1 h at 37°C. The coverslips were then washed with Duolink 1x wash buffer A two times for 5 min. The coverslips were incubated in 5x Duolink Ligation buffer diluted 1:5 in water with ligase added at a 1:40 dilution for 30 min at 37°C. Coverslips were then washed with Duolink 1x wash buffer A two times for 5 min. Coverslips were incubated in 5x Duolink amplification buffer diluted 1:5 in water with polymerase added at a 1:80 dilution for 100 min at 37°C. Coverslips were then washed with Duolink 1x wash buffer B two times for 10 min and Duolink 0.01x wash buffer B for 1 min at room temperature. Coverslips were mounted with Duolink In Situ Mounting Medium containing 4′,6-diamidino-2-phenylindole (DAPI) staining and stored at -20°C (cat#DUO92101-1KT, Sigma-Aldrich). Digital image acquisition was performed using a Zeiss Axioplan 2 fluorescent microscope with Zeiss Axiovision software containing z-axis capability (Carl Zeiss Microscopy, Thornwood, NY, USA) (Table 2.1). Ten to fifteen image sections at a maximum of 1µm apart were captured in the Z-axis for each section and then processed as an optical stack for quantification. 25 cells per sample over at least four independent experiments were analyzed. PLA^+ dots (each dot represents one interaction) were quantified. Quantification was conducted in Image J.

For the PLA, the primary antibodies were rabbit anti-p-CREB (S133) (cat#9198S, Cell Signaling 1:500) and mouse anti-CBP (cat#sc-7300, Santa Cruz Biotechnology, 1:200) (Table 2.3).

2.3.5. Immunocytochemistry

Mouse cortical precursors were cultured as previously described. Cells were fixed in 4% paraformaldehyde for 10 min after 72h in culture, they were then blocked with 10% normal goat serum (NGS) (cat#16050122, Thermo Fisher Scientific), diluted in 1x PBS with 0.3% Triton X-100. The cells were incubated within primary antibodies diluted in 10% NGS in PBS with 0.3% Triton X-100 and then incubated in a humid chamber at 4 °C overnight. Following this, secondary antibodies were diluted in PBST and incubated for 1 h at room temperature. After rinsing with PBS, the coverslips were mounted in a Lab Vision PermaFluor Aqueous Mounting Medium (cat#TA-030-FM, Thermo Fisher Scientific). The culture was washed three times for 5 min/time with 1x PBS between each step.

2.3.5.1. Antibodies

The primary antibodies used for immunocytochemistry were mouse anti-βIII-tubulin (cat#801201, BioLegend, 1:1000), rabbit anti-Pax6 (cat#901301, BioLegend, 1:1000), rabbit anti-Sox2 (cat#AB5603MI, Millipore, 1:500), and mouse anti-Ki67 (1:500, Abcam, cat#ab15580). The secondary antibodies used were donkey anti-rabbit Alexa Fluor 555 (cat#A31572, Thermo Fisher Scientific, 1:500) and goat anti-mouse Alexa Fluor 488 (cat#A32723, Thermo Fisher Scientific, 1:500). Nuclear counterstaining was performed with Hoechst 33342 (cat#4082, Cell Signalling Technology, 1:1000) (Table 2.3).

2.3.5.2. Image acquisition and quantification

For cultured cells, digital image acquisition was performed using a Zeiss Axioplan M.2 fluorescent microscope with Zeiss Axiovision software (Carl Zeiss Microscopy, Thornwood, NY, USA). Six random images per experiment were taken for all conditions, and at least 700 cells per condition were counted for each experiment. At least four independent experiments from four pregnant mice were conducted for all conditions. Quantification was performed using Image J.

2.3.6. Hg analysis

Mouse cortical precursors were cultured as previously described. After 72h in culture the medium and first PBS wash was collected and immediately stored at -20°C for future Hg analysis. For medium analysis 100µl was added to each boat, and 200µl was added for each wash. A minimum of two replicates were analyzed for each medium sample and then averaged. The theoretical amount of Hg was calculated and compared to the measured amount.

For the measurement of Hg levels, a direct thermal decomposition Hg analyzer (MA-3000, Nippon Instrument, Bryan, TX, USA) was used. Calibration was conducted using additive B which was added alone to three ceramic boats and then added to each boat containing treated samples. The MA-3000 used for Hg analysis has a detection limit of 0.01 to 0.02ng.

2.4. *In vivo* work

2.4.1. Experimental treatments

To study whether metformin could reverse the effects of MeHg on embryonic cortical development, we dosed pregnant CD-1 mice with 0ppm MeHg (control), 0.2ppm MeHg, 4 mg/ml metformin [288], or 0.2ppm MeHg+4 mg/ml metformin via drinking water from E0 to E15. Control received drinking water only. At the end of the treatment, brains were collected from the

E15 embryos for immunohistochemistry. For all immunohistochemical analysis, the 3-4 embryos in each condition came from two biological different pregnant mice. 0.2ppm MeHg drinking water was prepared by diluting a stock solution of 1000ppm MeHg(II)Cl (cat#33553, Alfa Aesar) in distilled water. For the preparation of the metformin solution, metformin powder (cat#D150959, Sigma-Aldrich) was dissolved in distilled water to make a final concentration of 4 mg/ml.

To study the long-term consequences of prenatal MeHg exposure I dosed pregnant C57BL/6 mice with 0ppm, or 0.2ppm MeHg via drinking water starting from the first day of their pregnancy until birth. At P7 and P9, I performed USV testing. Starting at P60, I performed all subsequent behavioural testing on the offspring.

2.4.1. Tissue preparation

The collected brain samples were fixed in 4% paraformaldehyde (PFA) in 0.1M PBS at room temperature for 24 h. They were then immersed in 30% sucrose solution in 0.1M PBS and stored at 4°C until use. Brain samples were embedded in optimal cutting temperature compound (OCT) (cat#95057-838, VWR) and frozen for cryosectioning. Serial 16µm (embryonic) and 20µm (adult) brain sections were obtained using a cryostat and sequentially mounted on glass slides. Glass slides were allowed to air dry before storage at -80°C for later use.

2.4.2. Immunohistochemistry

For the detection of Mcm2, Sox2, DCX, Tbr1, Cux1, Ctip, and Satb2 brain sections stored in the -80 °C freezer were first washed with 1x PBS 3 times (5 min each). Section slides were then incubated in 0.01 M citric acid (pH 6.0) at 90 C for 10 min for antigen retrieval. Afterwards, brain sections were blocked/permeabilized for at least 1 h at room temperature in 10% NGS (cat#16050122, Thermo Fisher Scientific) or 3% BSA (cat#9998S, Cell Signalling

Technology) in PBST. Subsequently, the brain sections were incubated with each primary antibody overnight, followed by secondary antibody treatment at room temperature for 1 h. The brain sections were washed with 1x PBS three times (5 min each) before incubation of secondary antibodies.

For the detection of Ki67 and Pax6, brain sections were blocked for 1 h at room temperature using the mouse IgG blocking reagent from the mouse on mouse (M.O.M.) immunodetection kit basic (cat#BMK-2202, Vector Laboratories). Brain sections were then washed with 1x PBS 2 times (2 min each) and further incubated with M.O.M. diluent prepared according to the manufacturer's protocol. After 5-min incubation with the M.O.M. diluent, slides were incubated with primary antibodies in the M.O.M. diluent overnight at room temperature. Subsequently, slides were washed with 1x PBS 2 times (2 min each) and incubated with the M.O.M. biotinylated anti-mouse IgG reagent for 10 min. After 2 washes with 1x PBS (2 min each), brain sections were incubated with secondary antibodies, Streptavidin Alexa Fluor 555 conjugate (cat#S32355, Invitrogen,) and donkey anti-rabbit Alexa Fluor 647 (cat#A31573, Invitrogen). Brain sections were mounted using PermaFluor™ solution (cat#TA-030-FM, Thermo Fisher Scientific).

2.4.2.1. Antibodies

The primary antibodies used for immunohistochemistry in the embryonic cortex were rabbit anti-Pax 6 (cat#901301, Biolegend, 1:2000), mouse anti-Ki67 (cat#550609, BD Pharmingen, 1:200), rabbit anti-Mcm2 (cat#ab4461, Abcam, 1:500) mouse anti-Sox2 (cat#ab79351, Abcam, 1:400), and goat anti-DCX (cat#sc-8066, Santa Cruz Biotechnology, 1:500). The primary antibodies used for immunohistochemistry in the adult cerebral cortex were rabbit anti-Tbr1 (cat#ab31940, Abcam, 1:500), mouse anti-Satb2 (cat#ab51502, Abcam, 1:500),

mouse anti-Cutl1 (Cux1) (cat#00001523-M01, Abnova, 1:500), rat anti-Ctip (cat#ab18465 Abcam, 1:500). The primary antibodies used for immunohistochemistry in the adult SVZ were rabbit anti-Mcm2 (cat#ab4461, Abcam, 1:500), and mouse anti-DCX (cat#sc-271390, Santa Cruz biotechnology, 1:500). The primary antibodies used for immunohistochemistry in the adult SGZ were rabbit anti-Mcm2 (cat#ab4461, Abcam, 1:500), and goat anti-DCX (cat#sc-8066, Santa Cruz biotechnology, 1:500).

The secondary antibodies used were goat anti-rat Alexa Fluor 647 (cat#A21247, Thermo Fisher Scientific, 1:500), donkey anti-rabbit Alexa Fluor 555 (cat#A31572, Thermo Fisher Scientific, 1:1000), goat anti-mouse Alexa Fluor 555 (cat#A21422, Thermo Fisher Scientific, 1:1000), donkey anti-rabbit Alexa Fluor 647 (cat#A31573, Thermo Fisher Scientific, 1:1000), goat anti-mouse Alexa Fluor 647 (cat#A32728, Thermo Fisher Scientific, 1:1000) and donkey anti-goat Alexa Fluor 647 (cat#A21447, Thermo Fisher Scientific, 1:1000). Hoechst 33342 (cat#4082, Cell Signalling Technology, 1:1000) was used for the nuclear staining (Table 2.3).

2.4.2.2. Image acquisition and quantification

For embryonic brain sections, digital images of brain sections were taken by a Zeiss Imager M.1 fluorescent microscopy with Zeiss Axiovision software containing z-axis capability. Ten to fifteen image sections at a maximum of 1µm apart were captured in the Z-axis for each brain section and were processed as an optical stack for quantification. Quantification was performed throughout the cortex, including VZ, subventricular zone/intermediate zone (SVZ/IZ), and CP. At least three anatomically matched brain sections were quantified for each embryo among different treatment groups. Quantification was conducted in Image J (Table 2.1).

For adult brain sections, digital images of brain sections were taken by a Zeiss Imager M.1 or M2. fluorescent microscopy with Zeiss Axiovision software containing z-axis capability.

Ten to fifteen image sections at a maximum of 1µm apart were captured in the Z-axis for each brain section and were processed as an optical stack for quantification. Quantification was performed throughout all six cerebral cortical layers, the SGZ, and SVZ. For the cerebral cortex and SVZ, at least three anatomically matched brain sections were quantified for each mouse among different treatment groups. For quantification, the SVZ was divided into three areas the dorsal, ventral, and lateral SVZ. For the SGZ I sampled 1 in every 40 sections throughout the septotemporal axis of the hippocampal structure (−1.3 mm to −3.70 mm relative to bregma referring to the rostral-caudal coordinates). Since the section sampling fraction was 1/40, the resulting raw count for each region was multiplied by 40 to obtain an estimate of cell numbers per SGZ. Quantification was conducted in Image J (Table 2.1).

Table 2.3. Primary antibodies used for immunocytochemistry, immunohistochemistry, western blotting, and PLA.

Antibodies	Source	Identifier
mouse anti-βIII-tubulin	Biolegend	cat#801201
rabbit anti-Sox2	Millipore	cat#AB5603MI
mouse anti-Ki67	Abcam	cat#ab15580
rabbit anti-Pax6	Biolegend	cat#901301
mouse anti-Ki67	BD Pharmingen	cat#550609
rabbit anti-Mcm2	Abcam	cat#ab4461
mouse anti-Sox2	Abcam	cat#ab79351
goat anti-DCX	Santa Cruz biotechnology	cat#sc-8066
rabbit anti-Tbr1	Abcam	cat#ab31940
mouse anti-Satb2	Abcam	cat#ab51502
rat anti-Ctip	Abcam	cat#ab18465
mouse anit-Cutl1 (Cux1)	Abnova	cat#00001523-M01
goat anti-rat Alexa Fluor 647	Thermo Fisher Scientific	cat#A21247
donkey anti-rabbit Alexa Fluor 555	Thermo Fisher Scientific	cat#A31572
goat anti-mouse Alexa Fluor 488	Thermo Fisher Scientific	cat#A32723
goat anti-mouse Alexa Fluor 555	Thermo Fisher Scientific	cat#A21422
donkey anti-rabbit Alexa Fluor 647	Thermo Fisher Scientific	cat#A31573
goat anti-mouse Alexa Fluor 647	Thermo Fisher Scientific	cat#A32728
donkey anti-goat Alexa Fluor 647	Thermo Fisher Scientific	cat#A21447
Hoechst 33342	Cell Signaling	cat#4082
rabbit anti-p-CREB (S133)	Cell Signaling	cat#9198S
mouse anti-CBP	Santa Cruz Biotechnology	cat#sc-7300
rabbit anti-paPKCζ/ι (T410/403)	Cell Signaling	cat#9378
mouse anti-CREB	Cell Signaling	cat#9104S
mouse anti-aPKCζ/ι	BD Pharmingen	cat#610175
HRP-conjugated goat anti-mouse	Cell Signaling	cat#7074
HRP-conjugated goat anti-rabbit	Cell Signaling	cat#7076

2.4.2. Hg analysis

The right hemispheres of E15 brains (after removal of the cerebellum) were collected and immediately stored at -80°C for future Hg analysis.

Hg in the feces, urine, and blood of mice undergoing behavioural testing were analyzed at P22 and P42. Feces, urine, and blood were collected and immediately stored at -20°C for Hg analysis. Following behavioural testing at 3 months old, the mice were sacrificed, and the kidneys, liver, and brain were collected and immediately frozen with liquid nitrogen and stored at -80°C for Hg analysis. The brains were dissected, and the cerebellum, occipital lobe, cerebral cortex, hypothalamus, hippocampus, pons/medulla, and olfactory bulb were isolated and immediately frozen with liquid nitrogen and stored at -80°C for Hg analysis.

For the measurement of Hg levels, a direct thermal decomposition Hg analyzer (MA-3000, Nippon Instrument, Bryan, TX, USA) was used. Quality assurance/quality control methods included blank samples and standard reference material DOLT5. The MA-3000 used for Hg analysis has a detection limit of 0.01 to 0.02ng.

2.5. Behavioural testing

All tests were done at the University of Ottawa Behavior Core. For all tests (except fear conditioning (FC)) mice were habituated for 30 min prior to testing. The behavioural tests were performed in order from the least stressful assessment to the most to reduce stress-related interference.

2.5.1. Ultrasonic vocalization (USV) test

Prior to the expected date of birth, female mice were checked once a day, the day of birth was recorded as P0. At P7 and P9 pups were isolated from their mother and littermates and placed inside a soundproof container for 4 min. The microphone was set to a 5 cm distance from

pups, illumination set at 100 lux, and gain set at 45. After 4 min the pups were sexed, weighed, and returned to their home cage. USVs were analyzed using UltraVox XT (Table 2.1). Calls were recorded and quantified based on call characterization shown below (adapted from Vogel et al., 2019) [301]. Max peak frequency and call duration were then measured for each recorded call.

Call characterization:

I used the following criteria to characterize and quantify each call:

1. Short: Call shorter than 5 ms.

2. Chevron: Call resembled an 'inverted-U', which was identified by a continuous increase in pitch ≥12.5 kHz followed by a decrease that was ≥ 6.25 kHz

3. Complex: Included one component containing two or more directional changes in frequency, each ≥6.25 kHz

4. Flat: Call ≤3 kHz in change from start to end

5. Upward: single harmonic that increases in frequency > 3 kHz from beginning to end

6. Downward: single harmonic that decreases in frequency > 3 kHz from beginning to end

7. Two-Component: Call has two parts: a main call (flat or downward) with an additional shorter component at a different frequency towards the end

8. Frequency-Step: Three or more instantaneous frequency harmonics appearing as a vertically discontinuous "step" on a spectrogram, but with no interruption in time

9. Composite: Two independent components, emitted simultaneously at different frequencies

2.5.2. Marble burying test

Experimental mice were placed in a disposable cage (31cm x 19.5cm x 11cm) with woodchip bedding (Sani Chips) to a depth of 6.5cm with illumination set at 100 lux for a 5 min habituation period. After 5 min the mice are removed and returned to their home cage. 20 marbles were then evenly spaced on top of the woodchip bedding. After 5 min the mice are returned to the disposable cage where they were left undisturbed for 30 min to interact with the 20 marbles. The number of marbles buried in 30 min was recorded by hand. A marble was scored as buried if two-thirds of its surface area is covered by bedding.

2.5.3. Adult social interaction (ASI) test

Experimental mice were placed in an open-field box with illumination limited to red lights only to initially explore an empty wire-mesh enclosure for a period of 5 min. Interaction with the enclosure was measured using Ethovision software as the duration of time spent in close proximity to the enclosure. Testing mice were removed, and an age, sex, and strain-matched novel mouse was placed inside the wire-mesh enclosure 5 min later. Testing mice were then placed back in the open-field box for 5 min and interaction time with the novel mouse was measured. Ethovision tracking software was used to record the behaviours of mice during testing.

2.5.4. Morris water maze (MWM) test

Experimental mice were trained on the hidden platform version of the water maze using a circular pool (122 cm diameter, 83.5 cm depth, 22 ºC) filled with 74.2 cm of water and made opaque with nontoxic white paint. The escape platform (10 cm diameter) was submerged 0.5 cm below the water surface. All testing was conducted under 120 lux lighting and an extra maze visual cue with “X” printed in black ink (2.9 cm thickness) on a white paper (13.5 x 15 cm) was

located on one wall. Acquisition was measured as latency to reach the platform and four possible start locations were pseudo-randomly assigned to each trial. Each animal was given four 60 s trials to find the platform with a 20 min inter-trial interval across 4 days. A probe trial was then completed on day 11 after the 4-day training, leaving the mice to swim in the pool for 60 s when the platform was removed. Immediately after this, the platform was moved to the opposite location and animals were trained in the same manner for 2 additional days. A probe trial was then completed on day 14 after the 2-day training, leaving the mice to swim in the pool for 60 s when the platform was removed. Ethovision tracking software was used to record the behaviours of mice during testing.

2.5.5. Nestlet shredding test

Experimental mice were added to an empty plastic cage and given 1.5h to interact with one cotton nestlet in an empty cage with illumination set to 100 lux. Each nestlet was weighed before the experiment, and the nestlet that was shredded was weighed after the 1.5h interaction time. The percentage of nestlet shredded was recorded for each animal.

2.5.6. Grooming test

Experimental mice were added to an empty plastic cage. After a 10 min habituation period, the mice were then recorded for the subsequent 10 min. The video was then analyzed for the total time spent grooming and the total number of grooming events.

2.5.7. Fear conditioning (FC) test

Experimental mice on day 1 (training) were exposed to a tone 3 times which was immediately followed by a shock (0.4 mA, 2 seconds). The percentage of time spent freezing prior to the initial tone/shock was measured to determine baseline freezing. On day 2 (contextual) experimental mice were exposed to the same environment without shock and tone.

The percentage of time spent freezing within the first three minutes in the conditioning context was measured. On day 3 (cued), the environment was altered to a triangle shape. White noise, red lighting, and vanilla scent was added. The percentage of time spent freezing after the first tone was measured. Ethovision tracking software was used to record the behaviours of mice during testing.

2.5.8. Novel object recognition (NOR) test

Experimental mice were placed at the center of an open-field box (35cm x35 cm x 27cm) with illumination set at 100 lux for 5 min habituation on day 1. Mice were then removed for 5 min, and 2 identical objects were placed inside the open-field box. Mice were reintroduced to the box to explore the two identical objects. Interaction with the objects was measured using Ethovision software as time in close proximity to either object. On day 2, mice were re-habituated with the empty open-field box for a period of 5 min. A familiar object and a novel object were placed inside the box and mice were then reintroduced to the box to explore the objects. The preference index is calculated by dividing the time spent with the novel object divided by the total time spent with both the novel and familiar object multiplied by 100. Values above 50% indicate increased exploration of the novel object. Data from the day 1 habituation period was used to calculate velocity and distance travelled using Ethovision software (Table 2.1).

2.6. Quantification and statistical analysis

Statistical analyses were performed with a two-tailed student's t-test, one-way, or two-way ANOVA with Tukey's multiple comparisons as post hoc analysis. Error bars indicate the standard error of the mean (SEM). P-values presented as *$p<0.05$, **$p<0.01$, ***$p<0.001$, and ****$p<0.0001$.

A priori, the study sample size for all immunohistochemical analyses was calculated by a statistical power analysis primarily to compare the difference between the two study groups. In the absence of available pilot data, a pragmatic decision was taken with the following assumptions: a difference of 30% between the control and MeHg treatment group, a 10% standard deviation from the mean, and a significance level of 5%, and a minimum statistical power of 80%. The calculated effective sample size of 3 or greater per condition was targeted. For all behavioural testing, I utilized the Mead's resource equation to determine sample size.

Chapter 3: Asymmetric division is a potential essential cellular mechanism underlying MeHg-induced premature neuronal differentiation

Using a culture model that mimics *in vivo* cortical development in the dish [302,303]. Our lab found that MeHg treatments at sub-micromolar (250nM) levels induced premature neuronal differentiation of cultured embryonic cortical precursors, without causing cell death [126]. Post-doctoral fellow Dr. Joseph Leung aimed to determine if low-dose MeHg could cause a similar impact on embryonic cortex development *in vivo*. To test this, he administered 0ppm and 0.2ppm MeHg via drinking water to pregnant mice from E0 until E15. E15 brain samples were collected from the embryos for immunohistochemical analysis (Appendix Figure 1A). Dr. Leung found that 0.2ppm MeHg significantly reduced the number and proportion of proliferating $Ki67^{+}/Pax6^{+}$ cortical precursors, also known as RGPs, in the VZ (Appendix Figure 1B-D) and increased the number of doublecortin-positive (DCX^{+}) neuroblasts in the VZ (Appendix Figure 1E-F). He also found that 0.2ppm MeHg did not increase apoptotic cell death in the E15 cortex (Appendix Figure 1G-H). Consistent with our *in vitro* work [126], prenatal exposure of 0.2ppm MeHg promotes premature differentiation of cortical precursors in the VZ to generate newborn neurons at the expense of their proliferation *in vivo,* without altering cell death.

scRNA-seq is a tool that allows researchers to stratify cell populations, examine changes in gene expression, and determine cell trajectories within a heterogeneous cell population [304]. Based on our consistent *in vitro* and *in vivo* results, I collaborated with Dr. Joseph Leung to perform scRNA-seq with the goal being to determine the underlying mechanism that triggers premature neuronal differentiation.

3.1. Annotating cell populations in E13.5 cortices

To understand the underlying cellular mechanisms that contribute to MeHg-induced neuronal differentiation during embryonic cortical development, we performed multiplexed scRNA-seq [293] using cortex tissue collected from E13.5 embryos that had been exposed to 0ppm

or 0.2ppm MeHg from the date of conception (Figure 3.1). In total, we collected 3 embryonic cortices from each group receiving 0ppm or 0.2ppm MeHg treatment. The dissociated cortical cells were randomized to be barcoded into four groups before being combined for the MULTI-seq (Figure 3.1, Figure 3.2A-F). Following demultiplexing, I transcriptionally profiled a total of 4,947 mouse cortical cells from the control group (0ppm MeHg) and 5460 cells from the MeHg group (0.2ppm) (Figure 3.1).

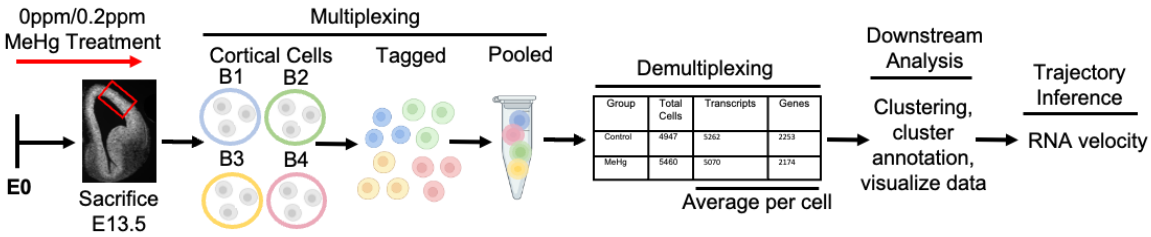

Figure 3.1 ScRNA-seq methods.
Schematic of prenatal exposure of MeHg to pregnant mice. 0ppm (control) and 0.2ppm MeHg were administered through drinking water to pregnant mice starting at E0 until E13.5, at which point the dorsal cortical cells were collected for multiplexing. Two technical replicates from both 0ppm and 0.2ppm MeHg treated groups were tagged and pooled for multiplexing RNA-seq. Following demultiplexing, downstream analysis and trajectory inference were performed. Created with BioRender.com.

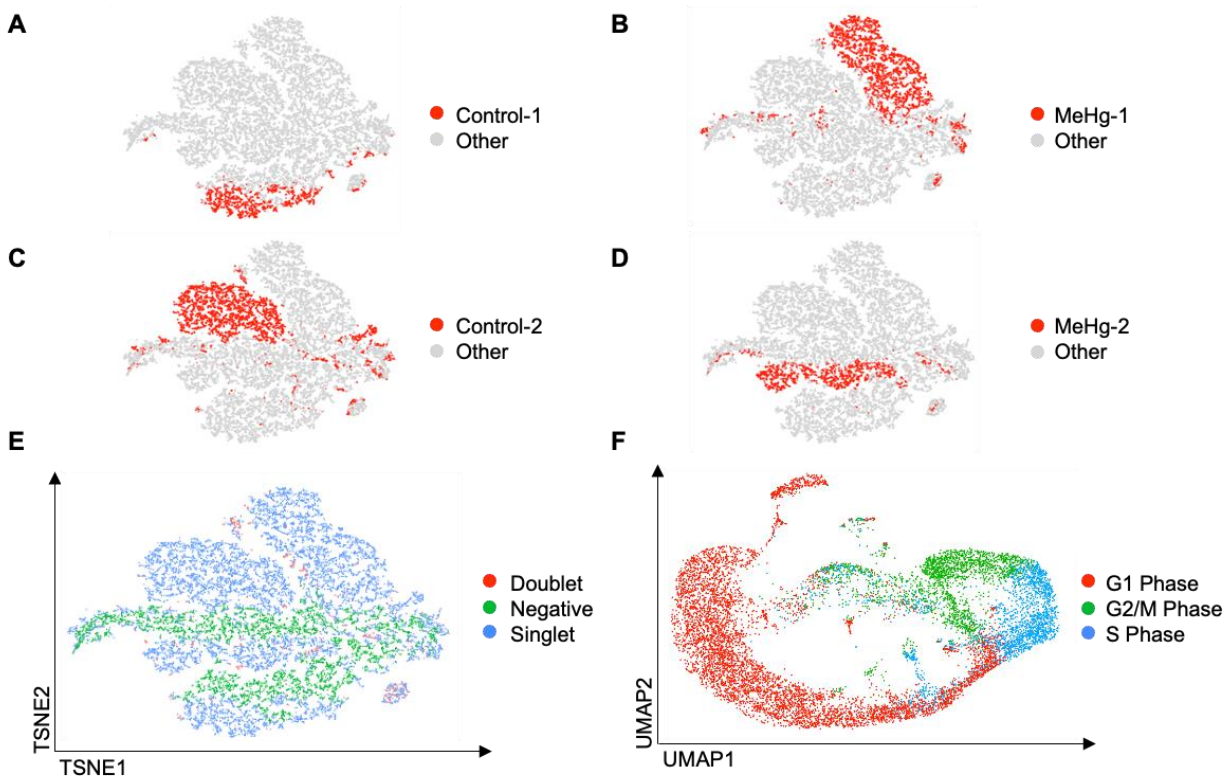

Figure 3.2. Demultiplexing scRNA-seq dataset from E13.5 cortex.
(A-D) T-distributed stochastic neighbor embedding (t-SNE) visualizations, coloured by treatment condition, control-1 (0ppm barcode-1) (A), 0.2ppm MeHg barcode-1 (B), control-2 (0ppm barcode-2) (C), 0.2ppm MeHg barcode-2 (D). (E) t-SNE visualizations, coloured by singlet, doublet, or negative barcode. (F) Visualization of cells after PCA and UMAP visualization, coloured by cell cycle phase.

After initial processing, cells were clustered based on their expression profile, and annotation of cell types was based on established cell markers available from the published scRNA-seq dataset for embryonic cortex at E13.5-E14 [296,297] (Figure 3.3A-C, Table 3.1-3.2). A total of 10 clusters were identified: RGP1, RGP2, intermediate progenitors, immature neurons, mature neurons, interneurons, endothelial cells, layer 1 cortical neurons, pericytes, and a cluster of transitional cells (Figure 3.3A-D).

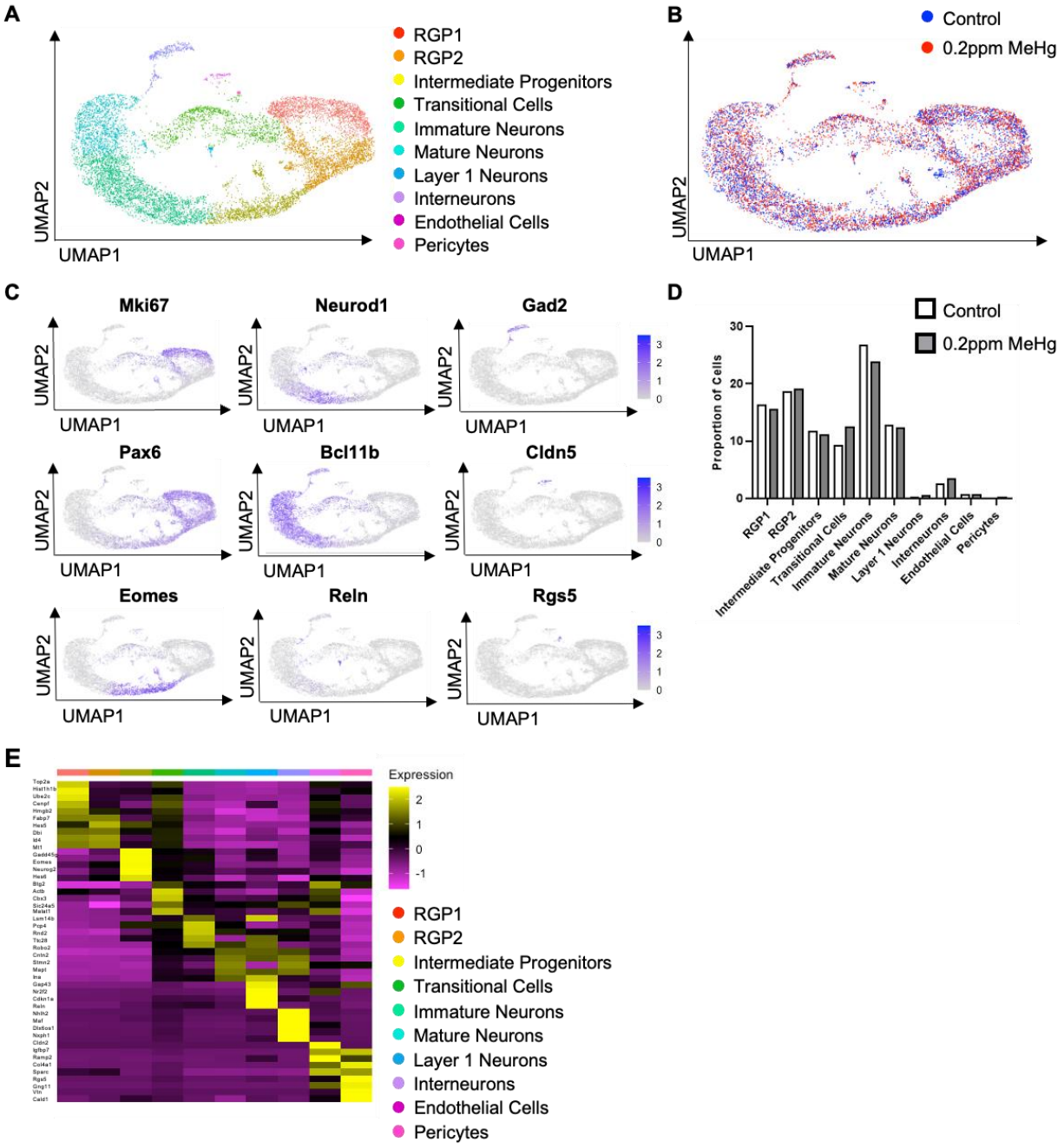

Figure 3.3. Annotating cell populations in E13.5 cortices.
(A) Visualization of cells from 0ppm and 0.2ppm MeHg groups after PCA and UMAP, coloured by Seurat clustering and annotated by cell type. (B) UMAP visualization of 0.2ppm MeHg (red) and 0ppm (blue) treatment groups. (C) Visualization of the total cell population after PCA and UMAP, coloured by expression of key marker genes (*Mki67*, *Pax6*, *Neurod1*, *Bcl11b*, *Reln*, *Gad2*, *Clnd5*, *Rgs5*). (D) The proportion of cells in each cluster for 0ppm and 0.2ppm MeHg. (E) Heatmaps of top five differentially upregulated genes relative to all other clusters at E13.5 cortex over ten cell clusters.

Table 3.1. Annotations, abundance, and marker genes of each cell cluster used for UMAP visualizations of the total cell population.

Cluster #	Cell type	% Abundance control	% Abundance MeHg	Marker genes
1	RGP1	16.33	15.64	Top2a, Ube2c, Cenpf, Fabp7, Mki67
2	RGP2	18.71	19.15	Sox2, Pax6, Hes1, Hes5, Pcna, Mcm3/6, Fabp7
3	Intermediate Progenitors	11.84	11.19	Eomes, Sstr2, Gadd45g, Mfap4
5	Immature Neurons	26.78	23.86	Neurod1, Sox11, Neurod6, Dcx
6	Mature Neurons	12.93	12.34	Bcl11b, Sox5, Stmn2
7	Layer 1 Neurons	0.38	0.58	Reln, Trp73, Lhx1, and Lhx5
8	Interneurons	2.62	3.55	Gad1, Gad2, Sst, Dlx1, Dlx2
9	Endothelial Cells	0.8	0.69	Igfbp7, Cldn5, Col4a1, Col4a2 Pecam1, Vwa1
10	Pericytes	0.1	0.32	Igfbp7, Rgs5, PdgfrB

Table 3.2. Annotations, abundance, and marker genes of each cell cluster used for UMAP visualizations of the transitional cell population.

Cluster #	Cell type	% Abundance control	% Abundance MeHg	Marker genes
1	RGP1	52.99	53.18	Dbi, Fabp7, Vim, Cenpf, Ube2c
2	Immature/Mature Neurons	44.01	43.76	Tubb3, Sox11, Neurod6, Stmn2
3	Layer 1 Neurons	1.70	0.86	Reln
4	Pericytes/Endothelial Cells	1.28	2.17	Igfbp7, Rgs5, Col4a1, Col4a2

A population of cells that was particularly interesting was the transitional cells. This population does not highly express any known marker genes used to annotate specific cell types but universally expresses feature genes shown in RGP1, RGP2, and immature neurons at minimal levels (Figure 3.3E) and was named to reflect this. Interestingly, I observed that MeHg treatment increased the proportion of transitional cells (Figure 3.3D). Sub-clustering showed that the transitional cells were comprised of 4 subpopulations of cells: RGP1, immature/mature neurons, layer 1 cortical neurons, and pericytes (Figure 3.4A-C). The composition of these cells suggests that the transitional cell population represents the asymmetrical division of RGP1 cells to directly generate cortical neurons. MeHg treatment increased the total population of transitional cells but did not alter the cell distribution within the 4 subpopulations of cell clusters (Figure 3.4D).

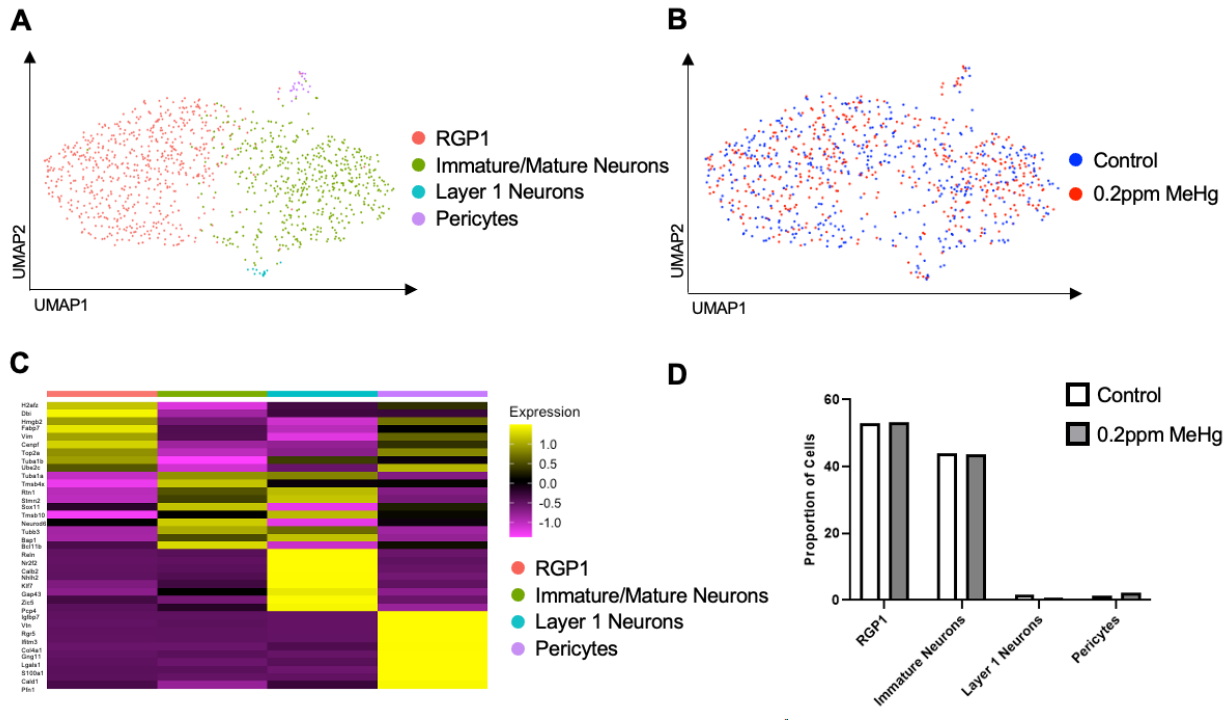

Figure 3.4. Annotating cell populations within the transitional cell cluster.
(A) Visualization of subclusters of the transitional cell population after PCA and UMAP, coloured by Seurat clustering and annotated by cell type. (B) UMAP visualization of 0.2ppm MeHg (red) and 0ppm (blue) treatment groups in transitional cell population subclusters. (C) Heatmap of top ten differentially upregulated genes over four clusters within the transitional cell population. (D) Proportion of cells in each subcluster within the transitional cell population for both 0ppm and 0.2ppm MeHg.

Ordering of cells by pseudotime in an unbiased manner using Monocle 2 [295], confirmed the predicted developmental trajectory in the total cell population (Figures 3.5A-B) and transitional cell cluster (Figures 3.5C-D). In the total cell population, there is a clear developmental trajectory whereby RGPs transition into intermediate progenitors/transitional cells and then mature into immature and mature neurons (Figures 3.5A-B). Similarly, in the transitional cell population, RGP1s mature into immature/mature neurons (Figures 3.5C-D).

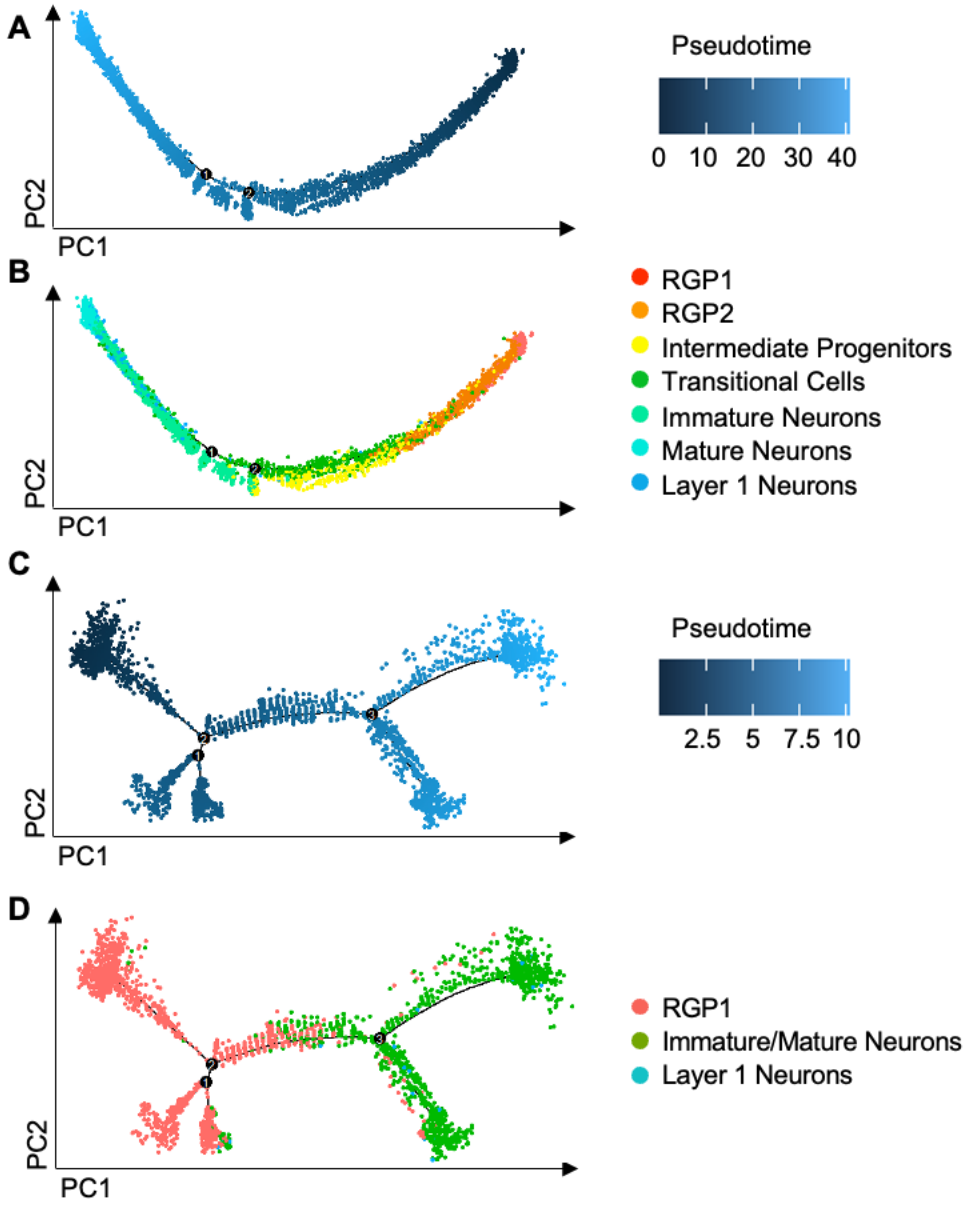

Figure 3.5. Pseudotime analysis (Monocle).
(A) The total cell population (excluding interneurons, endothelial cells, and pericytes) of E13.5 cortices ordered along pseudotime trajectory and colored by pseudotime. (B) Total cell population ordered along pseudotime trajectory and colored by Seurat cluster. **(**C) Transitional cell population (excluding pericytes) ordered along pseudotime trajectory and coloured by pseudotime. (D) Transitional cell population ordered along pesudotime trajectory and coloured by Seurat cluster. Each point represents a cell. Pseudo-time represents an ordering of cells based on the inferred trajectory, predicting the lineage trajectory.

3.2. Prenatal exposure to MeHg accelerates neuronal differentiation via direct asymmetric division

To further examine whether asymmetric division plays a dominant role to directly produce neurons within the transitional cell population, I classified three cell types, IP, RG, and N, using canonical markers (Table 3.1-3.2). I showed that within the transitional population, roughly 30% of cells co-express marker genes for both RG^+ and N^+ (RG^+/N^+). This is the largest population of co-expressing cells, which suggests that the majority of differentiation that takes place in the transitional population is asymmetric division from RGPs to cortical neurons (Figure 3.6A-D). I then removed the transitional cell population from the total cell population and found that only 1.5% of cells are RG^+/N^+, which suggests that asymmetric division is specific to the transitional population (Figure 3.6E-H).

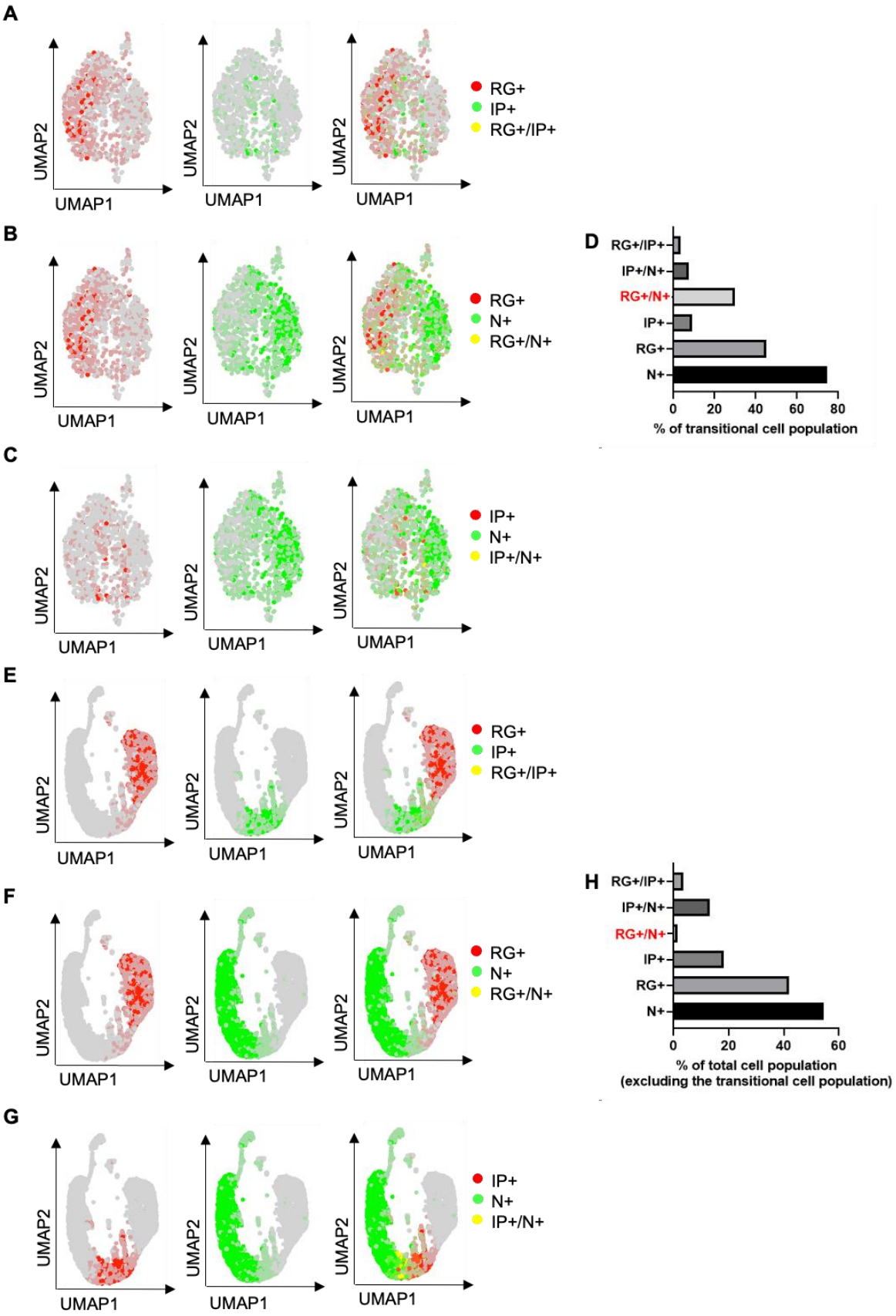
A
UMAP2
UMAP1
RG+
IP+
RG+/IP+
B
RG+
N+
RG+/N+
C
IP+
N+
IP+/N+
D
RG+/IP+
IP+/N+
RG+/N+
IP+
RG+
N+
0
20
40
60
80
% of transitional cell population
E
RG+
IP+
RG+/IP+
F
RG+
N+
RG+/N+
G
IP+
N+
IP+/N+
H
RG+/IP+
IP+/N+
RG+/N+
IP+
RG+
N+
0
20
40
60
% of total cell population
(excluding the transitional cell population)

Figure 3.6. Asymmetric division of RGP to neurons is dominant in the transitional population.
(A-C, E-G) Visualization of cells after PCA and UMAP visualisation colored by co-expression of groups of canonical cell-type markers. Yellow indicates co-expression. (A-C) Transitional cell population. (D) Percentage of cells in the transitional cell cluster displaying co-expression of major cell-type markers. (E-G) Total cell population with transitional population removed. (H) Percentage of cells in the total cell population with transitional population removed displaying co-expression of major cell-type markers.

3.3. Prenatal exposure to MeHg results in cell trajectory alterations

I then conducted trajectory inference using RNA velocity from scVelo [305] to study the full transcriptional dynamics of splicing kinetics. To do this, scVelo utilizes the relative abundance of nascent (unspliced) and mature (spliced) mRNA in each cell as an indicator of the future state of the cell. This method allowed us to describe the direction and speed with which cells transition between clusters. Interestingly, RNA velocity revealed an altered cell lineage trajectory caused by MeHg exposure (Figure 3.7A-F). In control (0ppm MeHg) cortical cells, the RGP1 population shows a 90% positive velocity directed toward RGP2, following symmetrical division, and then differentiating into intermediate progenitors, immature, and mature neurons (Figure 3.7A-B, D-F). In contrast, RGP1 cells in MeHg-exposed cortices showed approximately 50% positive velocity directed toward RGP2 that further differentiate into intermediate progenitors, and 50% negative velocity directed towards the transitional cells, which directly give rise to the population of immature neurons (Figure 3.7A, C-F). These results provide evidence to support that prenatal MeHg exposure may enhance the asymmetric division of RGP1 to generate neurons directly through the transitional cell stage. However, to validate these findings more thoroughly more work is required, including the exploration of alternative techniques.

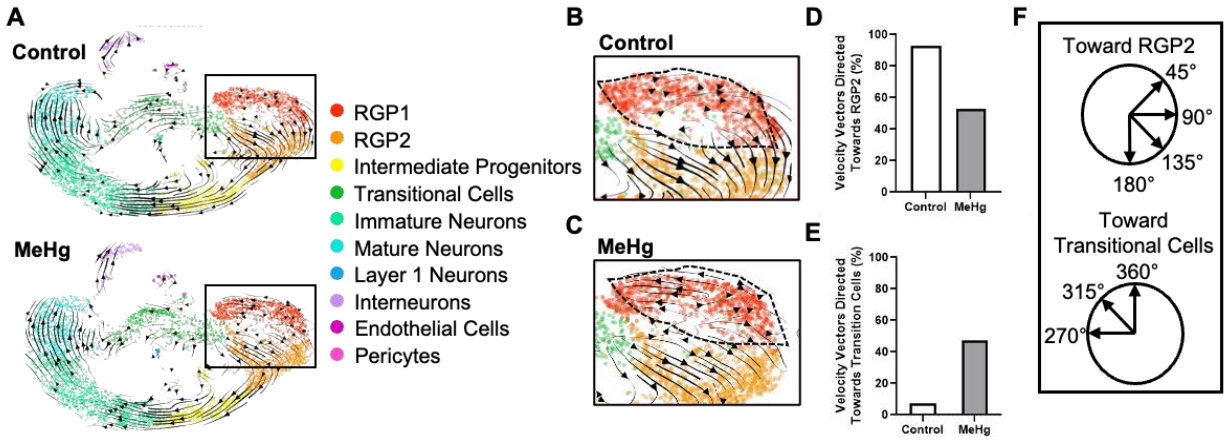

Figure 3.7. Prenatal exposure to MeHg results in cell trajectory alterations.
(A) Velocity vectors for total cell populations in 0ppm (control) and 0.2ppm MeHg, visualized and calculated from RNA velocity using the stochastic model, projected onto UMAP visualizations. (B-C) Enhanced image of velocity vectors in the RGP1 and RGP2 population for both (B) 0ppm and (C) 0.2ppm MeHg. (D) Quantitative analysis of velocity vectors in RGP1 directed towards the RGP2 population between 45° and 180°. (E) Quantitative analysis of velocity vectors in RGP1 directed towards the transitional cell population between 270° and 360°. (F) Parameters used to differentiate vector direction.

I further utilized RNA velocity to order cells along a trajectory that corresponds to their underlying biological process. Pseudotime analysis of the total cell population revealed that clusters including RGP1, RGP2, and the transitional cells in MeHg-exposed cortical cells were in a much later developmental stage than those in control cortical cells (Figure 3.8A), suggesting that prenatal MeHg exposure may accelerate the differentiation process. Next, I used phase portraits generated through scVelo to visualize RNA velocity for specific key cortical development marker genes, *Pax6*, a marker for cortical precursors; *βIII-tubulin* (*Tubb3*), a marker for newborn neurons; and *Tbr1*, a marker for deep layer cortical neurons. A gene with positive RNA velocity is predicted to be upregulated. In opposition, a negative velocity indicates that the gene is predicted to be down-regulated [305]. In the total cell population, I observed that *Pax6* is downregulated in MeHg-exposed RGP1, RGP2, and intermediate progenitors compared to the control. *Tubb3* showed a strong trend towards upregulation in the MeHg-exposed RGP2 population. A more obvious downregulated state for *Tubb3* was observed in the MeHg-exposed transitional cells, immature neurons, and mature neurons relative to the control. Interestingly, corresponding to downregulated *Tubb3* gene, I found that the *Tbr1* gene showed a more upregulated state in MeHg-exposed transitional cells, immature neurons, and mature neurons relative to the control (Figure 3.8B-C). These specific alterations in the key marker genes support our pseudotime analysis results, indicating that MeHg accelerates the neuronal differentiation process.

I then performed RNA velocity and pseudotime analysis on the sub-populated transitional cells as described above. I showed that MeHg also advanced the differentiation process of transitional cells from RGPs towards immature neurons (Figure 3.8D-E). Similar to the total cell population, I confirmed this by visualizing RNA velocity for specific key cortical development

marker genes, *Pax6*, *Tubb3*, *and Tbr1* in the transitional cells. *Pax6* trended towards downregulation in both RGP1 and immature neuron subpopulations in MeHg-exposed transitional cells relative to that in the control group. In contrast, the *Tubb3* gene trended towards upregulation in MeHg-exposed transitional cells. Interestingly, the *Tbr1* gene was not expressed in the control, whereas the *Tbr1* gene was present in the MeHg-exposed transitional cells (Figure 3.8F-G). This result provides further evidence that prenatal MeHg exposure results in premature neuronal differentiation of RGP1 through an increased transitional cell population.

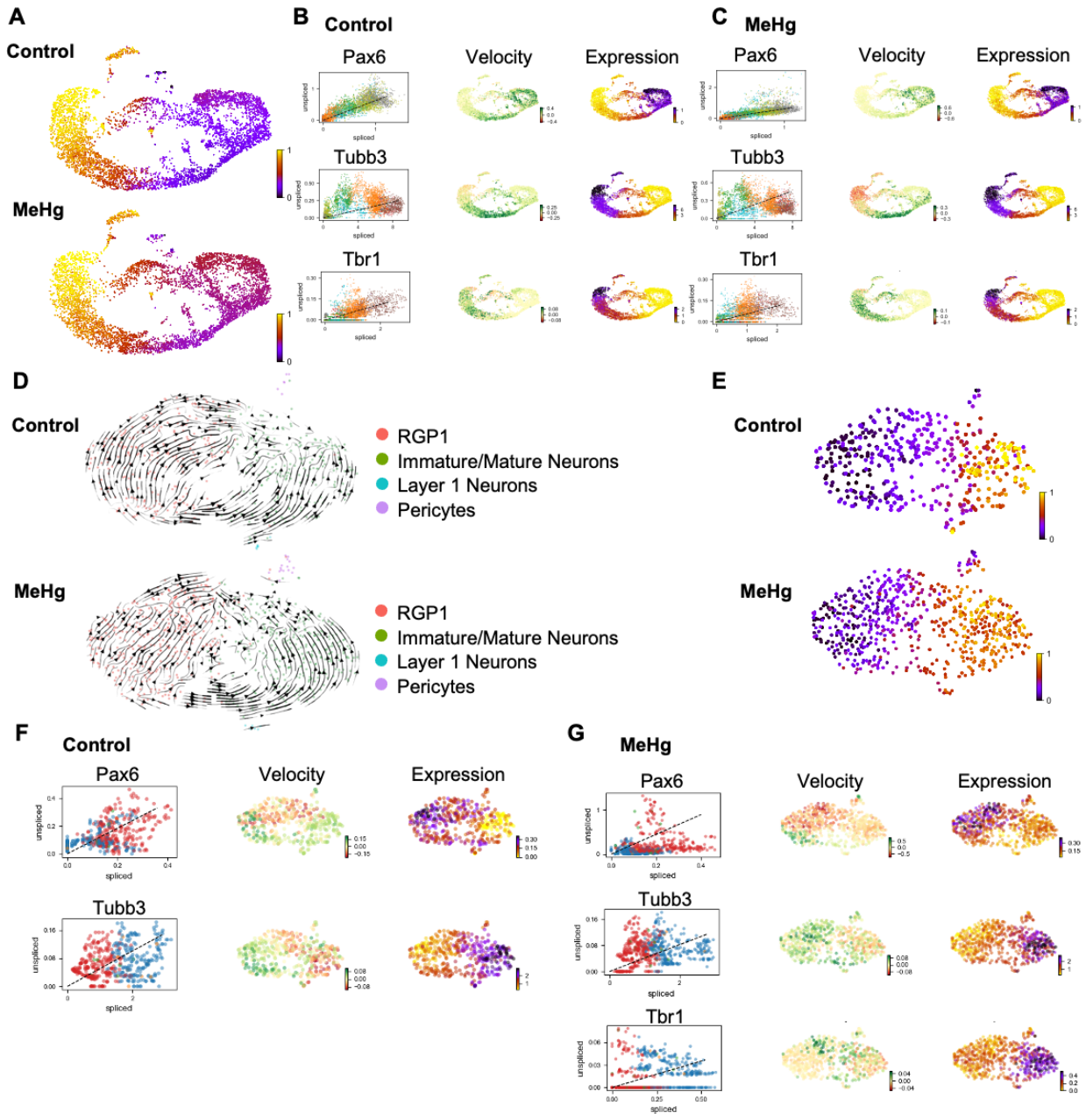
A
Control
MeHg
B
Control
Pax6
Velocity
Expression
Tubb3
Tbr1
C
MeHg
Pax6
Velocity
Expression
Tubb3
Tbr1
D
Control
RGP1
Immature/Mature Neurons
Layer 1 Neurons
Pericytes
MeHg
RGP1
Immature/Mature Neurons
Layer 1 Neurons
Pericytes
E
Control
MeHg
F
Control
Pax6
Velocity
Expression
Tubb3
G
MeHg
Pax6
Velocity
Expression
Tubb3
Tbr1

Figure 3.8. Pseudotime analysis (scvelo).
(A) Pseudotime analysis for 0ppm and 0.2ppm MeHg. (B-C) Phase portraits of marker genes (*Pax6*, *Tubb3*, and *Tbr1*) in (B) 0ppm and (C) 0.2ppm MeHg, calculated from RNA velocity. (D) Velocity vectors for transitional cell populations in both 0ppm and 0.2ppm MeHg treatment groups were visualized and calculated from RNA velocity using the stochastic model and projected onto UMAP visualizations. (E) Pseudotime analysis for the 0ppm and 0.2ppm MeHg treatments within the transitional cell population. (F-G) Phase portraits of marker genes (*Pax6*, *Tubb3*, and *Tbr1*) in the transitional cell population for (F) 0ppm and (G) 0.2ppm MeHg treatments, calculated from RNA velocity.

3.4. Prenatal exposure to MeHg increases the expression of downstream CREB target genes

I next aimed to determine a potential molecular mechanism underlying MeHg-induced neuronal differentiation. I probed for differentially expressed genes analysis using Seurat and found that both *Jund* and *Fos* were significantly upregulated in the MeHg-exposed cortical cells (Figure 3.9A) only in the RGP1 cluster, but not in other cell clusters (Figure 3.9B). Interestingly, both *Jund* and *Fos* are direct downstream gene targets of the transcription factor CREB which is known to play an important role in neurogenesis, synaptogenesis, and cell survival [101–104]. Since MeHg caused robust cell trajectory alterations in the RGP1 population towards the transitional cell cluster, within which asymmetric neuronal differentiation was undertaken to produce neurons, this argues that CREB may be a key regulator to mediate MeHg-induced asymmetric division to directly generate cortical neurons.

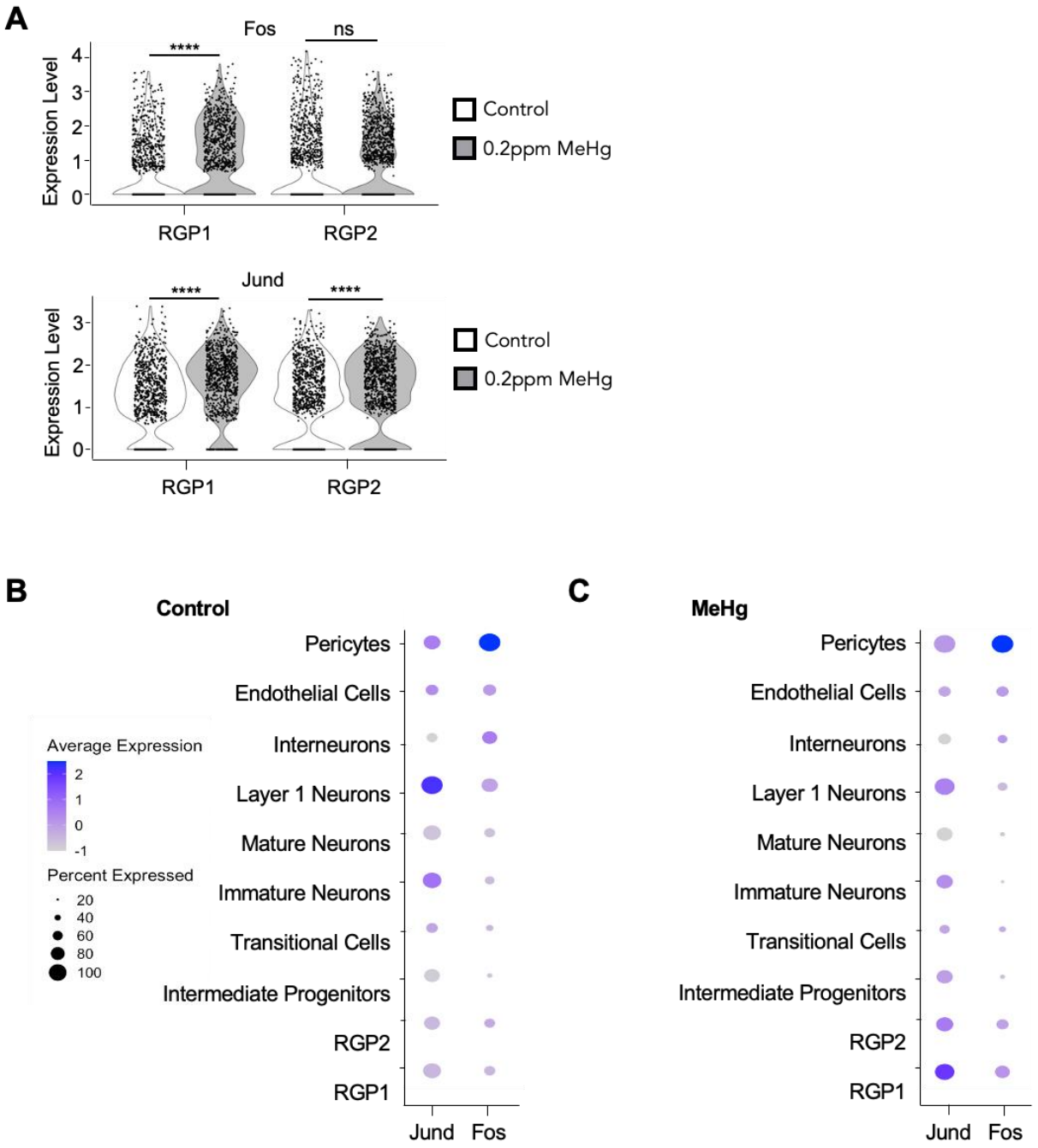

Figure 3.9. Prenatal exposure to MeHg increases the expression of downstream CREB target genes in RGPs.
(A) Violin plot from scRNA-seq showing *Fos* (upper panels) and *Jund* (lower panels) expressions in RGP1 and RGP2 cell populations in control (0ppm) and 0.2ppm MeHg treatment groups, n>800 cells for each group, Mann–Whitney U test, **** P<0.0001, ns (non-significant). (B-C) Dot plot of CREB target gene (*Jund* and *Fos*) expression from scRNA-seq data in pericytes, endothelial cells, interneurons, layer 1 neurons, mature neurons, immature neurons, transitional cells, intermediate progenitors, RGP2, and RGP1 cell populations for (B) control (0ppm) and (C) 0.2ppm MeHg.

Chapter 4: CREB activity/CREB-CBP interaction is an essential molecular mechanism to drive low-dose MeHg-induced premature neuronal differentiation

As mentioned previously, CREB is a key transcription factor that plays an important role in neurogenesis, synaptogenesis, and cell survival [101–104]. Interestingly, human neuroblastoma cells treated with MeHg at nanomolar concentrations showed a significant increase in pS133-CREB, an activated form of CREB, which protected the cells against apoptosis [105]. Consistent with these findings, we dosed cultured embryonic cortical precursors with similar nanomolar concentrations of MeHg and found that it promoted neuronal differentiation of the cortical precursors without causing cell death [126]. Furthermore, as highlighted in Chapter 3, downstream CREB targets *Jund* and *Fos* were upregulated in the RGP1 population following MeHg treatment. In combination, these findings suggest that MeHg might activate CREB in cortical precursors to promote neuronal differentiation.

Metformin is a time-proven FDA-approved drug for the treatment of patients with T2D [270]. Our earlier work showed that metformin was able to promote the differentiation of cortical precursors through the phosphorylation CBP, a co-activator of CREB, at serine 436 [280]. Other work has also shown that pS133-CREB and pS436-CBP are repulsive of each other and cannot co-exist in the brain and the liver [288,291]. Therefore, I hypothesize that metformin treatment could reverse the premature neuronal differentiation caused by low-dose MeHg by initiating protein-protein repulsion between CREB and CBP.

To study this, I will utilize a culture model that mimics *in vivo* cortical development in the dish [302,303]. Dorsal cortical precursors that are isolated from E11-12 CD-1 mice can mimic the three waves of genesis that occur in the cerebral cortex when left in culture. After 3 days in culture, these precursors mature in neurons, after 6 days in culture astrocytes, and after 9 days in culture, they form oligodendrocytes. This effectively mimics neurogenesis, astrogenesis, and oligodendrogenesis, which occurs *in vivo* (Figure 4.1)

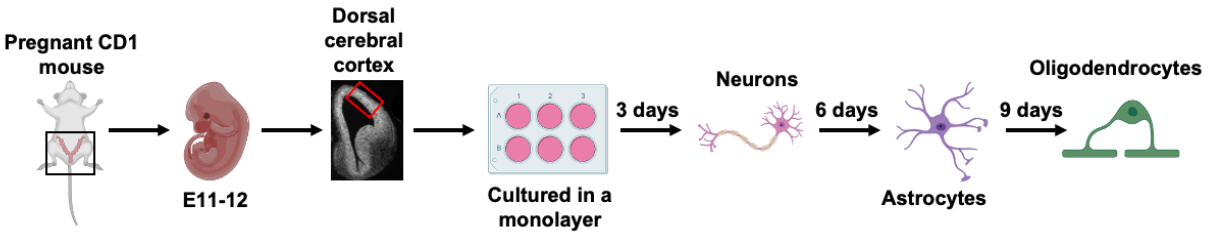

Figure 4.1. *In vitro* model of cortical development.

4.1. Low-dose MeHg increases pS133-CREB and downstream gene targets in cultured cortical precursors

To ask whether CREB is a key regulator to mediate MeHg-induced premature neuronal differentiation, I first examined whether MeHg can increase CREB activity in embryonic cortical precursors. To do that, I performed a culture experiment using cortical precursors isolated from E11-12 embryos and cultured these cortical precursors in the absence and presence of 250nM MeHg for 4 h (Figure 4.2A). Western blotting analysis showed that pS133-CREB, an activated form of CREB, was significantly upregulated in the cortical precursors exposed to 250nM MeHg, a low-dose concentration used in our previous work to promote neuronal differentiation of E12 cortical precursors [126] (Figure 4.2B-D). Interestingly, I also observed that MeHg significantly reduced pT410/403-aPKC, an activated form of aPKC (Figure 4.2E-G). Finally, MeHg altered CREB and aPKC phosphorylation/activation without altering their total protein expressions (Figure 4.2D, G).

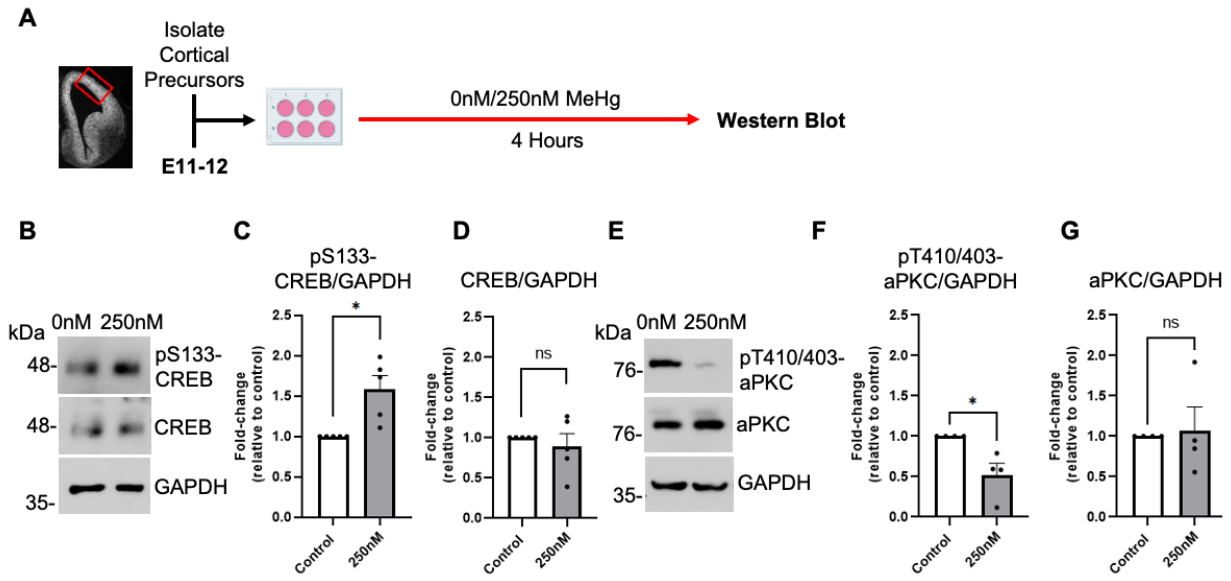

Figure 4.2. MeHg increases pS133-CREB in cultured cortical precursors.
(A) Schematic of cortical precursors isolated from E11-12 CD1 mice, created with BioRender.com. Cells were exposed to 0nM (control) or 250nM MeHg for 4 h, at which point they were lysed for western blot. (B-G) Western blot analysis of E12 cortical precursors cultured for 4 h in the absence or presence of 250nM MeHg. (B, E) Blots were probed for pS133-CREB, pT410/403-aPKC, total CREB, total aPKC and GAPDH as a loading control. (C-D) Quantitative analysis of (C) pS133-CREB and (D) total CREB over GAPDH. n=5 independent experiments, student t-test, *p<0.05, ns (non-significant) (F-G) Quantitative analysis of (F) pT410/403-aPKC and (G) aPKC over GAPDH, n=4 independent experiments, student t-test, *p<0.05, ns (non-significant). Error bars indicate the SEM.

To confirm the activation of downstream CREB targets (*Jund* and *Fos*) previously identified via the scRNA-seq analysis conducted in Chapter 3, I performed RT-qPCR on the cortical precursors in the absence and presence of 250nM MeHg for 20-30 minutes (Figure 4.3A). 250nM MeHg significantly increased the expression of *FosB* (Figure 4.3B) relative to the control. Despite not being significant, there was a positive trend for *upregulating Jund* and *cFos* expression following MeHg treatment (Figure 4.3C-D).

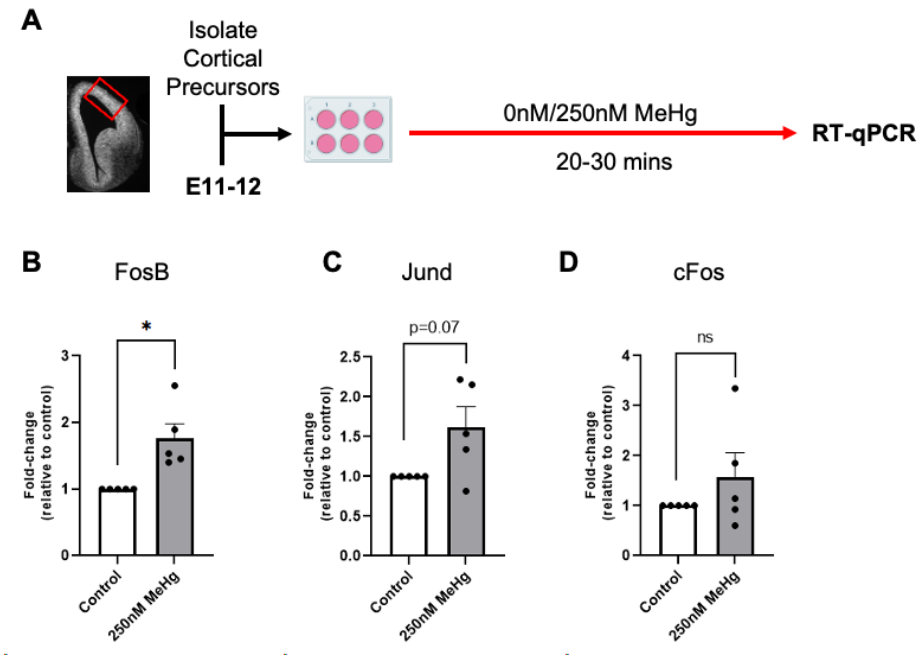

Figure 4.3. MeHg increases downstream pS133-CREB gene targets in cultured cortical precursors.
(A) Schematic of cortical precursors isolated from E11-12 CD1 mice, created with BioRender.com. Cells were exposed to 0nM (control) or 250nM MeHg for 20-30 min, at which point they were lysed. Quantitative analysis of (B) *FosB*, (C) *Jund*, and (D) *cFos* expression, over GAPDH, relative to control. n=5 independent experiments, student t-test, *p<0.05, ns (non-significant). Error bars indicate the SEM.

4.2. Metformin alleviates increased CBP-CREB pS133 interaction caused by low-dose MeHg

As previously highlighted, p-S133 CREB is known to increase the protein-protein interaction between CBP and CREB, while pS436-CBP is also known to increase protein-protein interaction between two proteins as a compensatory mechanism when pS133-CREB is reduced [289]. Furthermore, both pS133-CREB and pS436-CBP cannot co-exist [288,291], possibly due to the negative charge on phosphorylation groups. To test if co-treatment of metformin and MeHg can reverse the premature differentiation caused by MeHg, by initiating repulsion between pS133-CREB and pS436-CBP, I used a PLA assay to assess intranuclear interactions between CBP and pS133-CREB at the single-cell level (Figure 4.4A). The results showed that the interactions between CBP and pS133-CREB were significantly enhanced by 250nM MeHg treatment alone, while co-treatment with metformin eliminated the increased interactions (Figure 4.4B-C). Thus, metformin, an FDA-approved drug, has the potential to reverse MeHg-induced neuronal differentiation through repulsive interaction between CREB and CBP in cultured cortical precursors.

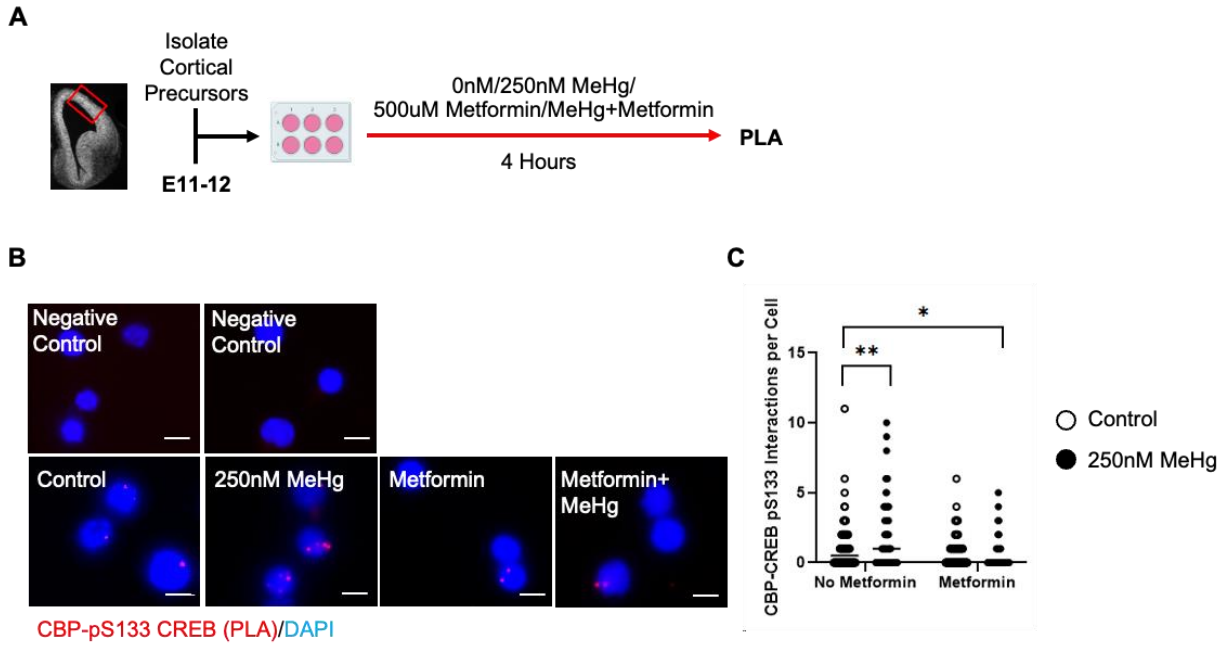

Figure 4.4. Metformin alleviates increased CBP-CREB pS133 interaction caused by low-dose MeHg.

(A) Schematic of cortical precursors isolated from E11-12 CD1 mice, created with BioRender.com. Cells were exposed to 0nM (control) or 250nM MeHg with no metformin or metformin (500µM) for 4 h, at which point they were lysed for PLA analysis. (B) Images of PLA^+ interactions (lower panels, red) between pS133-CREB and CBP, counterstained with Hoechst (blue) in cultured cortical precursors of four treatment groups i) control (0ppm MeHg and 0µM metformin), ii) 250nM MeHg, iii) 500µM metformin, and iv) co-treatment of 500µM metformin + 250nM MeHg, scale bar: 5µm. Images of negative control PLA (upper panels) in the absence of anti- pS133-CREB and anti-CBP (upper left) or absence of PLA probes (upper right). (C) Quantitative analysis of pS133- CREB and CBP interaction signals (red) within nuclei (blue). n=100 cells/group, n=4 independent experiments, Two-way ANOVA (group × metformin interaction $F(1, 396) = 11.34$, $P = 0.0008$, group $F(1, 396) = 1.463$, $P = 0.2272$, metformin $F(1, 396) = 25.01$, $p<0.0001$, n = 400) with post hoc test, *$p<0.05$, **$p<0.01$. Error bars indicate the SEM.

4.3. Metformin eliminates premature neuronal differentiation caused by low-dose MeHg *in vitro*

To test whether metformin can eliminate MeHg-induced neuronal differentiation, I utilized a E11-E12 cortical precursor culture for 3 days in the absence and presence of 250nM MeHg [126], and with or without 500μM metformin [280] (Figure 4.5A). Treatment with 250nM MeHg alone increased cortical precursor differentiation, manifested by an increased percentage of newborn neurons (βIII-tubulin$^+$) and a reduced proportion of cortical precursors (Pax6$^+$ and Sox2$^+$) in culture (Figure 4.5B-F). Additionally, MeHg treatment reduced the proliferation of cortical precursors (Ki67$^+$) (Figure 4.5G). Similarly, treatment with 500μM metformin alone increased the percentage of newborn neurons (βIII-tubulin$^+$) population and reduced the percentage of cortical precursors population (Figure 4.5B-F), marked by Pax6 and Sox2, as previously reported [281]. Interestingly, the co-treatment with both 250nM MeHg and 500μM metformin reversed the increased percentage of newborn neurons, as well as the reduced cortical precursor population and proliferation caused by MeHg alone (Figure 4.5B-G).

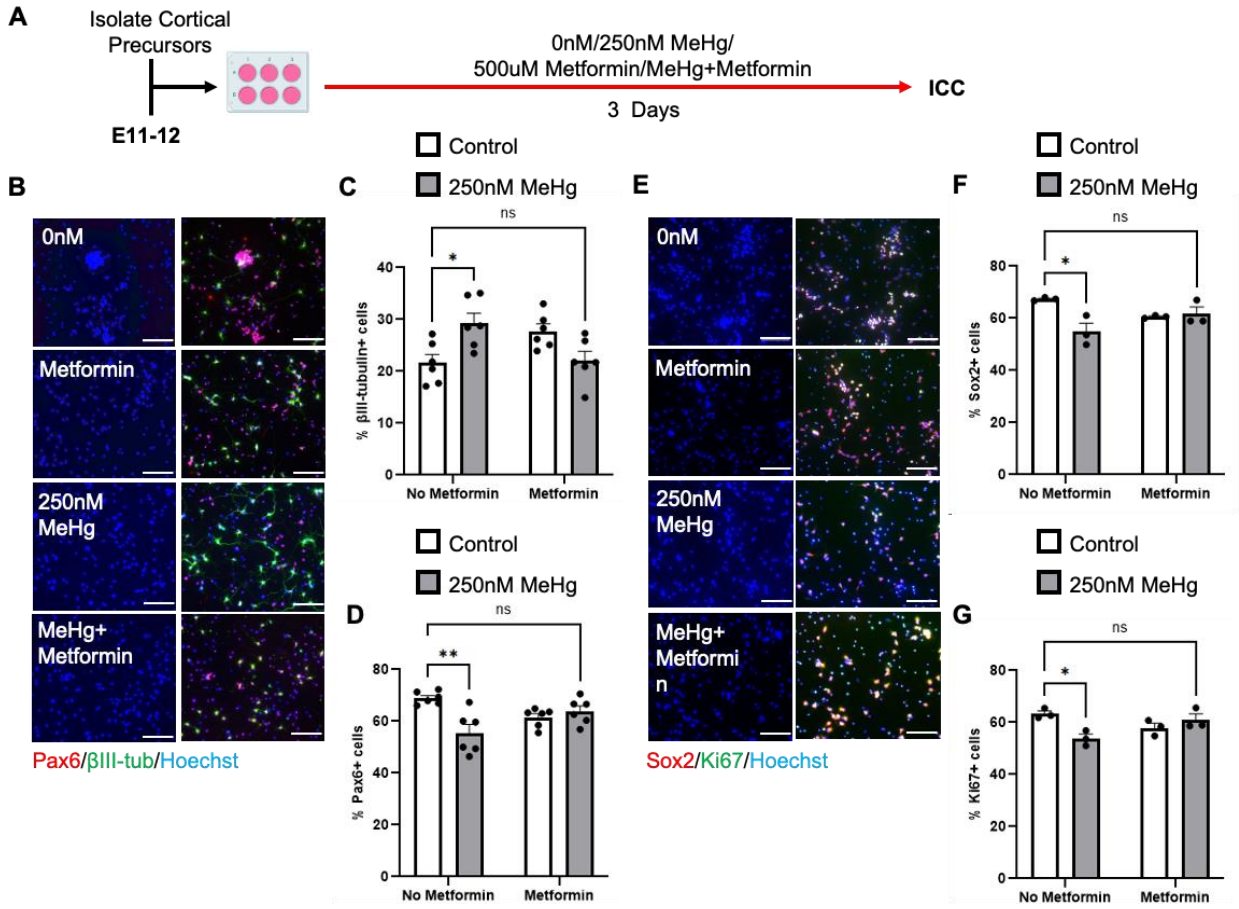

Figure 4.5. Metformin eliminates premature neuronal differentiation caused by low-dose MeHg *in vitro*.

(A) Schematic of cortical precursors isolated from E11-12 CD1 mice, created with BioRender.com. Cells were exposed to four conditions: i) control (0ppm MeHg+0µM metformin), ii) 250nM MeHg, iii) 500µM metformin, iv) co-treatment of 250nM MeHg + 500µM metformin for 3 days, followed by immunocytochemical analysis. (B, E) Images of cortical precursors after 3 days in culture treated with four conditions mentioned in (A), immunostained for Pax6 (B, red), βIII-tubulin (B, green), Ki67 (E, green), Sox2 (E, red) and counterstained for Hoechst (blue). Scale bar: 30µm. (c) Quantitative analysis of βIII-tubulin^{+} cells, n=6 independent experiments, Two-way ANOVA (group × metformin interaction $F(1, 20) = 15.28$, $P = 0.0009$, group $F(1, 20) = 0.3370$, $P = 0.5680$, metformin $F(1, 20) = 0.09295$, $P = 0.7636$, n = 24). (D) Quantitative analysis of Pax6^{+} cells, n=6 independent experiments, Two-way ANOVA (group × metformin interaction $F(1, 20) = 13.99$, $P = 0.0013$, group $F(1, 20) = 6.652$, $P = 0.0179$, metformin $F(1, 20) = 0.04803$, $P = 0.8287$, n = 24). (F) Quantitative analysis of Sox2^{+} cells, n=3 independent experiments, Two-way ANOVA (group × metformin interaction $F(1, 8) = 10.05$, $P = 0.0132$, group $F(1, 8) = 7.171$, $P = 0.0280$, metformin $F(1, 8) = 0.0002320$, $P = 0.9882$, n = 12). (G) Quantitative analysis of Ki67^{+} cells. n=3 independent experiments, Two-way ANOVA (group × metformin interaction $F(1, 8) = 12.89$, $P = 0.0071$, group $F(1, 8) = 3.335$, $P = 0.1053$, metformin $F(1, 8) = 0.2942$, $P = 0.6023$, n = 12) with post hoc test, $^{**}p<0.01$, $^{*}p<0.05$, ns (non-significant). Error bars indicate the SEM.

4.4. Metformin eliminates premature neuronal differentiation caused by MeHg exposure *in vivo*

Post-doctoral fellow Dr. Joseph Leung previously showed that prenatal exposure to low-dose MeHg significantly increased the number of DCX^+ neuroblasts, specifically in the VZ, at the expense of proliferating $Pax6^+$ cortical precursors (Appendix Figure 1A-F). This was further confirmed by the scRNA-seq dataset, which showed that MeHg caused a trajectory change to favor asymmetric division of the RGP1 population, as opposed to symmetric division of the RGP1 population to produce RGP2 (Figure 3.7A-F).

Here, I performed *in vivo* experiments to test whether metformin (4mg/ml) co-treatment with 0.2ppm MeHg via drinking water from E0 to E15 can eliminate MeHg-induced premature neuronal differentiation *in vivo* (Figure 4.6A). Here, I examined the number of $Pax6^+/Ki67^+$ and $Sox2^+/Mcm2^+$ proliferating cortical precursors. I found that co-treatment of MeHg with metformin restored MeHg-reduced proliferating cortical precursors, marked by $Pax6^+/Ki67^+$ and $Sox2^+/Mcm2^+$ populations (Figure 4.6B-H). Prenatal MeHg did not change the total number of $Pax6^+$ (Figure 4.6B, E) or total $Sox2^+$ (Figure 4.6F, H) RGPs. This is consistent with the scRNA-seq dataset which showed that MeHg caused trajectory change to favor asymmetric division of the RGP1 population. Furthermore, co-treatment with metformin and MeHg erased MeHg-increased DCX^+ immature neurons within the VZ (Figure 4.6I-J). Thus, metformin treatment was able to eliminate the premature neuronal differentiation caused by MeHg exposure.

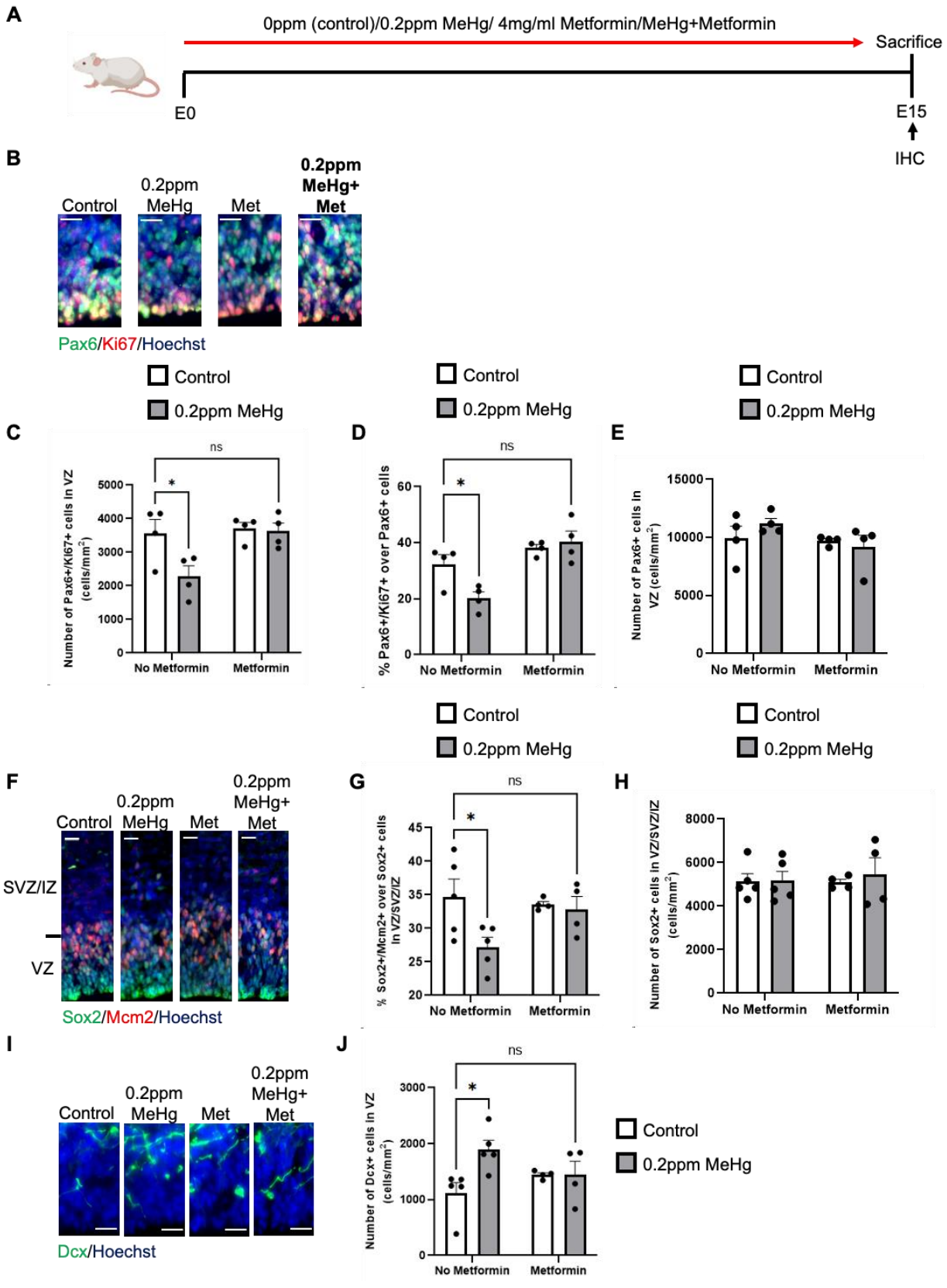
A
0ppm (control)/0.2ppm MeHg/ 4mg/ml Metformin/MeHg+Metformin
Sacrifice
E0
E15
IHC
B
Control
0.2ppm MeHg
Met
0.2ppm MeHg+ Met
Pax6/Ki67/Hoechst
Control
0.2ppm MeHg
C
Number of Pax6+/Ki67+ cells in VZ (cells/mm²)
ns
*
No Metformin
Metformin
D
% Pax6+/Ki67+ over Pax6+ cells
E
Number of Pax6+ cells in VZ (cells/mm²)
F
SVZ/IZ
VZ
Sox2/Mcm2/Hoechst
G
% Sox2+/Mcm2+ over Sox2+ cells in VZ/SVZ/IZ
H
Number of Sox2+ cells in VZ/SVZ/IZ (cells/mm²)
I
Dcx/Hoechst
J
Number of Dcx+ cells in VZ (cells/mm²)

Figure 4.6. Metformin eliminates premature neuronal differentiation caused by MeHg exposure *in vivo*.
(A) Schematic of prenatal exposure of MeHg to pregnant mice, created with BioRender.com. Pregnant mice were exposed to four conditions: i) control (0ppm MeHg +0mg metformin, ii) 0.2ppm MeHg, iii) 4mg/ml metformin, iv) 0.2ppm MeHg + 4mg/ml metformin. Treatment was administered through drinking water to pregnant mice starting at E0 until E15. At E15 brains were collected for immunohistochemistry. (B, F, I) Images of E15 cerebral cortex sections from embryos receiving four condition treatments mentioned in (H), immunostained for Pax6 (B, green), Ki67 (B, red) or Sox2 (F, green), Mcm2 (F, red), or DCX (I, green) and counterstained for Hoechst (blue). Scale bar: 20μm. (C-D) Quantitative analysis of the number and proportion of $Pax6^+/Ki67^+$ proliferating cortical precursors in the VZ. C: Two-way ANOVA (group × metformin interaction $F(1, 12) = 4.060$, $P = 0.0669$, group $F(1, 12) = 5.253$, $P = 0.0408$, metformin $F(1, 12) = 6.156$, $P = 0.0289$, $n = 16$). D: Two-way ANOVA (group × metformin interaction $F(1, 12) = 6.461$, $P = 0.0259$, group $F(1, 12) = 2.961$, $P = 0.1109$, metformin $F(1, 12) = 20.79$, $P = 0.0007$, $n = 16$) with post hoc test, $^*p<0.05$, ns (non-significant). (E) Quantitative analysis of the number of $Sox2^+$ cortical precursors within VZ/SVZ/IZ, n=4-5 embryos/group. (G) Quantitative analysis of the number of $Sox2^+/Mcm2^+$ proliferating RGPs within VZ and SVZ/IZ, Two-way ANOVA (group × metformin interaction $F(1, 14) = 3.167$, $P = 0.0969$, group $F(1, 14) = 4.683$, $P = 0.0482$, metformin $F(1, 14) = 1.379$, $P = 0.2599$, $n = 18$) with post hoc test, $^*p<0.05$, ns (non-significant). (H) Quantitative analysis of the number of $Pax6^+$ cortical precursors within VZ, n=4 embryos/group. (J) Quantitative analysis of the number of DCX^+ cells in the VZ, Two-way ANOVA (group × metformin interaction $F(1, 14) = 4.817$, $P = 0.0455$, group $F(1, 14) = 4.858$, $P = 0.0448$, metformin $F(1, 14) = 0.1290$, $P = 0.7248$, $n = 18$) with post hoc test, $^*p<0.05$, ns (non-significant). These quantifications (C-E, G-H, J) were determined from cortical sections similar to those shown in (B, F, I). n=4-5 embryos per group. Error bars indicate the SEM.

4.5. Metformin eliminates the increased cortical thickness caused by MeHg exposure

Previously, Dr. Joseph Leung demonstrated that prenatal treatment with 0.2ppm MeHg caused increased CP thickness (Appendix Figure 1I). I aimed to determine if co-treatment with both metformin and 0.2ppm MeHg could also reverse this phenomenon *in vivo*. I measured the cortical thickness of the VZ, SVZ/IZ, and CP in all four groups (Figure 4.7A). Interestingly, I observed that MeHg alone group showed a significant increase in the thickness of the CP relative to the control group. At the same time, co-treatment with metformin and MeHg exhibited a similar thickness of CP as the control group (Figure 4.7B-C).

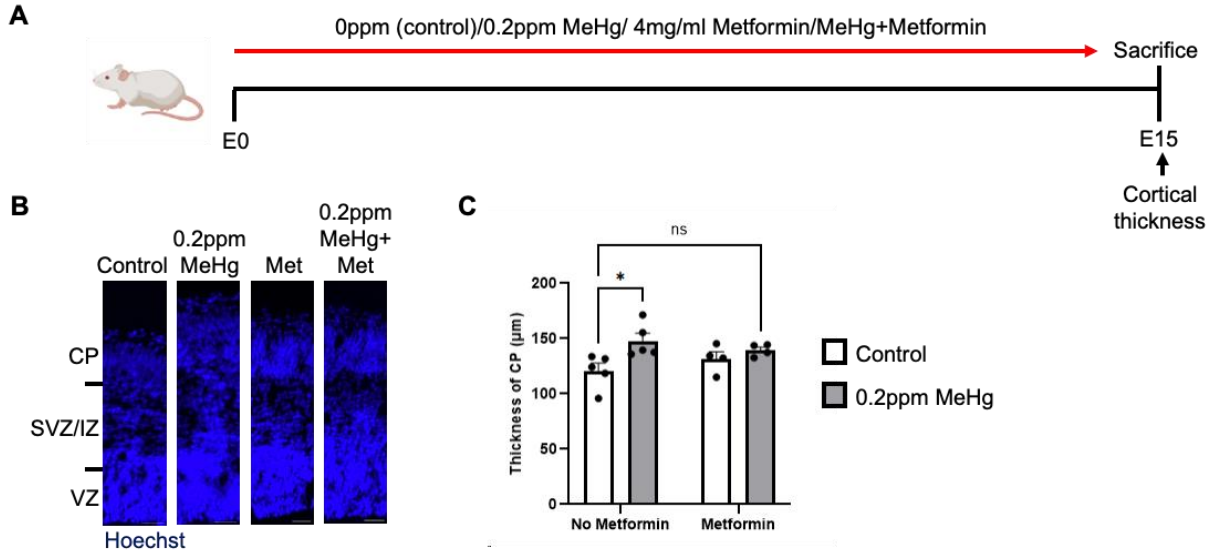

Figure 4.7. Metformin eliminates the increased cortical thickness caused by MeHg exposure.

(A) Schematic of prenatal exposure of MeHg to pregnant mice, created with BioRender.com. Pregnant mice were exposed to four conditions: i) control (0ppm MeHg +0mg metformin, ii) 0.2ppm MeHg, iii) 4mg/ml metformin, iv) 0.2ppm MeHg + 4mg/ml metformin. Treatment was administered through drinking water to pregnant mice starting at E0 until E15. (B) Images of E15 cerebral cortex sections from embryos receiving 0ppm and 0.2ppm MeHg treatment, counterstained for Hoechst (blue). Scale bar: 40µm. (C) Two-way ANOVA (MeHg × metformin interaction $F(1, 14) = 2.401$, $P = 0.1436$, MeHg $F(1, 14) = 7.810$, $P = 0.0143$, metformin $F(1, 14) = 0.04262$, $P = 0.8394$, $n = 18$) with post hoc test, $^*p<0.05$, ns (non-significant), determined from coronal sections similar to those shown in E. Error bars indicate the SEM.

4.6. *In vitro* Hg analysis

To confirm MeHg exposure in our cortical precursor culture, Hg analysis was conducted using a direct thermal decomposition Hg analyzer. The theoretical amount of Hg was calculated and compared to the measured amount. Hg analysis of treated groups are consistent with calculated theoretical Hg amounts (Table 4.1).

Table 4.1. Theoretical Hg dosage and empirical Hg measurements.

Treated (nM)	Theoretical (ng)	Average media (ng)	Average wash (ng)	Experimental measurements (media x 5 + wash) (ng)
0	0.000000	0.0596	0.0344	0.3324
250	25.0738	4.3468	0.2814	22.0154

4.7. *In vivo* Hg analysis

Following prenatal exposure to treated drinking water I measured the amount of water consumed by the pregnant mice (Figure 4.8A-B) and Hg levels in the fetal brains to confirm that E15 brains exposed to 0.2ppm MeHg treatment alone had similar levels of Hg accumulation compared to the co-treatment group (Figure 4.8A, C). I found no significant difference in brain Hg levels between MeHg-treated groups (Figure 4.8C). These results support that metformin treatment via drinking water does not affect Hg accumulation in the fetal brain but directly counteracts MeHg-perturbed cortical development.

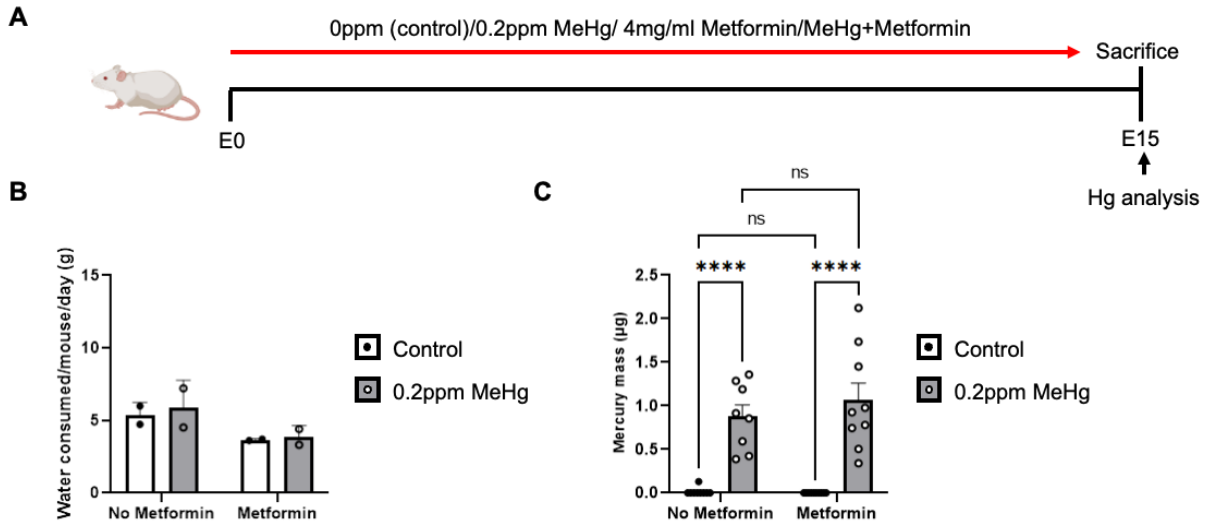

Figure 4.8. Hg analysis.
(A) Schematic of prenatal exposure of MeHg to pregnant mice, created with BioRender.com. Pregnant mice were exposed to four conditions: i) control (0ppm MeHg +0mg metformin, ii) 0.2ppm MeHg, iii) 4mg/ml metformin, iv) 0.2ppm MeHg + 4mg/ml metformin. Treatment was administered through drinking water to pregnant mice starting at E0 until E15. (B) Average drinking water consumed per mouse per day over gestation was assessed by the calculation (initial water (g) – final water (g)/gestation days/# of mice in cage). **(**C) Quantitative analysis of mercury mass from hemisphere measurements collected at E15, n=8-10 embryos/group, Two-way ANOVA (group × metformin interaction $F(1, 32) = 0.7741$, $P=0.3855$, group $F (1, 32) = 69.74$, $P<0.0001$, metformin $F (1, 32) = 0.5694$, $P=0.4560$) with post hoc test, ****$P<0.0001$, ns (non-significant). Error bars indicate the SEM.

Chapter 5: Low-dose prenatal MeHg exposure in rodents promotes ASD-like behaviours in early adulthood

Embryonic cerebral cortex development is vulnerable to environmental insults (such as drugs, alcohol, and environmental toxicants), potentially leading to neurodevelopmental disorders, including ASD [306,307]. While most work investigating the relationship between MeHg exposure and perturbed neurological function has been focused on cell apoptosis, oxidative stress, and mitochondrial dysfunction [126,308–310], the effects of prenatal low-dose MeHg exposure on cortical development and its underlying mechanism remain elusive. Our recent work revealed that MeHg treatments at sub-micromolar (nanomolar) levels induced premature neuronal differentiation of cultured embryonic cortical precursors without causing cell death [126]. Post-doctoral fellow Dr. Joseph Leung later confirmed this effect *in vivo* following prenatal treatment with 0.2ppm MeHg from E0 to E15 (Appendix Figure 1A-F). Interestingly, overproduction of neurons has been found in mouse models of ASD [204,205], ASD organoid models [205,311], and human ASD patients [194,195].

ASD is a neurodevelopmental disorder that is characterized by impairments in language, communication, and sociability combined with restricted and repetitive behaviours [145]. Huguet and Bourgeron (2016) suggested that there is a large portion of ASD, ~50%, that is non-genetic [154]. This suggests that other factors, such as environmental insults, could play a role in disorder onset. As previously introduced, the current literature on the relationship between prenatal Hg exposure and ASD onset is inconsistent [233–255]. This may be due to the fact that humans are most commonly exposed to MeHg via fish consumption. Fish contain beneficial long-chain polyunsaturated omega-3 fatty acids and Se, both of which can have positive effects. Polyunsaturated omega-3 fatty acids are known to aid prenatal development [258], and both provide beneficial effects against Hg toxicity [11,13–16]. Based on this, the effect of prenatal MeHg exposure

via maternal fish consumption may have a diminished effect. Overall, using rodent models to study the isolated effect of MeHg may be critical to further our understanding.

To determine the long-term behavioural consequences of prenatal exposure to low-dose MeHg, I administered 0ppm and 0.2ppm MeHg via drinking water from E0 to birth. No difference in average amount of drinking water consumed was observed between conditions (Figure 5.1). At P7 and P9, I probed for impaired ultrasonic USV, and at 2 months old, a battery of behavioural tests were performed on the offspring to probe for additional ASD-related behaviours (Figure 5.2).

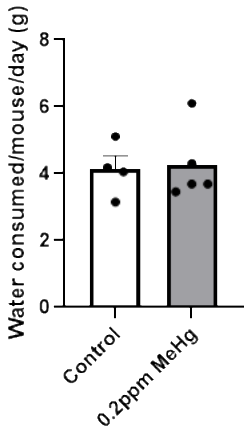

Figure 5.1. Average drinking water consumed by pregnant mice.
Average drinking water consumed per mouse per day over gestation was assessed by the calculation (initial water (g) – final water (g)/gestation days/# of mice in cage).

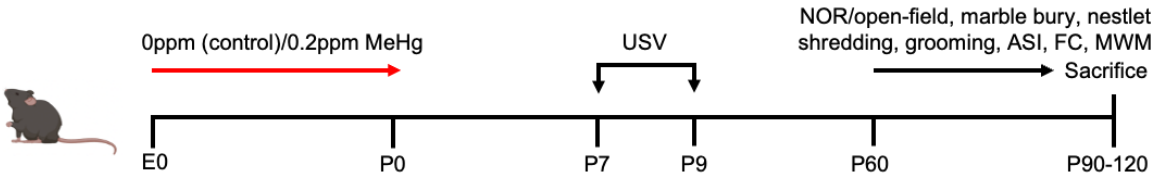

Figure 5.2. Long-term low-dose prenatal MeHg methodology.
Schematic of prenatal exposure to MeHg in pregnant mice, created with BioRender.com. 0ppm (control) and 0.2ppm MeHg was administered through drinking water to pregnant mice starting at E0 until birth. n=2-5 litters/group.

5.1. Prenatal exposure to 0.2ppm MeHg impairs communication

The triad of impairment for ASD diagnosis consists of restrictive repetitive behaviour, deficits in social interaction and communication [145]. To probe for impaired communication that is typically observed in individuals with ASD, I assessed USVs at P7 and P9. I found that P9 pups following prenatal MeHg exposure exhibited a reduced number of USVs (Figure 5.3A-B) and a decreased length per call (Figure 5.3C). This indicates that prenatal treatment with low-dose MeHg impairs communication at early postnatal. No change in call number or call length was observed at P7 (Figure 5.3B-C). No change in max peak frequency was observed at P7 or P9 (Figure 5.3D).

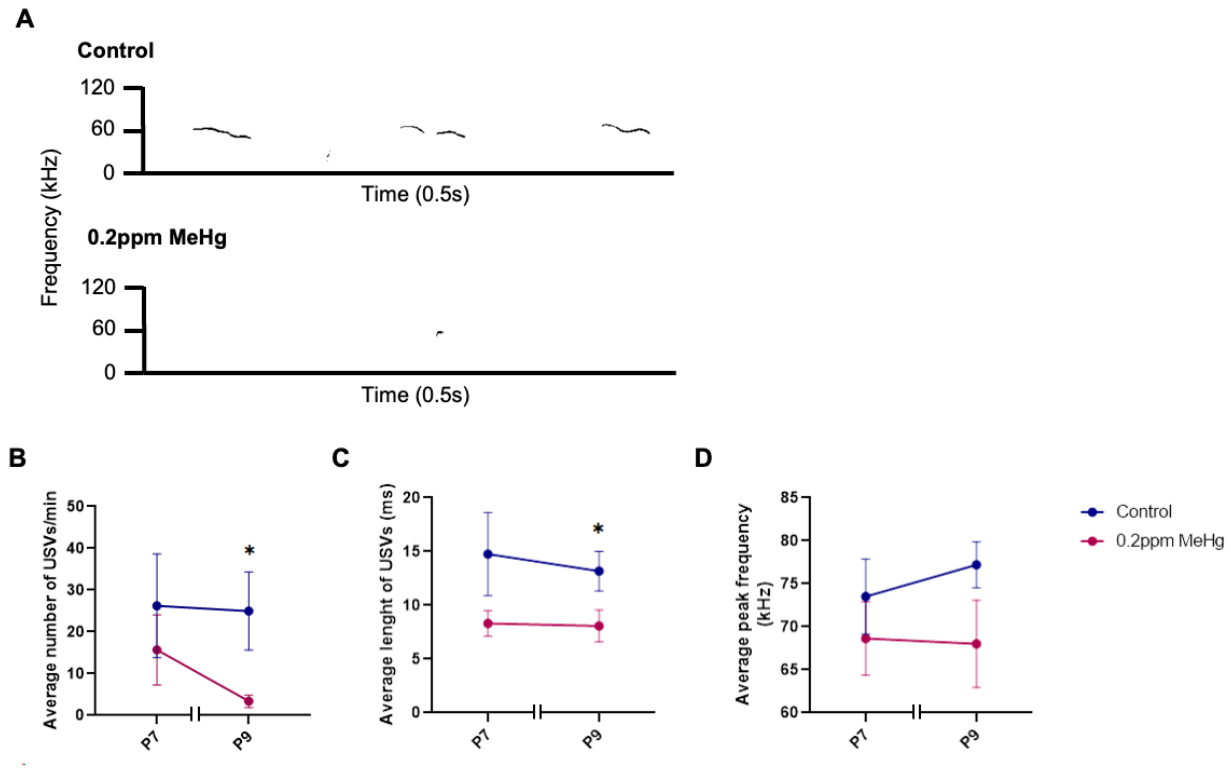

Figure 5.3. Prenatal treatment with 0.2ppm MeHg impairs communication.
USV analysis was conducted on P7 and P9 pups (A) representative spectrograms of control and MeHg-treated mice at P9. (B) The average number of calls/min, n=11 animals/group, Mann–Whitney U test, *$p<0.05$, (C) average call length per call, (D) and max peak frequency was analyzed, n=10 animals/group, student t-test, *$p<0.05$. Error bars indicate the SEM.

5.2. Prenatal exposure to 0.2ppm MeHg increases repetitive behaviour

To probe for repetitive behaviours, I performed the Marble Burying test. Here, 20 marbles were arranged-on top of loosely packed woodchips, and the mice were given 30 min to interact with the environment. A marble was scored as buried if two-thirds of its surface area was covered by bedding (Figure 5.4A). I observed significantly more marbles buried by the 0.2ppm MeHg-treated mice (Figure 5.4B), with no changes in locomotion (Figure 5.5A-B) or anxiety (Figure 5.5C-E) measured using the Open-Field test. Additionally, I performed the Nestlet Shredding test, another task used to indicate repetitive behaviour. Here, mice prenatally treated with either 0.2ppm MeHg or 0ppm MeHg (control) were given 1.5h to interact with one cotton nestlet in an empty cage (Figure 5.4C). The MeHg group showed a trend to increase the percentage of nestlet shredded at the end of 1.5h (Figure 5.4D). In combination, these tests reveal that prenatal MeHg exposure increases repetitive behaviours, a key indicator of ASD.

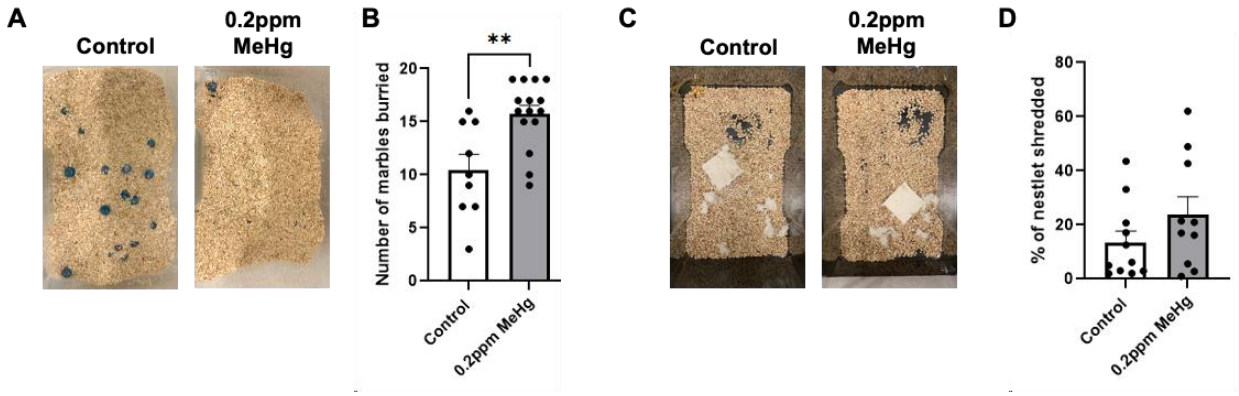

Figure 5.4. Prenatal treatment with 0.2ppm MeHg increases repetitive behaviour. (A-B) The Marble Burying test assessed the number of marbles buried after 30 min interaction time. (A) Representative images for both control and 0.2ppm MeHg. (B) Quantitative analysis of the number of marbles buried in the cage. n=9-15 animals/group, student t-test, ** $p<0.01$. (C-D) The Nestlet Shredding test assessed the percentage of nestlet shredded after 1.5 h interaction time. (C) Representative images for both control and 0.2ppm MeHg. (D) Percentage of nestlet shred after 1.5h for control and 0.2ppm MeHg groups. n=10-11 animals/group. Error bars indicate the SEM.

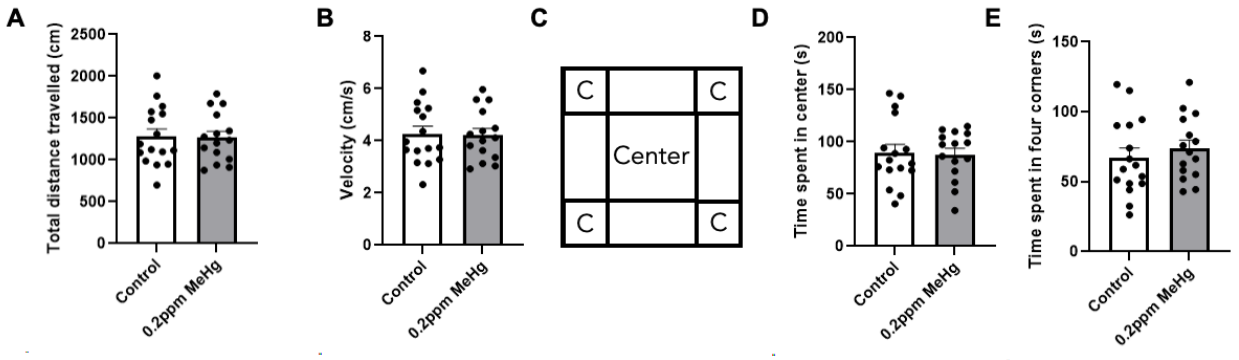

Figure 5.5. Prenatal treatment with 0.2ppm MeHg does not alter anxiety or locomotion. (A) Open-field data for total distance travelled (cm). n=15-16 animals/group. (B) Open-field data for mean velocity (cm/s). n=15-16 animals/group. (C) Schematic of open-field boundaries used to assess anxiety. (D-E) quantitative analysis of time spent in the (D) center and (E) four corners of the open-field. n=15-16 animals/group. Error bars indicate the SEM.

5.3. Prenatal exposure to 0.2ppm MeHg impairs sociability

To assess differences in sociability, I performed the ASI test (Figure 5.6A). The control females spent significantly more time in the interaction zone with the novel mouse in the mesh cage relative to an empty cage. In contrast, the MeHg-treated females did not show a significant change in interest in the novel mouse (Figure 5.6B). MeHg-treated females also spent significantly less time interacting with the novel mouse when compared to control females (Figure 5.6C). This reveals that prenatal MeHg exposure reduces the sociability of mice, a key behavioural feature of ASD. Interestingly, this test is highly sex-dependent. Both control and MeHg-treated male mice did not show an increased interaction time with a novel mouse (Figure 5.6D).

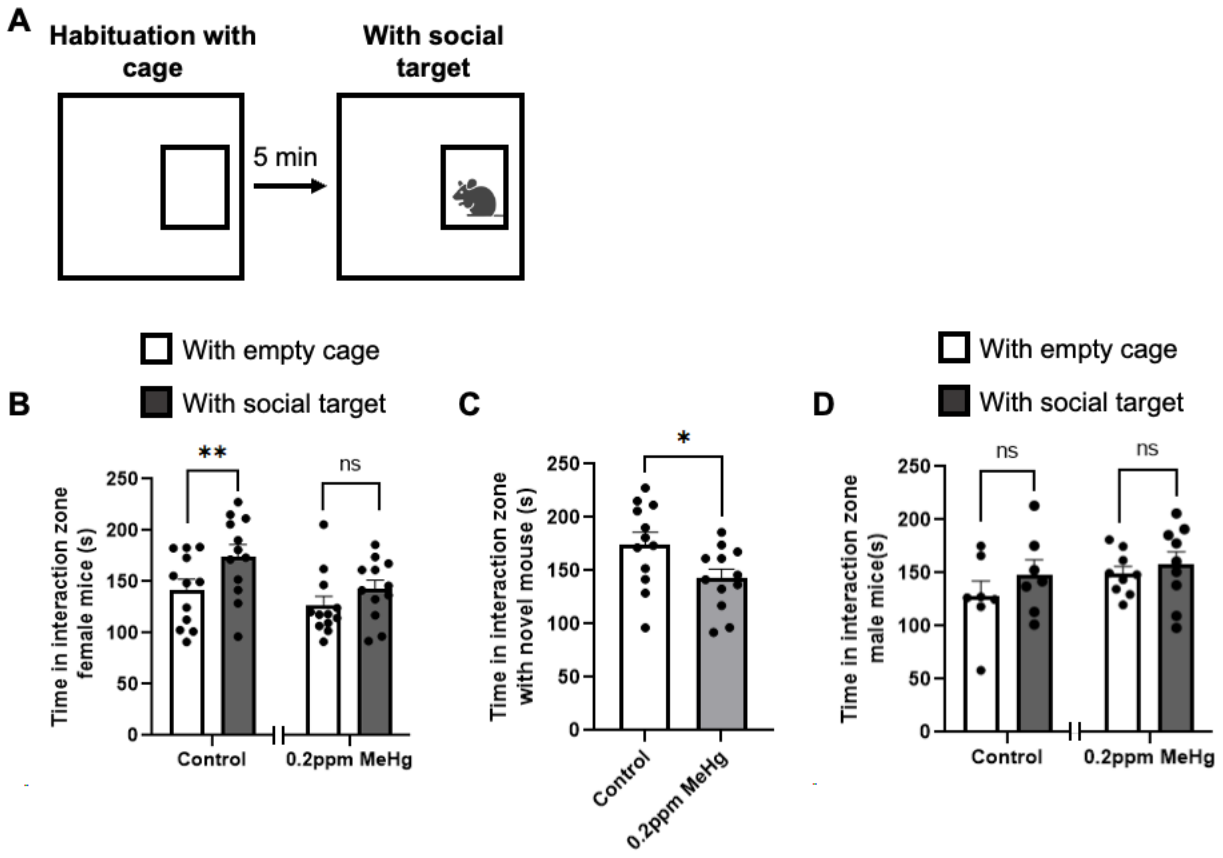

Figure 5.6. Prenatal treatment with 0.2ppm MeHg impairs sociability.
(A) The ASI test assessed the amount of time that testing mice spent in the interaction zone with either an empty wire-mesh cage or the cage with a novel mouse of the same strain, sex, and age. (B) The time spent in the interaction zone for female mice, n=12 animals/group, student t-test, ** $p<0.01$, ns (non-significant). (C) Time spent in interaction zone with novel mouse for female mice, n=12 animals/group, student t-test, * $p<0.05$. (D) Time spent in interaction zone male mice, n=7 animals/group, student t-test, ns (non-significant). Error bars indicate the SEM.

5.4. Prenatal exposure to 0.2ppm MeHg alters cognitive rigidity

MWM is a behavioural task typically used to assess learning and spatial memory. It is based on the principle that mice are highly motivated to escape from the water. Following 4 days of acquisition training to a submerged platform in a pool of water (Figure 5.7A-B), the memory probe was performed on day 11 after removing the platform from the pool. Both the control and MeHg-treated mice showed no difference in time spent in the target quadrant (Figure 5.7C-D), and a similar overall specificity of memory (Figure 5.7C, E-F). I then used reversal learning in MWM to examine cognitive flexibility. In reversal learning, the platform was moved from the initial target location (old target) to the opposite quadrant (new target). Acquisition to the novel location was performed over 2 days of training with latency to reach the platform as a measurement of learning (Figure 5.7G-H). The reversal probe was performed to measure cognitive flexibility on day 14. Here, the control mice showed a significant preference towards the new target location over the old target location, while the MeHg-treated mice failed to show significant quadrant preference in the new target zone (Figure 5.7I-J, K-L). Although there was no significant difference in % of time spent in a new target quadrant if I directly compared the control group with the MeHg group, the precision of the new memory, particularly in the new target quadrant, was impaired in the MeHg-treated group, which reflects spatial cognitive inflexibility (Figure 5.7K-L). Overall, these results indicate that prenatal 0.2ppm MeHg exposure impairs communication, increases restrictive and repetitive behaviours, and decreases sociability for the grown-up off-springs. This is the first time low-dose MeHg has been correlated to ASD-like behaviours in mice.

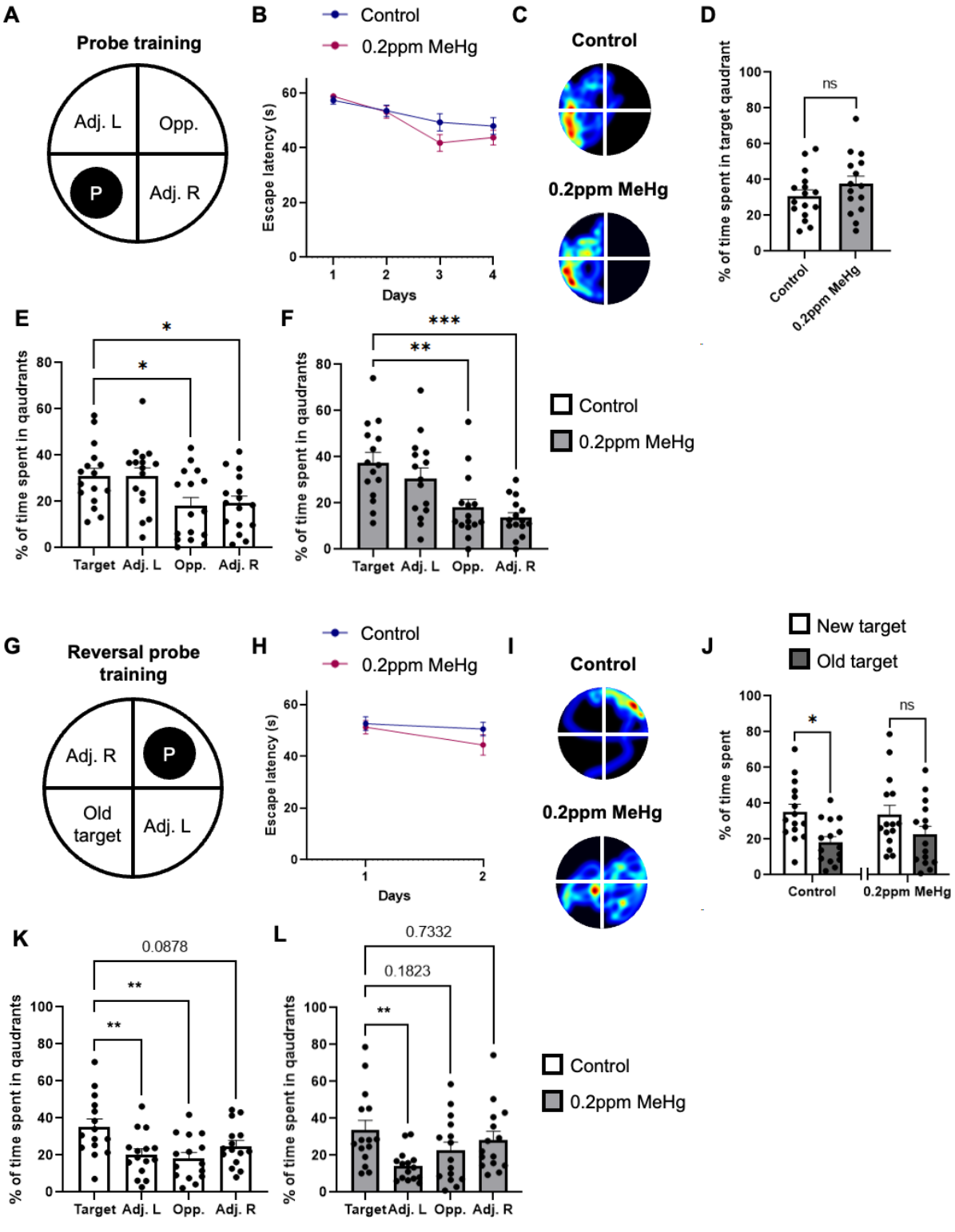
A
Probe training
Adj. L
Opp.
P
Adj. R
B
Control
0.2ppm MeHg
Escape latency (s)
Days
C
Control
0.2ppm MeHg
D
% of time spent in target qaudrant
ns
Control
0.2ppm MeHg
E
% of time spent in qaudrants
Target
Adj. L
Opp.
Adj. R
F
% of time spent in qaudrants
Control
0.2ppm MeHg
G
Reversal probe training
Adj. R
P
Old target
Adj. L
H
Control
0.2ppm MeHg
Escape latency (s)
Days
I
Control
0.2ppm MeHg
J
New target
Old target
% of time spent
ns
Control
0.2ppm MeHg
K
0.0878
% of time spent in qaudrants
Target
Adj. L
Opp.
Adj. R
L
0.7332
0.1823
% of time spent in qaudrants
Control
0.2ppm MeHg

Figure 5.7. Prenatal treatment with 0.2ppm MeHg alters cognitive rigidity.
(A-B) Acquisition of the initial platform location in the MWM task was performed across 4 days of training with latency to reach the platform as a measurement of learning. n=15-16 animals/group. (C-F) After the acquisition, the platform was removed on day 11, and mice were given a 60 s probe trial. (C) Representative heat maps from each group are shown in L. (D) The percentage of time spent in the target quadrant between control and 0.2ppm MeHg was analyzed as a measurement of memory. n=15-16 animals/group, student t-test, ns (non-significant). (E) The percentage of time spent in the 4 quadrant zones for control mice was analyzed on day 11 as a measurement of memory. n=16 animals/group, one-way ANOVA with post hoc test, *$p<0.05$. (F) The percentage of time spent in the 4 quadrant zones for MeHg-treated mice was analyzed on day 11 as a measurement of memory. n=15 animals/group, one-way ANOVA with post hoc test, **$p<0.01$, ***$p<0.001$. (G-H) Following the probe, the platform was moved to the opposite quadrant. Acquisition of the new platform location in the MWM task was performed across 2 days of training with latency to reach the platform as a measurement of learning. n=15 animals/group. (I-L) After the acquisition, the platform was removed on day 14, and mice were given a 60 s probe trial. (I) Representative heat maps from each group are shown in P. (J) The percentage of time spent in the new target quadrant and old target quadrant was analyzed as a measurement of reversal memory. n=15 animals/group, student t-test, * $p<0.05$, ns (non-significant). (K) The percentage of time spent in the 4 quadrant zones for control mice was analyzed on day 14 as a measurement of reversal learning. n=15 animals/group, one-way ANOVA with post hoc test, **$p<0.01$. (L) The percentage of time spent in the 4 quadrant zones for MeHg-treated mice was analyzed on day 14 as a measurement of reversal learning. n=15 animals/group, one-way ANOVA with post hoc test, **$p<0.01$. Error bars indicate the SEM.

5.5. Prenatal treatment with 0.2ppm MeHg does not alter the learning and memory of adult mice

As mentioned previously, mice showed normal learning and memory during the initial MWM probe day (Figure 5.7E-F). In addition to this test, I performed two additional learning and memory tests. The first is the Novel Object Recognition (NOR) test. Here, mice were habituated to a group of objects on day 1. On day 2 one of the objects is replaced with a novel object (Figure 5.8A). This test is based on the principle that mice have an innate preference for novelty, and as a result, the mice should interact more with the novel object than the familiar object. Control and MeHg-treated mice showed no difference in preference to the novel object which demonstrates that they have normal learning and memory (Figure 5.8B). The second test used was Fear Conditioning (FC) test. This test measures learning and associative memory by quantifying freezing time in response to a sudden fearful foot shock. FC utilizes classical conditioning where a neutral conditioned stimulus (an auditory tone) is paired with an aversive unconditioned stimulus (an electric foot shock). This will result in contextual and cued-dependent fear. Here I showed that the MeHg-treated mice experienced decreased freezing time prior to the initial shock/tone pairing during training (Figure 5.8C-D) and during the contextual fear (Figure 5.8C, E). However, they showed no changes in associative memory during the cued-dependent fear (Figure 5.8C, F). A study using an ASD mouse model also showed decreased freezing during the contextual fear triggers. This is most likely explained by a hyperactivity phenotype, which causes an inability to maintain freezing [312]. To determine what caused decreased freezing at baseline in the MeHg-treated mice I analyzed 1) movement and 2) grooming behaviour. First, I saw no changes in distance travelled (Figure 5.5A) or velocity (Figure 5.5B) between control and MeHg-treated mice during the open-field test. Second, I

assessed grooming behaviour under the assumption that increased grooming events would lead to a decrease in freezing activity with no changes in locomotion. Throughout a 10 min observation period, I observed no changes in time spent grooming (Figure 5.8G) and no changes in the number of grooming events (Figure 5.8H).

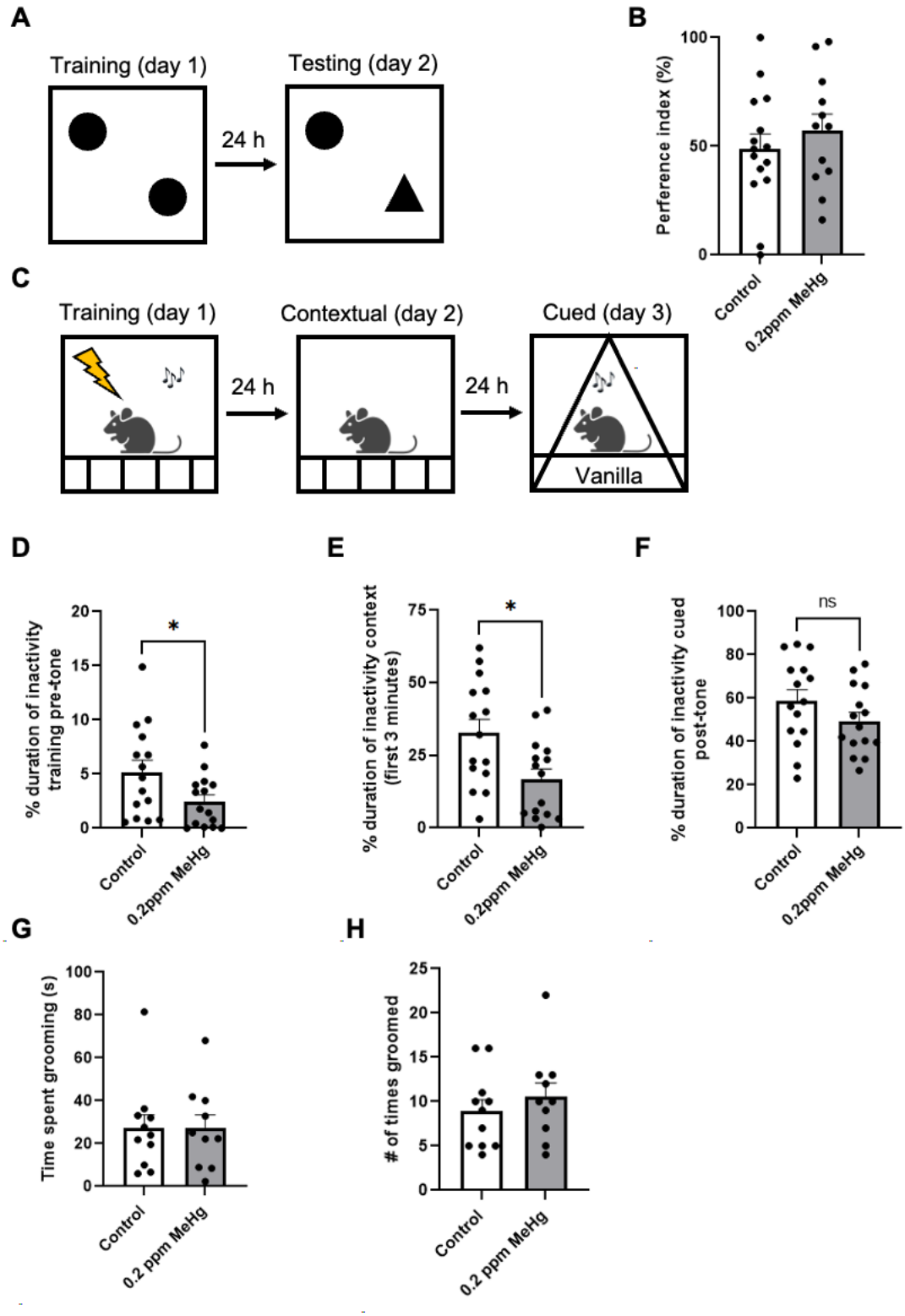
A
Training (day 1)
Testing (day 2)
24 h
B
Perference index (%)
100
50
0
Control
0.2ppm MeHg
C
Training (day 1)
Contextual (day 2)
Cued (day 3)
24 h
24 h
Vanilla
D
% duration of inactivity training pre-tone
20
15
10
5
0
*
Control
0.2ppm MeHg
E
% duration of inactivity context (first 3 minutes)
75
50
25
0
*
Control
0.2ppm MeHg
F
% duration of inactivity cued post-tone
100
80
60
40
20
0
ns
Control
0.2ppm MeHg
G
Time spent grooming (s)
100
80
60
40
20
0
Control
0.2 ppm MeHg
H
# of times groomed
25
20
15
10
5
0
Control
0.2 ppm MeHg

Figure 5.8. Prenatal treatment with 0.2ppm MeHg does not alter the learning and memory of adult mice.
(A) The NOR test evaluated the differences in the exploration of novel object and familiar object (B) The preference index is calculated by dividing the time spent with the novel object divided by the total time spent with both the novel and familiar object multiplied by 100. (C) On day 1 (training) of the FC test both control and MeHg-treated mice were exposed to a tone 3 times which was immediately followed by a shock (0.4 mA, 2 seconds). (D) The percentage of time spent freezing prior to the initial tone/shock was measured (baseline). n=15 animals/group, student t-test, *$p<0.05$. (C) On day 2 (contextual) of the FC test the mice were exposed to the same environment, (E) the percentage of time spent freezing within the first three minutes in the conditioning context without shock or tone was measured. n=15 animals/group, student t-test, *$p<0.05$. (C) On day 3 (cued) of the FC test the environment was altered to a triangle shape and white noise, red lighting, and vanilla scent was added. (F) The percentage of time spent freezing after the first tone was measured. n=15 animals/group. (G) Time spent grooming, and (H) number of grooming events recorded over 10 min. Error bars indicate the SEM.

5.6. Prenatal exposure to 0.2ppm MeHg does not alter the cerebral cortical neurons distributions in adult mice

Following behavioural testing, the experimental mice were sacrificed and immunohistochemical analysis was performed in all six layers of the cerebral cortex (Figure 5.9A). I examined the number of $Tbr1^+$ and $Ctip2^+$ deep-layer cortical neurons and the number of $Cux1^+$ and $Satb2^+$ upper-layer cortical neurons. I found that prenatal low-dose MeHg did not alter the number and distribution of $Satb2^+$ (Figure 5.9B-C), $Tbr1^+$ (Figure 5.9B, D), $Cux1^+$ (Figure 5.9E-F), or $Ctip2^+$ cells (Figure 5.9E, G) in any layer of the adult cerebral cortex.

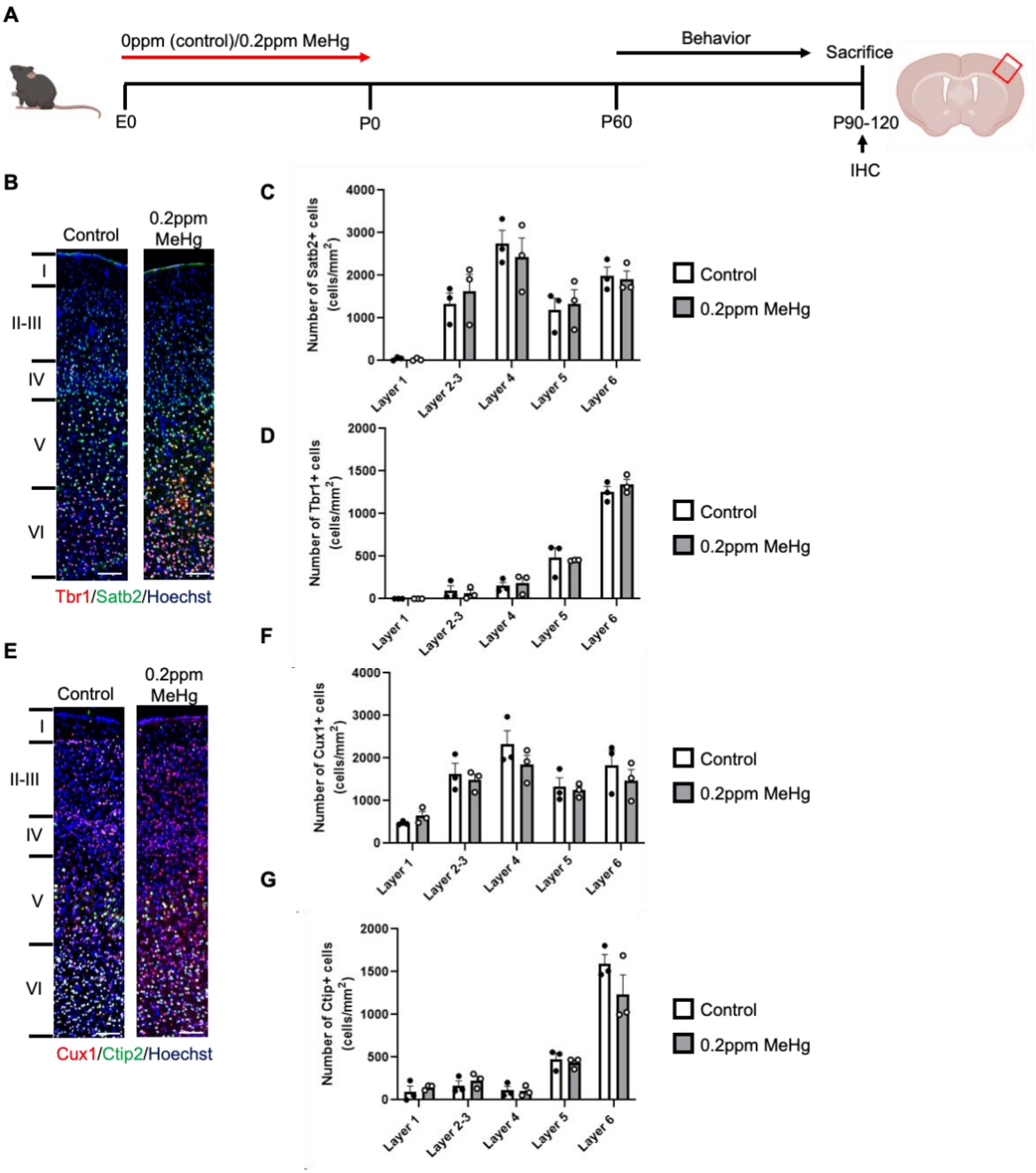
A
0ppm (control)/0.2ppm MeHg
Behavior
Sacrifice
E0
P0
P60
P90-120
IHC
B
Control
0.2ppm MeHg
I
II-III
IV
V
VI
Tbr1/Satb2/Hoechst
C
Number of Satb2+ cells (cells/mm2)
4000
3000
2000
1000
0
Layer 1
Layer 2-3
Layer 4
Layer 5
Layer 6
Control
0.2ppm MeHg
D
Number of Tbr1+ cells (cells/mm2)
2000
1500
1000
500
0
Layer 1
Layer 2-3
Layer 4
Layer 5
Layer 6
Control
0.2ppm MeHg
E
Control
0.2ppm MeHg
I
II-III
IV
V
VI
Cux1/Ctip2/Hoechst
F
Number of Cux1+ cells (cells/mm2)
4000
3000
2000
1000
0
Layer 1
Layer 2-3
Layer 4
Layer 5
Layer 6
Control
0.2ppm MeHg
G
Number of Ctip+ cells (cells/mm2)
2000
1500
1000
500
0
Layer 1
Layer 2-3
Layer 4
Layer 5
Layer 6
Control
0.2ppm MeHg

Figure 5.9. Prenatal treatment with 0.2ppm MeHg does not alter the cerebral cortices of adult mice.
(A) Schematic of prenatal exposure to MeHg in pregnant mice, created with BioRender.com. 0ppm (control) and 0.2ppm MeHg were administered through drinking water to pregnant mice starting at E0 until P0. Following behaviour testing brains were collected for immunohistochemistry. (B, D-F) Images of cerebral cortex sections from mice receiving 0ppm and 0.2ppm MeHg treatment, immunostained for Tbr1 (B, red), Satb2 (B, green), Cux1 (E, red) and Mcm2 (E, green) and counterstained for Hoechst (blue). Scale bar: 25 µm. (C-D, F-G) Quantitative analysis of the number and proportion of (C) $Satb2^{+}$, (D) $Tbr1^{+}$, (F) $Cux1^{+}$, and (G) Ctip2, determined from sections similar to those shown in (B, E). n=3 animals/group. Error bars indicate the SEM.

5.7. Prenatal exposure to 0.2ppm MeHg does not alter adult neurogenesis in the SVZ

To assess for changes in neurogenesis, I examined the two neurogenic niches within the rodent brain, which are 1) the SVZ and 2) the subgranular zone (SGZ) of the hippocampus. In the SVZ, newborn neuroblasts migrate via the rostral migratory stream to the olfactory bulb. Here, they are integrated into existing neural circuitry that is critical for smelling [313]. In humans, olfaction is rudimentary, and the existence of an adult rostral migratory stream has been controversial [314,315]. However, neuroblasts are present in the SVZ of adult humans. This has led researchers to speculate on other possible migratory destinations. In the striatum, researchers have found high levels of DCX comparable to that of the hippocampus (another key area of adult neurogenesis) [316]. This suggests that the newborn neurons in the striatum may be a result of SVZ neurogenesis; however, more research is required. Changes in neuron production or proliferation have been observed in multiple models of ASD in the SVZ. A PTEN deletion-ASD mouse model showed a reduced number of DCX^+ neuroblasts in the SVZ [317]. Furthermore, NSCs derived from the SVZ of *Shank3*-KO mice had a decreased number of $Ki67^+$ proliferating cells [318].

To examine changes in the SVZ, experimental mice after undergoing behavioural testing were sacrificed and immunohistochemical analysis was performed in the SVZ near the lateral ventricles. The SVZ was divided into three areas for quantification, the dorsal, lateral, and ventral SVZ (Figure 5.10A). I examined the number of DCX^+ neuroblasts and $Mcm2^+$ proliferating cells. I found that prenatal low-dose MeHg did not alter the number or distribution of DCX^+ (Figure 5.10B-C) or $Mcm2^+$ cells (Figure 5.10D-G) in any of the three regions of the SVZ.

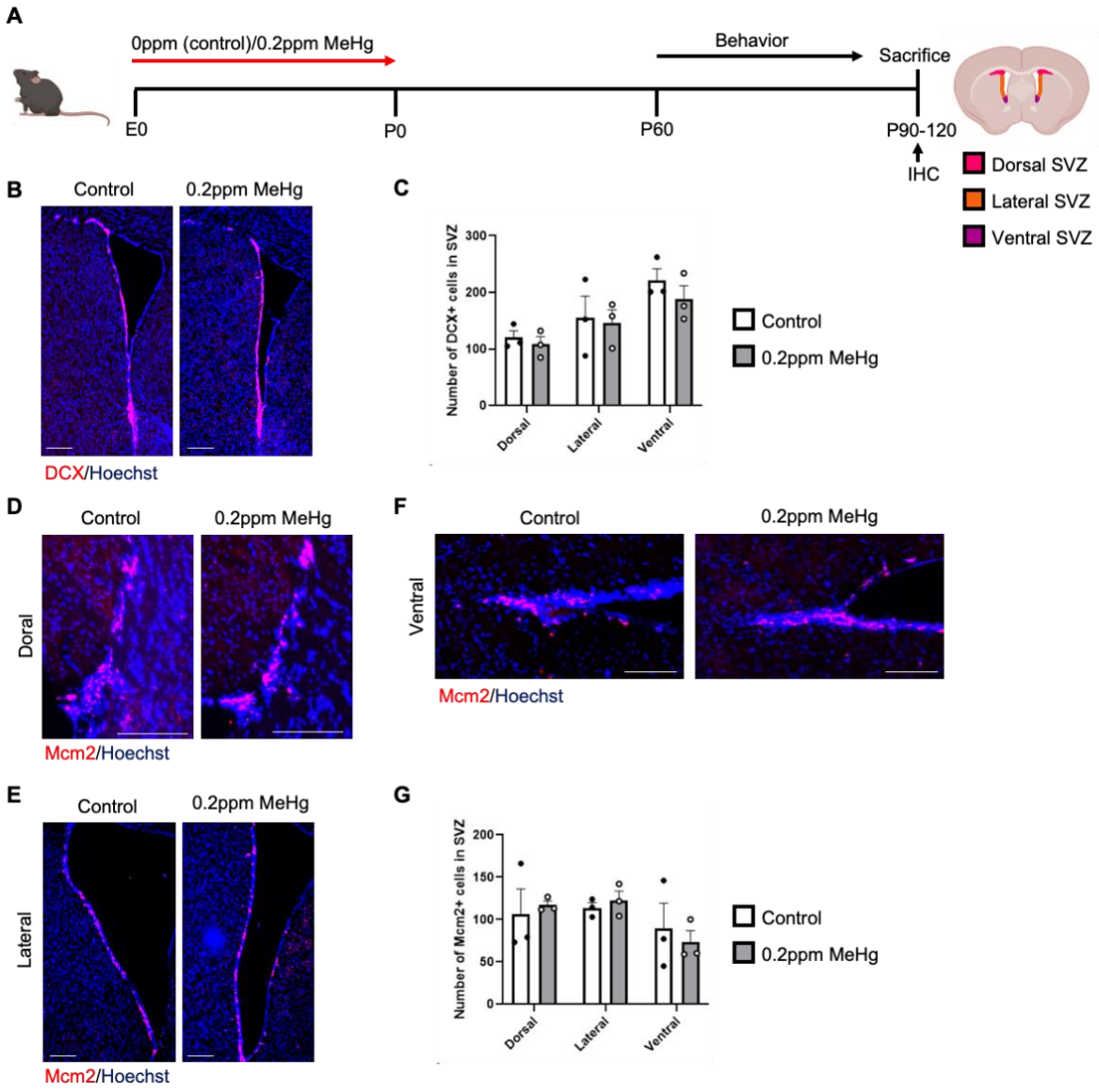

Figure 5.10. Prenatal treatment with 0.2ppm MeHg does not alter adult neurogenesis in the SVZ.

(A) Schematic of prenatal exposure to MeHg in pregnant mice, created with BioRender.com. 0ppm (control) and 0.2ppm MeHg were administered through drinking water to pregnant mice starting at E0 until P0. Following behaviour testing brains were collected for immunohistochemistry. (B, D-F) Images of SVZ sections from mice receiving 0ppm and 0.2ppm MeHg treatment, immunostained for DCX (B, red), and Mcm2 (D-F, red) and counterstained for Hoechst (blue). Scale bar: 100 µm. (C, G) Quantitative analysis of the number and proportion of (C) DCX^+ neuroblasts and (G) $Mcm2^+$ proliferative cells within SGZ, determined from sections similar to those shown in (B, D-F). n=3 animals/group. Error bars indicate the SEM.

5.8. Prenatal exposure to 0.2ppm MeHg does not alter adult neurogenesis in the SGZ

The SGZ of the dentate gyrus (DG) is another primary contributor to adult neurogenesis. Here, RGPs in the SGZ mature into IPs and neuroblasts. Progenitors then migrate into the granule cell layer and extend their dendrites into the molecular layer to receive inputs from the entorhinal cortex and terminate in the CA3 of the hippocampus [313]. This process has been characterized in both rodents [319,320] and humans [321–323]. Changes in neuron production or proliferation have been observed in multiple models of ASD in the SGZ. In a BTBR-ASD mouse model, researchers observed a decreased number of $BrdU^+$ proliferating cells and decreased number of DCX^+ neuroblasts [324]. In contrast to this, another study using a PTEN deletion-ASD mouse model observed increased $Ki67^+$ proliferating cells in the SGZ [325].

To examine changes in the SGZ, experimental mice after undergoing behavioural testing were sacrificed and immunohistochemical analysis was performed in the SGZ (Figure 5.11A). I examined the number of DCX^+ neuroblasts and $Mcm2^+$ proliferating cells. I found that prenatal low-dose MeHg did not alter the number or distribution of DCX^+ (Figure 5.11B-C) or $Mcm2^+$ cells (Figure 5.11D-E) in the SGZ.

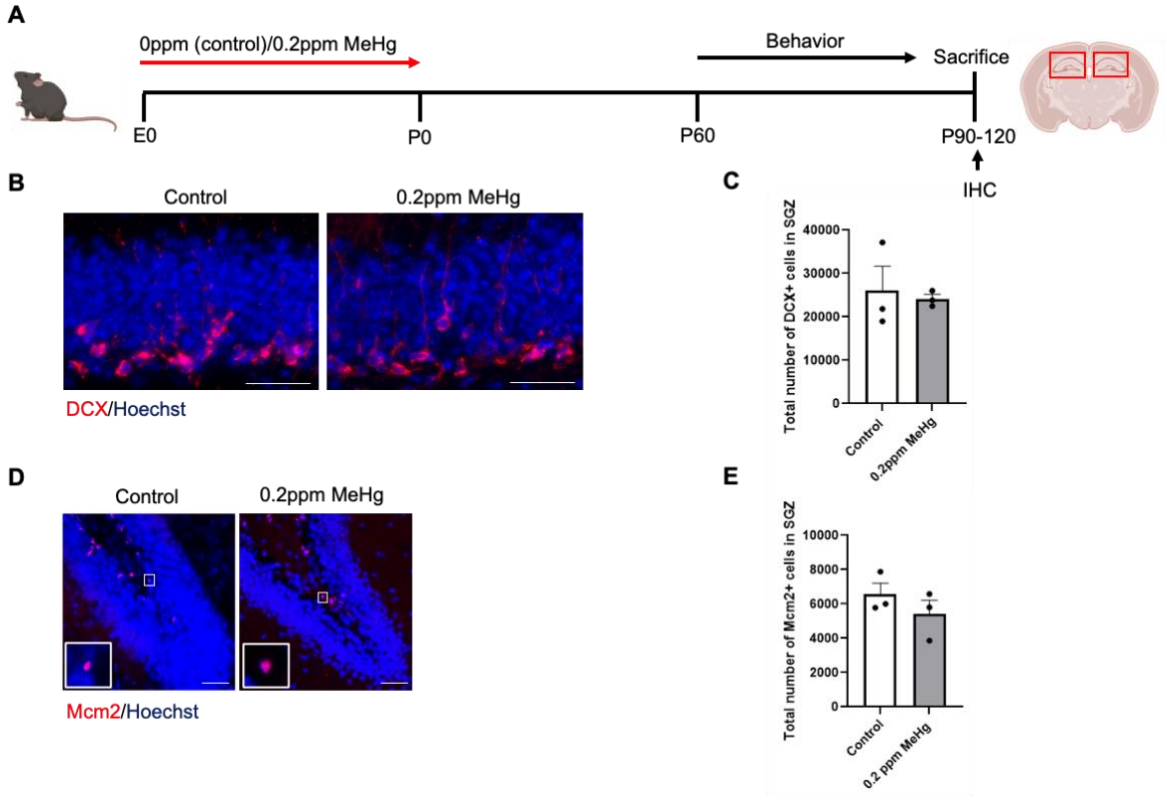

Figure 5.11. Prenatal treatment with 0.2ppm MeHg does not alter adult neurogenesis in the SGZ.

(A) Schematic of prenatal exposure to MeHg in pregnant mice, created with BioRender.com. 0ppm (control) and 0.2ppm MeHg were administered through drinking water to pregnant mice starting at E0 until P0. Following behaviour testing brains were collected for immunohistochemistry. (B, D) Images of hippocampal sections from mice receiving 0ppm and 0.2ppm MeHg treatment, immunostained for DCX (B, red), and Mcm2 (D, red) and counterstained for Hoechst (blue). Scale bar: 30 µm. (C, E) Quantitative analysis of the number and proportion of (C) DCX^+ neuroblasts and (E) $Mcm2^+$ proliferative cells within SGZ, determined from sections similar to those shown in (B, D). n=3 animals/group. Error bars indicate the SEM.

5.9. Hg analysis

To examine Hg accumulation in mice, I analyzed the feces, urine, and blood of all the mice undergoing behavioural testing at P22, P42, and at sacrifice (Figure 5.12A-D). I found that the highest concentration of Hg was detected in the feces at P22 (Figure 5.12B), which is consistent with the known route of MeHg excretion [7]. Following behavioural testing, the mice were sacrificed, and major Hg target organs were assessed. Hg was detected in the liver and kidneys of MeHg-treated mice (Figure 5.12A, E-F). In the liver, MeHg was roughly 6 times more concentrated than in control mice, and in the kidneys, MeHg was roughly 3 times more concentrated than in control mice (Figure 5.12E). To determine the distribution of Hg in the brain following prenatal exposure, various brain regions were isolated for Hg analysis. I found that very little Hg was present in the adult brain of the prenatally exposed mice (Figure 5.12F), suggesting that the behavioural deficits observed in early adulthood are residual effects of aberrant embryonic neurodevelopment that is elicited by prenatal MeHg exposure.

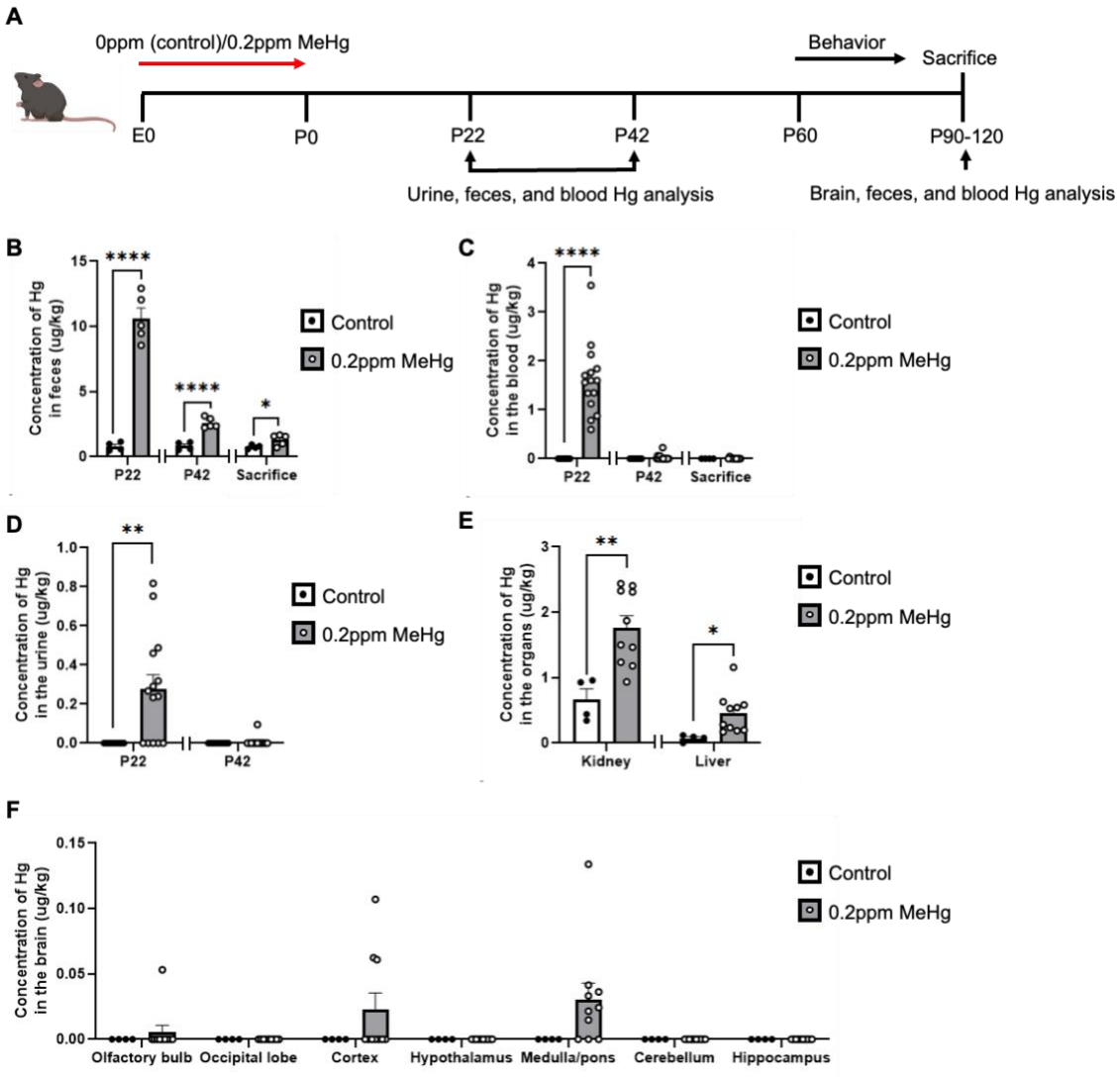

Figure 5.12. Hg analysis.
(A) Schematic of prenatal exposure of MeHg to pregnant mice, created with BioRender.com. Pregnant mice were exposed to either control (0ppm MeHg) or 0.2ppm MeHg. Treatment was administered through drinking water to pregnant mice starting at E0 until P0. Feces and blood were collected at P22, P42, and sacrificed for Hg analysis. Urine was collected at P22 and P42 for Hg analysis. Once behavioural testing was complete the brain, liver, and kidneys were dissected at sacrifice (P90-120) for Hg analysis. (B) Quantitative analysis of Hg concentration in the feces collected at P22, P42, and sacrifice. n=4-5 cages/group, student t-test, *p<0.05, ****p<0.0001. (C) Quantitative analysis of Hg concentration in the blood collected at P22, P42, and sacrifice. n=4-15 animals/group, student t-test, ****p<0.0001. (D) Quantitative analysis of Hg concentration in the urine collected at P22 and P42. n=9-15 animals/group, student t-test, **p<0.01. (E) Quantitative analysis of Hg concentration in the kidneys and liver collected at sacrifice. n=4-7 animals/group, student t-test, *p<0.05, **p<0.01. (F) Quantitative analysis of Hg concentration in various brain regions collected at sacrifice. n=4-7 animals/group. Error bars indicate the SEM.

Chapter 6: Discussion and conclusion

Overall, I put forward three major conclusions. First, I discovered an underlying cellular and molecular mechanisms that contribute to MeHg-induced premature neuronal differentiation. Second, I demonstrated that metformin, an FDA-approved drug, treatment can eliminate the MeHg-induced premature neuronal differentiation of cortical precursors both in culture and *in vivo*. Finally, prenatal low-dose MeHg exposure triggers ASD-like behaviours, including impaired communication, reduced sociability, and increased restrictive and repetitive behaviours in young adult mice.

6.1. Asymmetric division is a potential cellular mechanism underlying MeHg-induced premature neuronal differentiation

Embryonic RGPs are known to perform asymmetric division to produce intermediate progenitor/cortical neurons or symmetric division to expand the cortical precursor cell pool [326]. I used a scRNA-seq dataset from E13.5 cortices to identify a cluster of transitional cells. Feature gene analysis showed that the population of transitional cells do not highly express any cluster-specific marker genes. However, further subcluster analysis showed that this cluster of transitional cells contains 4 subpopulations of cells representing proliferating radial glial cells, immature neurons, layer I neurons, and pericytes (Figure 3.4A-D). Here, I demonstrated that these transitional cells are comprised of RGPs undergoing asymmetrical division to directly generate cortical neurons (Figure 3.6A-H). This provides evidence at the single-cell level that embryonic RGPs can take two trajectories during cortical development, either symmetric division to expand the cortical precursor pool that ultimately produces the sequential generation of IPs, immature neurons, and mature neurons or asymmetric division to directly generate cortical neurons through the transitional cell population. This phenomenon was also exhibited in human neocortical development in mid-gestation, disclosed by scRNA-seq data [327]. Importantly,

I found that fetal MeHg exposure can alter RGP trajectory to be prone to a transitional cell state (Figure 3.7A-F). This accelerates the differentiation process by increasing the asymmetrical division of cortical precursors to directly generate cortical neurons. This process was further confirmed by immunohistochemical analysis conducted by Dr. Joseph Leung, who showed that prenatal MeHg exposure significantly increased the number of DCX^+ neuroblasts, specifically in the VZ, at the expense of proliferating $Pax6^+$ cortical precursors (Appendix Figure 1A-F). Furthermore, Dr. Joseph Leung showed that at P7, the number of $Tbr1^+$ cortical neurons was significantly increased following prenatal MeHg treatment (Appendix Figure 2A-D). Together, these results support that prenatal MeHg enhances asymmetric division of RGPs in embryo to promote the genesis of newborn neurons in the VZ, which subsequently increase the number of deep-layer $Tbr1^+$ cortical neurons at early postnatal (Figure 6.1). However, enhanced asymmetric division facilitated by MeHg must be further validated using other metrics to confirm this.

In addition, I showed that direct CREB-targeted genes, *Jund* and *Fos,* were specifically upregulated in the RGP1 cell cluster but not in other neural cell clusters following prenatal MeHg exposure using the scRNA-seq data analysis (Figure 3.9A-C). I further confirmed that the downstream CREB target genes expression was upregulated, although not significantly, in cultured embryonic cortical precursors exposed to low-dose MeHg (Figure 4.3A-D). I also demonstrated that prenatal MeHg exposure significantly increased pS133-CREB levels, an activated form of CREB, in cultured embryonic cortical precursors (Figure 4.2A-D). These results suggest that MeHg-induced CREB activation in RGP1 may initiate the process that alters their trajectory towards the transitional cell population to directly generate cortical neurons.

Overall, I identified a potential cellular mechanism which mediates premature neural differentiation caused by low-dose MeHg exposure. These findings are the first to show asymmetric division in the embryonic mouse cerebral cortex via scRNA-seq. In addition, low-dose prenatal MeHg exposure alters RGP1 trajectory towards asymmetric division to directly generate immature/mature neurons. Finally, downstream CREB-target genes, *Jund* and *Fos,* are differentially expressed in the RGP1 population only, suggesting that CREB may play an important role in MeHg-induced differentiation.

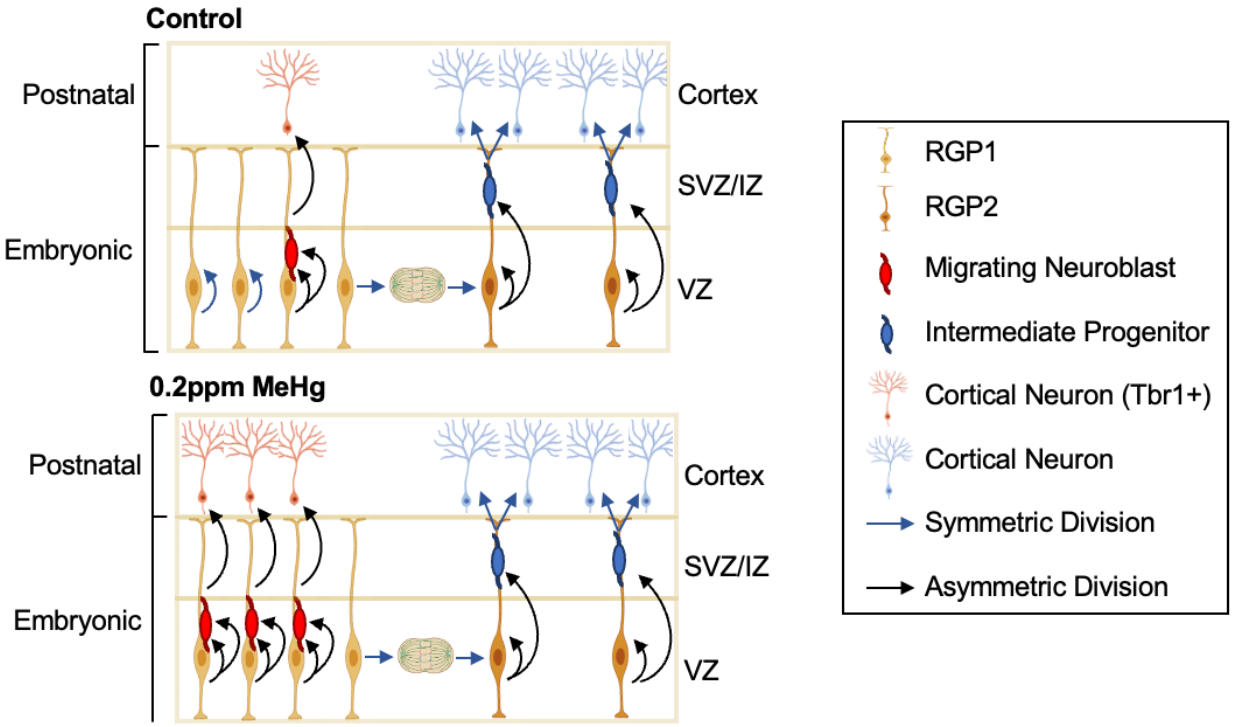

Figure 6.1. Proposed model of premature neuronal differentiation in the cerebral cortex. Created with BioRender.com.

6.2. CREB activity/CREB-CBP interaction is an essential molecular mechanism to drive low-dose MeHg-induced premature neuronal differentiation

Consistent with previous work conducted on non-apoptotic MeHg concentrations in a neuroblastoma cell line [105], I found that pS133-CREB was elevated following 250nM MeHg exposure. To further explore this pathway, I probed for changes in pT410/403-aPKC, a known upstream kinase of pS436-CBP. Western blotting revealed that non-apoptotic MeHg caused a significant reduction in pT410/403-aPKC (Figure 4.2A-G). As previously reported, early work from our lab has demonstrated that metformin can act on the AMPK-aPKC-CBP pathway to phosphorylate CBP at S436 site in order to promote neuronal differentiation of neural precursor cells [280]. Additionally, both p-S133 CREB and p-S436 CBP are repulsive to each other [288,291]. Since 250nM MeHg promoted p-S133 CREB activation while reducing the aPKC-CBP pathway in cultured cortical precursors, I hypothesized that co-treatment with both metformin and MeHg could rescue premature neuronal differentiation and the reduced proliferative RGP population caused by MeHg alone, by initiating repulsion between pS133-CREB and pS436-CBP. This was demonstrated both in culture (Figure 4.4A-C, Figure 4.5A-G) and *in vivo* (Figure 4.6A-J). These findings confirm that 1) pS133-CREB promotes premature neuronal differentiation in culture (Figure 6.2A), and 2) this can be rescued by metformin through initiating repulsion between pS133-CREB and pS436-CBP (Figure 6.2B-C).

Following Dr. Joseph Leung's discovery that 0.2ppm MeHg resulted in increased thickness of the CP (Appendix Figure 1I), I demonstrated that the increased thickness of the CP can be rescued by co-treatment with metformin (Figure 4.7A-C). These results suggest that the increased cortical thickness was caused by MeHg-induced premature neuronal differentiation. Finally, there was no change in the amount of Hg measured in the embryonic brain at E15

(Figure 4.8A-C). These results support that metformin treatment via drinking water does not affect Hg consumption and accumulation in fetal brains, but directly impacts the pathophysiology of MeHg.

Overall, I conducted a series of experiments to understand the role of pS133-driven CREB activity in modulating MeHg-induced premature differentiation, and I have identified a potential therapeutic strategy to prevent the developmental defects using an FDA-approved anti-diabetic drug, metformin.

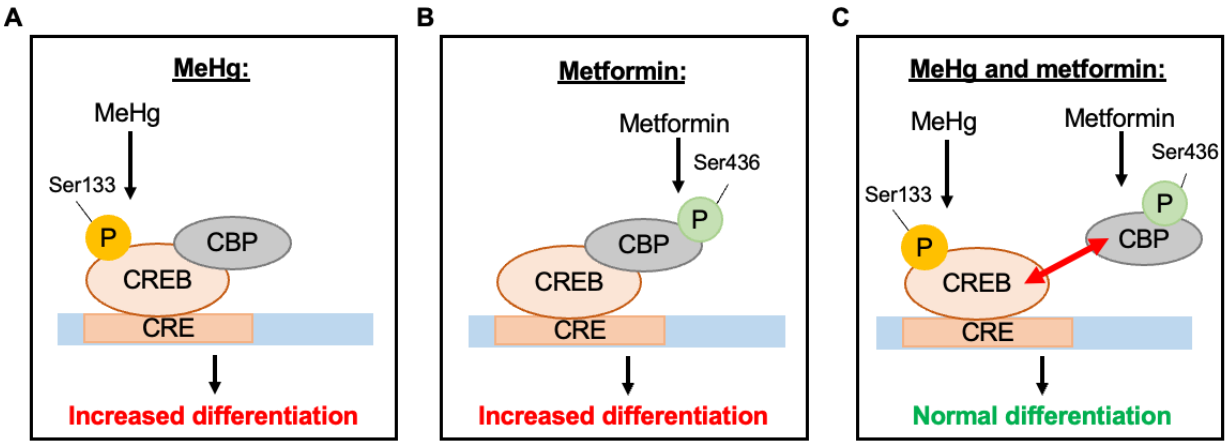

Figure 6.2. Proposed model for MeHg and MeHg+metformin exposure.
(A-C) Proposed model for MeHg and MeHg+metformin exposure. (A) MeHg alone increases pS133-CREB and represses pS436-CBP, which results in increased neuronal differentiation. (B) Metformin alone promotes pS436-CBP, which causes increased neuronal differentiation shown in a previous publication [281]. (C) Co-treatment with MeHg and metformin causes repulsion between pS133-CREB and pS436-CBP, alleviating MeHg-induced neuronal differentiation.

6.3. Low-dose prenatal MeHg exposure in rodents promotes ASD-like behaviours in early adulthood

This study is the first to show that prenatal low-dose MeHg exposure triggers ASD-like behaviours in a rodent model. Individuals with ASD experience deficits in verbal language. To test this in a rodent model, I performed USV analysis at early postnatal. Mouse pups emit calls during their first two weeks of life when separated from their mother and littermates [328]. I found that mice prenatally exposed to low-dose MeHg vocalized significantly less at P9 than control mice (Figure 5.3A-D). This is consistent with other genetic mouse models of ASD [329–331]. Moreover, children with ASD typically perform repetitive behaviours such as tapping, hand flapping, and rocking [145]. To test this in mice, I performed the Marble Burying test and found that mice prenatally treated with low-dose MeHg buried significantly more marbles than control mice (Figure 5.4A-B). Another key component of ASD is poor sociability, which I also observed in MeHg-treated mice using the ASI test (Figure 5.6A-D). The third common characteristic in individuals with ASD is rigidity in routine and interests. To test this, I used the MWM test. This behavioural task is typically used to assess learning and spatial memory; however, I utilized the reversal learning/memory component of MWM to specifically examine cognitive rigidity. Here, cognitive rigidity was measured by the inability to alter target zone preference which has been shown in other ASD mouse models [332]. I found that mice prenatally treated with low-dose MeHg showed poor reversal memory (Figure 5.7A-L). Overall, I have demonstrated the three key components of ASD with MeHg-treated mice. Interestingly, recent studies have shown that high-dose MeHg in adulthood exasperates the effects of a genetic ASD mouse model [259,260]. Our study provides further evidence for the potential link between ASD and MeHg.

In addition, I aimed to examine changes in the adult brain following prenatal MeHg exposure. Despite changes in rodent behaviour, immunohistochemical analysis revealed no changes in the number or distributions of deep or superficial layer-specific cortical neurons (Figure 5.9A-G). Rodent models of ASD have shown impaired cortical neuron production and migration, which were assessed in the somatosensory cortex, a key region for sensory processing [204,210,211,213]. In addition, neuron overproduction has been observed in human ASD patients [194,195] and rodent models of ASD [204,205]. However, I do not see changes in the number of cortical neurons during adulthood, except for transient alterations observed by Dr. Joseph Leung during the early postnatal age (Appendix Figure 2A-D). Interestingly, E/I imbalance and overgeneration or under-pruning of synaptic connections have also been linked to ASD pathogenesis [215–217,333,334]. E/I balance is regulated by glutamatergic and GABAergic neurons and is implicated in ASD pathogenesis. As previously highlighted, increased glutamatergic signalling [215–217] and reduced GABAergic signalling have been observed in ASD patients [215,217]. In addition, synaptic formation and function are key underlying mechanisms associated with ASD and can further contribute to E/I imbalance [333,334]. This suggests that there may be changes in E/I balance or changes in synaptic formation and function that I have not characterized in our prenatally-treated adult mice, which could underly the observed ASD-like behaviours.

One possible outcome for increased neuronal differentiation during embryonic brain development is a reduced pool of neural stem cells in adulthood and decreased adult neurogenesis. To examine whether MeHg-induced premature neuronal differentiation can lead to these phenotypes, I examined adult neurogenesis in the two neurogenic niches: 1) the SVZ of the lateral ventricle and 2) the SGZ of the hippocampus following prenatal MeHg exposure. I did not observe any changes in the number of proliferating cells and immature neuroblasts in these two

adult neurogenic niches (Figure 5.10A-G, Figure 5.11A-E). Associated with this, I did not observe any changes in learning and memory behaviours (Figure 5.7A-L, Figure 5.8A-F), which are known to be regulated by adult hippocampal neurogenesis [335]. It is possible that the reduced adult neurogenesis and its associated behaviour following prenatal MeHg exposure would occur in aging mice where compensatory mechanisms may die out.

These findings highlight three major conclusions. First, prenatal exposure to low-dose MeHg promotes behavioural hallmarks of ASD, including restrictive and repetitive behaviours and deficits the communication and social interaction. Second, since very little Hg remained in the brains of mice by adulthood, the behavioural deficits observed in early adulthood are residual effects of aberrant embryonic neurodevelopment. Third, prenatal exposure to low-dose MeHg does not cause changes in deep or superficial layers of the cerebral cortex and the number of neuroblasts or proliferation cells in the hippocampal SGZ or lateral ventricle SVZ.

6.4. Future directions

This project has three major future directions. First, I have elucidated the underlying mechanism that causes MeHg-induced premature neuronal differentiation in embryo. Here, I showed that prenatal MeHg exposure causes asymmetric neuronal differentiation of cortical precursors to directly generate cortical neurons through CREB activation. However, what triggers CREB phosphorylation following MeHg exposure is still unknown. My scRNA-seq dataset obtained from the cortices of embryonic mice revealed that *Glyoxalase 1* (*Glo1*) is reduced in MeHg-treated embryos relative to control. Interestingly, a recent study has shown that Glo1 inhibition can lead to increased CREB phosphorylation and subsequent neurogenesis-related pathways [336]. Moreover, Glo1 knock-out embryos showed similar phenotypes as MeHg-treated embryos, including induced neuronal differentiation at the expense of the proliferation of

embryonic cortical precursor cells [337]. Overall, more work is needed to study the relationship between CREB and Glo1. Second, I have shown that low-dose exposure to 0.2ppm MeHg in embryo causes premature neuronal differentiation, which can be rescued by co-treatment with metformin. I also demonstrated that administration of 0.2ppm MeHg from conception until birth can result in the onset of ASD-like behaviours. However, the direct link between premature neuronal differentiation and ASD-like behaviours is still unknown. To study this, I must confirm that ASD-like behaviours caused by low-dose MeHg alone can also be rescued by co-treatment with metformin. Finally, the results of this study highlight a potential epidemiological research project to investigate the potential therapeutic effect of metformin-treated pregnant women exposed to Hg in relation to childhood neurodevelopmental outcomes.

6.5. Limitations

Overall, this study has two major limitations. First, results from rodent studies are inherently limited in extrapolating to the human condition. It remains unclear how low-dose MeHg affects human embryonic brain development. Future human brain organoid models could be implemented to study the impact of low-dose MeHg on human cerebral cortex development. Furthermore, ASD is difficult to interpret in a rodent model as deficits in social interaction and social communication can only be approximated in rodents.

Second, the most common way humans are exposed to MeHg is via fish consumption. Fish contain beneficial long-chain polyunsaturated omega-3 fatty acids and Se, both of which can have positive effects. Polyunsaturated omega-3 fatty acids are known to aid prenatal development [258], and polyunsaturated omega-3 fatty acids and Se are both known protective agents against Hg toxicity [11,13–16]. Therefore, this project demonstrates the effect of isolated MeHg but does not accurately mimic real-world exposure conditions.

6.6. Significance

The devastating effects of high-dose MeHg exposure were highlighted in the Minamata Bay Disaster [338]. However, the long-term consequences of low-dose MeHg exposure during pregnancy remains unclear, and the potential relationship between MeHg and ASD has been a contentious area of study. To my knowledge, this is the first study to demonstrate that prenatal low-dose MeHg exposure results in ASD-like behaviours in a rodent model. Overall, the results of this study have provided novel insight into the long-term effects of low-dose prenatal MeHg exposure, a potential cellular and molecular mechanism.

Globally, all populations are exposed to some amount of Hg, and seafood sampling has found widespread MeHg contamination in fish, shellfish, and marine mammals [339]. Communities that are highly dependent on fish consumption, such as arctic populations, are at an elevated risk for MeHg exposure. This is a very pertinent topic for Canadian health as women of childbearing age living in northern regions and Quebec tend to have high Hg levels that often exceed Health Canada's guidelines [340]. Furthermore, the dangers of MeHg are a growing concern despite the plateau in Hg emissions. A combination of climate change and overfishing has resulted in more MeHg entering aquatic organisms [341]. Moreover, melting permafrost in Artic environments where Hg^0 is known to accumulate will result in more MeHg in aquatic circulation [3]. Overall, MeHg is a topical concern, and further research is needed on the long-term effects of moderate fish consumption during pregnancy.

References

1. World Health Organization. Mercury and health. https://www.who.int/news-room/fact-sheets/detail/mercury-and-health (2017).
2. US EPA. Basic Information about Mercury | US EPA. https://www.epa.gov/mercury/basic-information-about-mercury.
3. Outridge, P. M., MacDonald, R. W., Wang, F., Stern, G. A. & Dastoor, A. P. A mass balance inventory of mercury in the Arctic Ocean. *Environmental Chemistry* **5**, 89–111 (2008).
4. Lamborg, C. *et al.* Mercury in the anthropocene ocean. *Oceanography* **27**, 76–87 (2014).
5. Lin, H. *et al.* Mercury methylation by metabolically versatile and cosmopolitan marine bacteria. *ISME J* **15**, 1810–1825 (2021).
6. Li, M. *et al.* Assessing sources of human methylmercury exposure using stable mercury isotopes. *Environ Sci Technol* **48**, 8800–8806 (2014).
7. National Research Council (US). Toxicological Effects of Methylmercury. *Toxicological Effects of Methylmercury* (2000) doi:10.17226/9899.
8. Leaner, J. J. & Mason, R. P. Methylmercury accumulation and fluxes across the intestine of channel catfish, Ictalurus punctatus. *Comparative Biochemistry and Physiology - C Toxicology and Pharmacology* **132**, 247–259 (2002).
9. Ouédraogo, O. & Amyot, M. Effects of various cooking methods and food components on bioaccessibility of mercury from fish. *Environ Res* **111**, 1064–1069 (2011).
10. Højbjerg, S., Nielsen, J. B. & Andersen, O. Effects of dietary lipids on whole-body retention and organ distribution of organic and inorganic mercury in mice. *Food Chem Toxicol* **30**, 703–708 (1992).

11. Jin, X. *et al.* Modulating effects of dietary fats on methylmercury toxicity and distribution in rats. *Toxicology* **230**, 22–44 (2007).

12. Cha, C. W. A study on the effect of garlic to the heavy metal poisoning of rat. *J Korean Med Sci* **2**, 213–223 (1987).

13. Seppänen, K. *et al.* Effect of supplementation with organic selenium on mercury status as measured by mercury in pubic hair. *J Trace Elem Med Biol* **14**, 84–87 (2000).

14. Stoewsand, G. S., Bache, C. A. & Lisk, D. J. Dietary selenium protection of methylmercury intoxication of Japanese quail. *Bull Environ Contam Toxicol* **11**, 152–156 (1974).

15. Farina, M. *et al.* Mechanisms of the inhibitory effects of selenium and mercury on the activity of δ-aminolevulinate dehydratase from mouse liver, kidney and brain. *Toxicol Lett* **139**, 55–65 (2003).

16. Azad, A. M. *et al.* Effects of geography and species variation on selenium and mercury molar ratios in Northeast Atlantic marine fish communities. *Science of The Total Environment* **652**, 1482–1496 (2019).

17. Kershaw MB, T. G., Dhahir, P. H. & Clarkson, T. W. The Relationship between Blood Levels and Dose of Methylmercury in Man. *Arch Environ Health* **35**, 28–36 (1980).

18. Bridle, T. G., Kumarathasan, P. & Gailer, J. Toxic Metal Species and 'Endogenous' Metalloproteins at the Blood–Organ Interface: Analytical and Bioinorganic Aspects. *Molecules* **26**, 3408 (2021).

19. Sundberg, J., Ersson, B., Lönnerdal, B. & Oskarsson, A. Protein binding of mercury in milk and plasma from mice and man — a comparison between methylmercury and inorganic mercury. *Toxicology* **137**, 169–184 (1999).

20. Yasutake, A., Hirayama, K. & Inoue, M. Mechanism of urinary excretion of methylmercury in mice. *Arch Toxicol* **63**, 479–483 (1989).

21. Bridle, T. G., Doroudian, M., White, W. & Gailer, J. Physiologically relevant hCys concentrations mobilize MeHg from rabbit serum albumin to form MeHg–hCys complexes. *Metallomics* **14**, 10 (2022).

22. Morton, J., Mason, H. J., Ritchie, K. A. & White, M. Comparison of hair, nails and urine for biological monitoring of low level inorganic mercury exposure in dental workers. *Biomarkers* **9**, 47–55 (2004).

23. Sakamoto, M. *et al.* Significance of fingernail and toenail mercury concentrations as biomarkers for prenatal methylmercury exposure in relation to segmental hair mercury concentrations. *Environ Res* **136**, 289–294 (2015).

24. Yin, Z. *et al.* The methylmercury-L-cysteine conjugate is a substrate for the L-type large neutral amino acid transporter, LAT1. *J Neurochem* **107**, 1083 (2008).

25. Iverson, F., Downie, R. H., Trenholm, H. L. & Paul, C. Accumulation and tissue distribution of mercury in the guinea pig during subacute administration of methyl mercury. *Toxicol Appl Pharmacol* **27**, 60–69 (1974).

26. Kajiwara, Y., Yasutake, A., Adachi, T. & Hirayama, K. Methylmercury transport across the placenta via neutral amino acid carrier. *Arch Toxicol* **70**, 310–314 (1996).

27. Skerfving, S. Mercury in women exposed to methylmercury through fish consumption, and in their newborn babies and breast milk. *Bull Environ Contam Toxicol* **41**, 475–482 (1988).

28. Uchikawa, T. *et al.* Demethylation of methylmercury and the enhanced production of formaldehyde in mouse liver. *J Toxicol Sci* **41**, 479–487 (2016).

29. Nakamura, I., Hosokawa, K., Tamura, H. & Miura, T. Reduced mercury excretion with feces in germfree mice after oral administration of methyl mercury chloride. *Bull Environ Contam Toxicol* **17**, 528–533 (1977).

30. Rowland, I. R. Interactions of the gut microflora and the host in toxicology. *Toxicol Pathol* **16**, 147–153 (1988).

31. Suzuki, T. *et al.* Normal organic and inorganic mercury levels in the human feto-placental system. *Journal of Applied Toxicology* **4**, 249–252 (1984).

32. Palmisano, F., Cardellicchio, N. & Zambonin, P. G. Speciation of mercury in dolphin liver: A two-stage mechanism for the demethylation accumulation process and role of selenium. *Mar Environ Res* **40**, 109–121 (1995).

33. Björkman, L. *et al.* Mercury in human brain, blood, muscle and toenails in relation to exposure: An autopsy study. *Environ Health* **6**, 1–14 (2007).

34. Vahter, M. *et al.* Speciation of mercury in the primate blood and brain following long-term exposure to methyl mercury. *Toxicol Appl Pharmacol* **124**, 221–229 (1994).

35. Government of Canada. Human Health Risk Assessment of Mercury in Fish and Health Benefits of Fish Consumption. https://www.canada.ca/en/health-canada/services/food-nutrition/reports-publications/human-health-risk-assessment-mercury-fish-health-benefits-fish-consumption.html (2008).

36. Ballatori, N. & Clarkson, T. W. Developmental changes in the biliary excretion of methylmercury and glutathione. *Science (1979)* **216**, 61–63 (1982).

37. Rand, M. D. & Caito, S. W. Variation in the biological half-life of methylmercury in humans: Methods, measurements and meaning. *Biochim Biophys Acta Gen Subj* **1863**, (2019).

38. Berglund, M. *et al.* Inter-individual variations of human mercury exposure biomarkers: A cross-sectional assessment. *Environmental Health* **4**, 1–11 (2005).

39. Smith, J. C. *et al.* The Kinetics of Intravenously Administered Methyl Mercury in Man. *Toxicol Appl Pharmacol* **128**, 251–256 (1994).

40. Hall, B. D., Bodaly, R. A., Fudge, R. J. P., Rudd, J. W. M. & Rosenberg, D. M. Food as the Dominant Pathway of Methylmercury Uptake by Fish. *Water Air Soil Pollut* **100**, 13–24 (1997).

41. Schroeder, W. H. & Munthe, J. Atmospheric mercury—An overview. *Atmos Environ* **32**, 809–822 (1998).

42. Wheatley, B. & Paradis, S. Exposure of Canadian aboriginal peoples to methylmercury. *Water Air Soil Pollut* **80**, 3–11 (1995).

43. Muckle, G., Ayotte, P., Dewailly, É., Jacobson, S. W. & Jacobson, J. L. Prenatal exposure of the northern Québec Inuit infants to environmental contaminants. *Environ Health Perspect* **109**, 1291–1299 (2001).

44. Calao-Ramos, C., Bravo, A. G., Paternina-Uribe, R., Marrugo-Negrete, J. & Díez, S. Occupational human exposure to mercury in artisanal small-scale gold mining communities of Colombia. *Environ Int* **146**, 106216 (2021).

45. Takeuchi, T., Morikawa, N., Matsumoto, H. & Shiraishi, Y. A pathological study of Minamata disease in Japan. *Acta Neuropathol* **2**, 40–57 (1962).

46. Bakir, F. *et al.* Methylmercury Poisoning in Iraq. *New Series* **181**, 230–241 (1973).

47. Harada, M. Minamata Disease: Methylmercury Poisoning in Japan Caused by Environmental Pollution. *Crit Rev Toxicol* **25**, 1–24 (1995).

48. Yorifuji, T., Tsuda, T., Inoue, S., Takao, S. & Harada, M. Long-term exposure to methylmercury and psychiatric symptoms in residents of Minamata, Japan. *Environ Int* **37**, 907–913 (2011).

49. Government of Japan. Minamata Disease The History and Measures - Chapter 2 [MOE]. http://www.env.go.jp/en/chemi/hs/minamata2002/ch2.html (2001).

50. Harada & Y. Congenital (or fetal) Minamate disease. *Minamata disease* 93–117 (1968).

51. Myers, G. J. & Davidson, P. W. Prenatal methylmercury exposure and children: neurologic, developmental, and behavioral research. *Environ Health Perspect* **106**, 841 (1998).

52. Amin-Zaki, L. *et al.* Prenatal Methylmercury Poisoning: Clinical Observations Over Five Years. *American journal of diseases of children* **133**, 172–177 (1979).

53. Grandjean, P. *et al.* Cognitive Deficit in 7-Year-Old Children with Prenatal Exposure to Methylmercury. *Neurotoxicol Teratol* **19**, 417–428 (1997).

54. Prpić, I. *et al.* Prenatal exposure to low-level methylmercury alters the child's fine motor skills at the age of 18 months. *Environ Res* **152**, 369–374 (2017).

55. Karagas, M. R. *et al.* Evidence on the human health effects of low-level methylmercury exposure. *Environ Health Perspect* **120**, 799–806 (2012).

56. Choi, A. L. *et al.* Negative confounding by essential fatty acids in methylmercury neurotoxicity associations. *Neurotoxicol Teratol* **42**, 85–92 (2014).

57. Debes, F., Budtz-Jørgensen, E., Weihe, P., White, R. F. & Grandjean, P. Impact of prenatal methylmercury exposure on neurobehavioral function at age 14 years. *Neurotoxicol Teratol* **28**, 536–547 (2006).

58. Debes, F., Weihe, P. & Grandjean, P. Cognitive deficits at age 22 years associated with prenatal exposure to methylmercury. *Cortex* **74**, 358–369 (2016).

59. van Wijngaarden, E. *et al.* Prenatal methyl mercury exposure in relation to neurodevelopment and behavior at 19 years of age in the Seychelles Child Development Study. *Neurotoxicol Teratol* **39**, 19–25 (2013).

60. Davidson, P. W. *et al.* Effects of Prenatal and Postnatal Methylmercury Exposure From Fish Consumption on Neurodevelopment: Outcomes at 66 Months of Age in the Seychelles Child Development Study. *JAMA* **280**, 701–707 (1998).

61. Jacobson, J. L., Muckle, G., Ayotte, P., Dewailly, É. & Jacobson, S. W. Relation of Prenatal Methylmercury Exposure from Environmental Sources to Childhood IQ. *Environ Health Perspect* **123**, 827–833 (2015).

62. Boucher, O. *et al.* Prenatal Methylmercury, Postnatal Lead Exposure, and Evidence of Attention Deficit/Hyperactivity Disorder among Inuit Children in Arctic Québec. *Environ Health Perspect* **120**, 1456–1461 (2012).

63. Chhetri, P. K. & Das, J. M. Neuroanatomy, Neural Tube Development and Stages. *StatPearls* (2022).

64. Guo, J. & Anton, E. S. Decision Making During Interneuron Migration in the Developing Cerebral Cortex. *Trends Cell Biol* **24**, 342 (2014).

65. Villalba, A., Götz, M. & Borrell, V. The regulation of cortical neurogenesis. *Curr Top Dev Biol* **142**, 1–66 (2021).

66. Postiglione, M. P. & Hippenmeyer, S. Monitoring neurogenesis in the cerebral cortex: An update. *Future Neurol* **9**, 323–340 (2014).

67. Budday, S., Steinmann, P. & Kuhl, E. Physical biology of human brain development. *Front Cell Neurosci* **9**, 257 (2015).

68. Yang, L., Li, Z., Liu, G., Li, X. & Yang, Z. Developmental Origins of Human Cortical Oligodendrocytes and Astrocytes. *Neurosci Bull* **38**, 47–68 (2021).

69. Gal, J. S. *et al.* Molecular and morphological heterogeneity of neural precursors in the mouse neocortical proliferative zones. *J Neurosci* **26**, 1045–1056 (2006).

70. Cadwell, C. R., Bhaduri, A., Mostajo-Radji, M. A., Keefe, M. G. & Nowakowski, T. J. Development and Arealization of the Cerebral Cortex. *Neuron* **103**, 980–1004 (2019).

71. Dwyer, N. D. *et al.* Neural stem cells to cerebral cortex: Emerging mechanisms regulating progenitor behavior and productivity. *Journal of Neuroscience* **36**, 11394–11401 (2016).

72. Clancy, B., Darlington, R. B. & Finlay, B. L. Translating developmental time across mammalian species. *Neuroscience* **105**, 7–17 (2001).

73. Li, X. *et al.* Decoding Cortical Glial Cell Development. *Neurosci Bull* **37**, 440 (2021).

74. Brodmann, K. *Vergleichende Lokalisationslehre der Grosshirnrinde in ihren Prinzipien dargestellt auf Grund des Zellenbaues*. (1909).

75. Zilles, K. Brodmann: a pioneer of human brain mapping—his impact on concepts of cortical organization. *Brain* **141**, 3262 (2018).

76. DeFelipe, J. & Fariñas, I. The pyramidal neuron of the cerebral cortex: morphological and chemical characteristics of the synaptic inputs. *Prog Neurobiol* **39**, 563–607 (1992).

77. Wonders, C. P. & Anderson, S. A. The origin and specification of cortical interneurons. *Nat Rev Neurosci* **7**, 687–696 (2006).

78. Miyashita, Y. Operating principles of the cerebral cortex as a six-layered network in primates: beyond the classic canonical circuit model. *Proc Jpn Acad Ser B Phys Biol Sci* **98**, 93 (2022).

79. Hevner, R. F. *et al.* Tbr1 Regulates Differentiation of the Preplate and Layer 6. *Neuron* **29**, 353–366 (2001).

80. Huang, Y. *et al.* Expression of Transcription Factor Satb2 in Adult Mouse Brain. *Anatomical Record* **296**, 452–461 (2013).

81. Nikouei, K., Muñoz-Manchado, A. B. & Hjerling-Leffler, J. BCL11B/CTIP2 is highly expressed in GABAergic interneurons of the mouse somatosensory cortex. *J Chem Neuroanat* **71**, 1–5 (2016).

82. Cubelos, B. *et al.* Cux-1 and Cux-2 control the development of Reelin expressing cortical interneurons. *Dev Neurobiol* **68**, 917–925 (2008).

83. Kitamura, S. *et al.* A Central Nervous System Disease of Unknown Cause That Occurred in the Minamata Region: Results of an Epidemiological Study. *J Epidemiol* **30**, 3–11 (2020).

84. Shao, Y., Yamamoto, M., Figeys, D., Ning, Z. & Chan, H. M. Proteomic Analysis of Cerebellum in Common Marmoset Exposed to Methylmercury. *Toxicological sciences* **146**, 43–51 (2015).

85. Dietrich, M. O., Mantese, C. E., Anjos, G. dos, Souza, D. O. & Farina, M. Motor impairment induced by oral exposure to methylmercury in adult mice. *Environ Toxicol Pharmacol* **19**, 169–175 (2005).

86. Mattsson, J. L., Miller, E., Alligood, J. P., Koering, J. E. & Levin, S. G. Early effects of methylmercury on the visual evoked response of the dog. *Neurotoxicology* **2**, 499–514 (1981).

87. Bittencourt, L. O. *et al.* Proteomic approach underlying the hippocampal neurodegeneration caused by low doses of methylmercury after long-term exposure in adult rats. *Metallomics* **11**, 390–403 (2019).

88. Franco, J. L. *et al.* Mercurial-induced hydrogen peroxide generation in mouse brain mitochondria: protective effects of quercetin. *Chem Res Toxicol* **20**, 1919–1926 (2007).

89. Mori, N., Yasutake, A. & Hirayama, K. Comparative study of activities in reactive oxygen species production/defense system in mitochondria of rat brain and liver, and their susceptibility to methylmercury toxicity. *Arch Toxicol* **81**, 769–776 (2007).

90. Franco, J. L. *et al.* Methylmercury neurotoxicity is associated with inhibition of the antioxidant enzyme glutathione peroxidase. *Free Radic Biol Med* **47**, 449–457 (2009).

91. Naganuma, A. *et al.* Overexpression of manganese-superoxide dismutase prevents methylmercury toxicity in hela cells. *Life Sci* **62**, 157–161 (1998).

92. Shinyashiki, M. *et al.* Selective inhibition of the mouse brain Mn-SOD by methylmercury. *Environ Toxicol Pharmacol* **2**, 359–366 (1996).

93. Farina, M. *et al.* Methylmercury Increases Glutamate Release from Brain Synaptosomes and Glutamate Uptake by Cortical Slices from Suckling Rat Pups: Modulatory Effect of Ebselen. *Toxicological Sciences* **73**, 135–140 (2003).

94. Porciúncula, L. O. *et al.* Methylmercury inhibits glutamate uptake by synaptic vesicles from rat brain. *Neuroreport* **14**, 577–580 (2003).

95. Reynolds, I. J. & Hastings, T. G. Glutamate induces the production of reactive oxygen species in cultured forebrain neurons following NMDA receptor activation. *J Neurosci* **15**, 3318–3327 (1995).

96. Tymianski, M. & Tator, C. H. Normal and Abnormal Calcium Homeostasis in Neurons: A Basis for the Pathophysiology of Traumatic and Ischemic Central Nervous System Injury. *Neurosurgery* **38**, 1176–1195 (1996).

97. Kaur, P., Aschner, M. & Syversen, T. Glutathione modulation influences methyl mercury induced neurotoxicity in primary cell cultures of neurons and astrocytes. *Neurotoxicology* **27**, 492–500 (2006).

98. da Conceição Nascimento, M., Nascimento, J. L. M. Do, de Lima Silveira, L. C., Da Rocha, J. B. T. & Aschner, M. Mercury and selenium - a review on aspects related to the health of human populations in the Amazon. *Environ Bioindic* **4**, 222–245 (2009).

99. Zhong, L., Arnér, E. S. J. & Holmgren, A. Structure and mechanism of mammalian thioredoxin reductase: The active site is a redox-active selenolthiol/selenenylsulfide formed from the conserved cysteine-selenocysteine sequence. *Proc Natl Acad Sci U S A* **97**, 5854–5859 (2000).

100. Usuki, F., Fujita, E. & Sasagawa, N. Methylmercury activates ASK1/JNK signaling pathways, leading to apoptosis due to both mitochondria- and endoplasmic reticulum (ER)-generated processes in myogenic cell lines. *Neurotoxicology* **29**, 22–30 (2008).

101. Merz, K., Herold, S. & Lie, D. C. CREB in adult neurogenesis - master and partner in the development of adult-born neurons? *European Journal of Neuroscience* **33**, 1078–1086 (2011).

102. Barco, A., Alarcon, J. M. & Kandel, E. R. Expression of constitutively active CREB protein facilitates the late phase of long-term potentiation by enhancing synaptic capture. *Cell* **108**, 689–703 (2002).

103. Nakagawa, S. *et al.* Localization of phosphorylated cAMP response element-binding protein in immature neurons of adult hippocampus. *Journal of Neuroscience* **22**, 9868–9876 (2002).

104. Walton, M. R. & Dragunow, M. Is CREB a key to neuronal survival? *Trends Neurosci* **23**, 48–53 (2000).

105. Unoki, T. *et al.* Methylmercury, an environmental electrophile capable of activation and disruption of the Akt/CREB/Bcl-2 signal transduction pathway in SH-SY5Y cells. *Sci Rep* **6**, 1–10 (2016).

106. Fujimura, M. & Usuki, F. Site-specific neural hyperactivity via the activation of MAPK and PKA/CREB pathways triggers neuronal degeneration in methylmercury-intoxicated mice. *Toxicol Lett* **271**, 66–73 (2017).

107. Fujimura, M. & Usuki, F. Methylmercury induces oxidative stress and subsequent neural hyperactivity leading to cell death through the p38 MAPK-CREB pathway in differentiated SH-SY5Y cells. *Neurotoxicology* **67**, 226–233 (2018).

108. Wang, L., Jiang, H., Yin, Z., Aschner, M. & Cai, J. Methylmercury toxicity and Nrf2-dependent detoxification in astrocytes. *Toxicological Sciences* **107**, 135–143 (2009).

109. Ni, M. *et al.* Methylmercury induces acute oxidative stress, altering Nrf2 protein level in primary microglial cells. *Toxicological Sciences* **116**, 590–603 (2010).

110. Toyama, T. *et al.* Cytoprotective role of Nrf2/Keap1 system in methylmercury toxicity. *Biochem Biophys Res Commun* **363**, 645–650 (2007).

111. Li, B., Qiao, C., Jin, X. & Chan, H. M. Characterizing the Low-Dose Effects of Methylmercury on the Early Stages of Embryo Development Using Cultured Human Embryonic Stem Cells. *Environ Health Perspect* **129**, (2021).

112. Qiu, Q. *et al.* Noninvasive Dual-Modality Photoacoustic-Ultrasonic Imaging to Detect Mammalian Embryo Abnormalities after Prenatal Exposure to Methylmercury Chloride (MMC): A Mouse Study. *Environ Health Perspect* **130**, (2022).

113. Smith, J. H., McCormack, K. M., Braselton, W. E. & Hook, J. B. The effect of prenatal methylmercury administration on postnatal renal functional development. *Environ Res* **30**, 63–71 (1983).

114. Choi, B. H., Lapham, L. W., Amin-Zaki, L. & Saleem, T. Abnormal neuronal migration, deranged cerebral cortical organization, and diffuse white matter astrocytosis of human fetal brain: A major effect of methylmercury poisoning in utero. *J Neuropathol Exp Neurol* **37**, 719–733 (1978).

115. Weiss, B., Stern, S., Cox, C. & Balys, M. Perinatal and lifetime exposure to methylmercury in the mouse: behavioral effects. *Neurotoxicology* **26**, 675–690 (2005).

116. Goulet, S., Doré, F. Y. & Mirault, M. E. Neurobehavioral changes in mice chronically exposed to methylmercury during fetal and early postnatal development. *Neurotoxicol Teratol* **25**, 335–347 (2003).

117. Onishchenko, N. *et al.* Developmental exposure to methylmercury alters learning and induces depression-like behavior in male mice. *Toxicological Sciences* **97**, 428–437 (2007).

118. Montgomery, K. S. *et al.* Chronic, low-dose prenatal exposure to methylmercury impairs motor and mnemonic function in adult C57/B6 mice. *Behavioural brain research* **191**, 55–61 (2008).

119. Inouye, M., Murao, K. & Kajiwara, Y. Behavioral and neuropathological effects of prenatal methylmercury exposure in mice. *Neurobehav Toxicol Teratol* **7**, 227–232 (1985).

120. Reuhl, K. R., Chang, L. W. & Townsend, J. W. Pathological effects of in utero methylmercury exposure on the cerebellum of the golden hamster: I. Early effects upon the neonatal cerebellar cortex. *Environ Res* **26**, 281–306 (1981).

121. Guo, B. Q., Yan, C. H., Cai, S. Z., Yuan, X. B. & Shen, X. M. Low level prenatal exposure to methylmercury disrupts neuronal migration in the developing rat cerebral cortex. *Toxicology* **304**, 57–68 (2013).

122. Kakita, A., Inenaga, C., Sakamoto, M. & Takahashi, H. Neuronal migration disturbance and consequent cytoarchitecture in the cerebral cortex following transplacental administration of methylmercury. *Acta Neuropathol* **104**, 409–417 (2002).

123. Ferraro, L. *et al.* Developmental exposure to methylmercury elicits early cell death in the cerebral cortex and long-term memory deficits in the rat. *International Journal of Developmental Neuroscience* **27**, 165–174 (2009).

124. Peckham, N. H. & Choi, B. H. Abnormal neuronal distribution within the cerebral cortex after prenatal methylmercury intoxication. *Acta Neuropathol* **76**, 222–226 (1988).

125. Jebbett, N. J., Hamilton, J. W., Rand, M. D. & Eckenstein, F. Low level methylmercury enhances CNTF-evoked STAT3 signaling and glial differentiation in cultured cortical progenitor cells. *Neurotoxicology* **38**, 91–100 (2013).

126. Yuan, X., Wang, J. & Chan, H. M. Correction: Yuan et al. Sub-Micromolar Methylmercury Exposure Promotes Premature Differentiation of Murine Embryonic Neural Precursor at the Expense of Their Proliferation. Toxics 2018, 6, 61. *Toxics* **9**, 322 (2021).

127. Xu, M., Yan, C., Tian, Y., Yuan, X. & Shen, X. Effects of low level of methylmercury on proliferation of cortical progenitor cells. *Brain Res* **1359**, 272–280 (2010).

128. Bose, R., Onishchenko, N., Edoff, K., Lang, A. M. J. & Ceccatelli, S. Inherited effects of low-dose exposure to methylmercury in neural stem cells. *Toxicological Sciences* **130**, 383–390 (2012).

129. Fujimura, M. & Usuki, F. Low concentrations of methylmercury inhibit neural progenitor cell proliferation associated with up-regulation of glycogen synthase kinase 3 beta and subsequent degradation of cyclin E in rats. *Toxicol Appl Pharmacol* **288**, 19–25 (2015).

130. Burke, K. *et al.* Methylmercury elicits rapid inhibition of cell proliferation in the developing brain and decreases cell cycle regulator, cyclin E. *Neurotoxicology* **27**, 970–981 (2006).

131. Tasneem, S., Farrell, K., Lee, M. Y. & Kothapalli, C. R. Sensitivity of neural stem cell survivalpe, differentiation and neurite outgrowth within 3D hydrogels to environmental heavy metals. *Toxicol Lett* **242**, 9–22 (2016).

132. Tamm, C., Duckworth, J., Hermanson, O. & Ceccatelli, S. High susceptibility of neural stem cells to methylmercury toxicity: Effects on cell survival and neuronal differentiation. *J Neurochem* **97**, 69–78 (2006).

133. Tamm, C., Duckworth, J. K., Hermanson, O. & Ceccatelli, S. Methylmercury inhibits differentiation of rat neural stem cells via Notch signalling. *Neuroreport* **19**, 339–343 (2008).

134. Tian, J. *et al.* MeHg Suppressed Neuronal Potency of Hippocampal NSCs Contributing to the Puberal Spatial Memory Deficits. *Biol Trace Elem Res* **172**, 424–436 (2016).

135. Young, J. F., Wosilait, W. D. & Luecke, R. H. Analysis of Methylmercury Disposition in Humans Utilizing a PBPK Model and Animal Pharmacokinetic Data. *J Toxicol Environ Health A* **63**, 19–52 (2001).

136. Nadarajah, B. & Parnavelas, J. G. Modes of neuronal migration in the developing cerebral cortex. *Nat Rev Neurosci* **3**, 423–432 (2002).

137. Marín, O. & Rubenstein, J. L. R. A long, remarkable journey: Tangential migration in the telencephalon. *Nat Rev Neurosci* **2**, 780–790 (2001).

138. Sass, J. B., Haselow, D. T. & Silbergeld, E. K. Methylmercury-induced decrement in neuronal migration may involve cytokine-dependent mechanisms: a novel method to assess neuronal movement in vitro. *Toxicol Sci* **63**, 74–81 (2001).

139. Zimmer, B. *et al.* Evaluation of Developmental Toxicants and Signaling Pathways in a Functional Test Based on the Migration of Human Neural Crest Cells. *Environ Health Perspect* **120**, 1116–1122 (2012).

140. Kanner, L. Autism disturbances of affective contact. *Nervous Child* **2**, 217–250 (1943).

141. Diagnostic Criteria | Autism Spectrum Disorder (ASD) | CDC. *2022* https://www.cdc.gov/ncbddd/autism/hcp-dsm.html.

142. Bougeard, C., Picarel-Blanchot, F., Schmid, R., Campbell, R. & Buitelaar, J. Prevalence of Autism Spectrum Disorder and Co-morbidities in Children and Adolescents: A Systematic Literature Review. *Front Psychiatry* **12**, 1834 (2021).

143. Fombonne, E. Epidemiology of Pervasive Developmental Disorders. *Pediatr Res* **65**, 591–598 (2009).

144. Kim, Y. S. *et al.* Prevalence of autism spectrum disorders in a total population sample. *American Journal of Psychiatry* **168**, 904–912 (2011).

145. Mattila, M. L. *et al.* Autism Spectrum Disorders According to DSM-IV-TR and Comparison With DSM-5 Draft Criteria: An Epidemiological Study. *J Am Acad Child Adolesc Psychiatry* **50**, 583-592.e11 (2011).

146. Idring, S. *et al.* Autism Spectrum Disorders in the Stockholm Youth Cohort: Design, Prevalence and Validity. *PLoS One* **7**, e41280 (2012).

147. Kirkovski, M., Enticott, P. G. & Fitzgerald, P. B. A review of the role of female gender in autism spectrum disorders. *J Autism Dev Disord* **43**, 2584–2603 (2013).

148. Hiller, R. M., Young, R. L. & Weber, N. Sex differences in pre-diagnosis concerns for children later diagnosed with autism spectrum disorder. *Autism* **20**, 75–84 (2016).

149. Halladay, A. K. *et al.* Sex and gender differences in autism spectrum disorder: summarizing evidence gaps and identifying emerging areas of priority. *Mol Autism* **6**, (2015).

150. Mandy, W. *et al.* Sex differences in autism spectrum disorder: Evidence from a large sample of children and adolescents. *J Autism Dev Disord* **42**, 1304–1313 (2012).

151. Messinger, D. S. *et al.* Early sex differences are not autism-specific: A Baby Siblings Research Consortium (BSRC) study. *Mol Autism* **6**, 1–12 (2015).

152. Baron-Cohen, S. The extreme male brain theory of autism. *Trends Cogn Sci* **6**, 248–254 (2002).

153. Jacquemont, S. *et al.* A Higher Mutational Burden in Females Supports a "Female Protective Model" in Neurodevelopmental Disorders. *The American Journal of Human Genetics* **94**, 415–425 (2014).

154. Dougherty, J. D. *et al.* Can the "female protective effect" liability threshold model explain sex differences in autism spectrum disorder? *Neuron* **110**, 3243–3262 (2022).

155. le Couteur, A. L. *et al.* Autism as a strongly genetic disorder: evidence from a British twin study. *Psychol Med* **25**, 63–77 (1995).

156. le Couteur, A. *et al.* A broader phenotype of autism: the clinical spectrum in twins. *J Child Psychol Psychiatry* **37**, 785–801 (1996).

157. Ritvo, E. R., Freeman, B. J., Mason-Brothers, A. & Mo, A. Concordance for the syndrome of autism in 40 pairs of afflicted twins. *Am J Psychiatry* **142**, 74–77 (1985).

158. Steffenburg, S. *et al.* A twin study of autism in Denmark, Finland, Iceland, Norway and Sweden. *J Child Psychol Psychiatry* **30**, 405–416 (1989).

159. Huguet, G., Benabou, M. & Bourgeron, T. *The genetics of autism spectrum disorders*. *Research and Perspectives in Endocrine Interactions* (Springer Verlag, 2016). doi:10.1007/978-3-319-27069-2_11.

160. Fernandez, B. A. & Scherer, S. W. Syndromic autism spectrum disorders: moving from a clinically defined to a molecularly defined approach. *Dialogues Clin Neurosci* **19**, 353 (2017).

161. Anney, R. *et al.* Individual common variants exert weak effects on the risk for autism spectrum disorders. *Hum Mol Genet* **21**, 4781–4792 (2012).

162. Smoller, J. W. *et al.* Identification of risk loci with shared effects on five major psychiatric disorders: a genome-wide analysis. *Lancet* **381**, 1371–1379 (2013).

163. Jiang, C. C. *et al.* Signalling pathways in autism spectrum disorder: mechanisms and therapeutic implications. *Signal Transduct Target Ther* **7**, (2022).

164. Malkova, N. v., Yu, C. Z., Hsiao, E. Y., Moore, M. J. & Patterson, P. H. Maternal immune activation yields offspring displaying mouse versions of the three core symptoms of autism. *Brain Behav Immun* **26**, 607–616 (2012).

165. Lucchina, L. & Depino, A. M. Altered Peripheral and Central Inflammatory Responses in a Mouse Model of Autism. *Autism Research* **7**, 273–289 (2014).

166. Roullet, F. I., Lai, J. K. Y. & Foster, J. A. In utero exposure to valproic acid and autism--a current review of clinical and animal studies. *Neurotoxicol Teratol* **36**, 47–56 (2013).

167. Abbott, A. E. *et al.* Repetitive behaviors in autism are linked to imbalance of corticostriatal connectivity: a functional connectivity MRI study. *Soc Cogn Affect Neurosci* **13**, 32 (2018).

168. Rădulescu, A., Herron, J., Kennedy, C. & Scimemi, A. Global and local excitation and inhibition shape the dynamics of the cortico-striatal-thalamo-cortical pathway. *Sci Rep* **7**, 1–21 (2017).

169. di Martino, A. *et al.* Aberrant striatal functional connectivity in children with autism. *Biol Psychiatry* **69**, 847–856 (2011).

170. Rojas, D. C. *et al.* Regional gray matter volumetric changes in autism associated with social and repetitive behavior symptoms. *BMC Psychiatry* **6**, 1–13 (2006).

171. Langen, M. *et al.* Changes in the Developmental Trajectories of Striatum in Autism. *Biol Psychiatry* **66**, 327–333 (2009).

172. Estes, A. *et al.* Basal ganglia morphometry and repetitive behavior in young children with autism spectrum disorder. *Autism Res* **4**, 212–220 (2011).

173. Barak, B. & Feng, G. Neurobiology of social behavior abnormalities in autism and Williams syndrome. *Nat Neurosci* **19**, 647–655 (2016).

174. Kim, S. Y. *et al.* Abnormal Activation of the Social Brain Network in Children with Autism Spectrum Disorder: An fMRI Study. *Psychiatry Investig* **12**, 37 (2015).

175. Humphreys, K., Hasson, U., Avidan, G., Minshew, N. & Behrmann, M. Cortical patterns of category-selective activation for faces, places and objects in adults with autism. *Autism Research* **1**, 52–63 (2008).

176. Dalton, K. M. *et al.* Gaze fixation and the neural circuitry of face processing in autism. *Nat Neurosci* **8**, 519–526 (2005).

177. Just, M. A., Cherkassky, V. L., Keller, T. A. & Minshew, N. J. Cortical activation and synchronization during sentence comprehension in high-functioning autism: evidence of underconnectivity. *Brain* **127**, 1811–1821 (2004).

178. Kana, R. K., Keller, T. A., Cherkassky, V. L., Minshew, N. J. & Just, M. A. Sentence comprehension in autism: thinking in pictures with decreased functional connectivity. *Brain* **129**, 2484–2493 (2006).

179. Wang, A. T., Lee, S. S., Sigman, M. & Dapretto, M. Neural basis of irony comprehension in children with autism: the role of prosody and context. *Brain* **129**, 932–943 (2006).

180. McCaffery, P. & Deutsch, C. K. Macrocephaly and the control of brain growth in autistic disorders. *Prog Neurobiol* **77**, 38–56 (2005).

181. Courchesne, E. Abnormal early brain development in autism. *Mol Psychiatry* **10**, 106–111 (2002).

182. Nordahl, C. W. *et al.* Brain enlargement is associated with regression in preschool-age boys with autism spectrum disorders. *Proceedings of the National Academy of Sciences* **108**, 20195–20200 (2011).

183. Carper, R. A., Moses, P., Tigue, Z. D. & Courchesne, E. Cerebral Lobes in Autism: Early Hyperplasia and Abnormal Age Effects. *Neuroimage* **16**, 1038–1051 (2002).

184. Lange, N. *et al.* Longitudinal Volumetric Brain Changes in Autism Spectrum Disorder Ages 6–35 Years. *Autism Research* **8**, 82–93 (2015).

185. Movsas, T. *et al.* Autism spectrum disorder is associated with ventricular enlargement in a low birth weight population. *J Pediatr* **163**, 73–80 (2013).

186. Wolfe, F. H., Auzias, G., Deruelle, C. & Chaminade, T. Focal atrophy of the hypothalamus associated with third ventricle enlargement in autism spectrum disorder. *Neuroreport* **26**, 1017–1022 (2015).

187. Lotspeich, L. J. *et al.* Investigation of neuroanatomical differences between autism and aspergersyndrome. *Arch Gen Psychiatry* **61**, 291–298 (2004).

188. Courchesne, E., Carper, R. & Akshoomoff, N. Evidence of brain overgrowth in the first year of life in autism. *JAMA* **290**, 337–344 (2003).

189. Casanova, M. F., Herbert, M. R. & Ziegler, D. A. White matter volume increase and minicolumns in autism. *Ann Neurol* **56**, 453–453 (2004).

190. Herbert, M. R. *et al.* Dissociations of cerebral cortex, subcortical and cerebral white matter volumes in autistic boys. *Brain* **126**, 1182–1192 (2003).

191. Smith, E. *et al.* Cortical thickness change in autism during early childhood. *Hum Brain Mapp* **37**, 2616–2629 (2016).

192. Khundrakpam, B. S., Lewis, J. D., Kostopoulos, P., Carbonell, F. & Evans, A. C. Cortical Thickness Abnormalities in Autism Spectrum Disorders Through Late Childhood, Adolescence, and Adulthood: A Large-Scale MRI Study. *Cerebral Cortex* **27**, 1721–1731 (2017).

193. Zielinski, B. A. *et al.* Longitudinal changes in cortical thickness in autism and typical development. *Brain* **137**, 1799–1812 (2014).

194. Casanova, M. F. *et al.* Minicolumnar abnormalities in autism. *Acta Neuropathol* **112**, 287–303 (2006).

195. Courchesne, E. *et al.* Neuron Number and Size in Prefrontal Cortex of Children With Autism. *JAMA* **306**, 2001–2010 (2011).

196. Gandhi, T. & Lee, C. C. Neural Mechanisms Underlying Repetitive Behaviors in Rodent Models of Autism Spectrum Disorders. *Front Cell Neurosci* **14**, 463 (2021).

197. Kim, H., Lim, C. S. & Kaang, B. K. Neuronal mechanisms and circuits underlying repetitive behaviors in mouse models of autism spectrum disorder. *Behavioral and Brain Functions* **12**, 1–13 (2016).

198. Ko, J. Neuroanatomical Substrates of Rodent Social Behavior: The Medial Prefrontal Cortex and Its Projection Patterns. *Front Neural Circuits* **11**, (2017).

199. Hammerschmidt, K., Whelan, G., Eichele, G. & Fischer, J. Mice lacking the cerebral cortex develop normal song: Insights into the foundations of vocal learning. *Sci Rep* **5**, (2015).

200. Martucci, L. L. *et al.* A multiscale analysis in CD38-/- mice unveils major prefrontal cortex dysfunctions. *FASEB J* **33**, 5823–5835 (2019).

201. Steadman, P. E. *et al.* Genetic effects on cerebellar structure across mouse models of autism using a magnetic resonance imaging atlas. *Autism Research* **7**, 124–137 (2014).

202. Smith, S. E. P., Elliott, R. M. & Anderson, M. P. Maternal immune activation increases neonatal mouse cortex thickness and cell density. *Journal of Neuroimmune Pharmacology* **7**, 529–532 (2012).

203. Sabers, A., Bertelsen, F. C. B., Scheel-Krüger, J., Nyengaard, J. R. & Møller, A. Long-term valproic acid exposure increases the number of neocortical neurons in the developing rat brain. A possible new animal model of autism. *Neurosci Lett* **580**, 12–16 (2014).

204. Fang, W. Q. *et al.* Overproduction of Upper-Layer Neurons in the Neocortex Leads to Autism-like Features in Mice. *Cell Rep* **9**, 1635–1643 (2014).

205. Zhang, W. *et al.* Cerebral organoid and mouse models reveal a RAB39b-PI3K-mTOR pathway-dependent dysregulation of cortical development leading to macrocephaly/ autism phenotypes. *Genes Dev* **34**, 580–597 (2020).

206. Schoen, M. *et al.* Shank3 transgenic and prenatal zinc-deficient autism mouse models show convergent and individual alterations of brain structures in MRI. *Front Neural Circuits* **13**, 6 (2019).

207. Kumar, M. *et al.* High resolution magnetic resonance imaging for characterization of the neuroligin-3 knock-in mouse model associated with autism spectrum disorder. *PLoS One* **9**, (2014).

208. Dodero, L. *et al.* Neuroimaging Evidence of Major Morpho-Anatomical and Functional Abnormalities in the BTBR T+TF/J Mouse Model of Autism. *PLoS One* **8**, (2013).

209. Notwell, J. H. *et al.* TBR1 regulates autism risk genes in the developing neocortex. *Genome Res* **26**, 1013–1022 (2016).

210. Falcone, C. *et al.* Neuronal and Glial Cell Number is Altered in a Cortical Layer-Specific Manner in Autism. *Autism* **25**, 2238 (2021).

211. Trutzer, I. M., García-Cabezas, M. Á. & Zikopoulos, B. Postnatal development and maturation of layer 1 in the lateral prefrontal cortex and its disruption in autism. *Acta Neuropathol Commun* **7**, 40 (2019).

212. Pucilowska, J. *et al.* The 16p11.2 deletion mouse model of autism exhibits altered cortical progenitor proliferation and brain cytoarchitecture linked to the ERK MAPK pathway. *Journal of Neuroscience* **35**, 3190–3200 (2015).

213. Fenlon, L. R. *et al.* Formation of functional areas in the cerebral cortex is disrupted in a mouse model of autism spectrum disorder. *Neural Dev* **10**, 1–14 (2015).

214. Gauthier, J. *et al.* Truncating mutations in NRXN2 and NRXN1 in autism spectrum disorders and schizophrenia. *Hum Genet* **130**, 563–573 (2011).

215. El-Ansary, A. & Al-Ayadhi, L. GABAergic/glutamatergic imbalance relative to excessive neuroinflammation in autism spectrum disorders. *J Neuroinflammation* **11**, 1–9 (2014).

216. Shinohe, A. *et al.* Increased serum levels of glutamate in adult patients with autism'. *Prog Neuropsychopharmacol Biol Psychiatry* **30**, 1472–1477 (2006).

217. Harada, M. *et al.* Non-invasive evaluation of the GABAergic/glutamatergic system in autistic patients observed by MEGA-editing proton MR spectroscopy using a clinical 3 tesla instrument. *J Autism Dev Disord* **41**, 447–454 (2011).

218. Barnby, G. *et al.* Candidate-gene screening and association analysis at the autism-susceptibility locus on chromosome 16p: Evidence of association at GRIN2A and ABAT. *Am J Hum Genet* **76**, 950–966 (2005).

219. Yoo, H. J., Cho, I. H., Park, M., Yang, S. Y. & Kim, S. A. Family based association of GRIN2A and GRIN2B with Korean autism spectrum disorders. *Neurosci Lett* **512**, 89–93 (2012).

220. Gauthier, J. *et al.* De novo mutations in the gene encoding the synaptic scaffolding protein SHANK3 in patients ascertained for schizophrenia. *Proc Natl Acad Sci U S A* **107**, 7863–7868 (2010).

221. Durand, C. M. *et al.* Mutations in the gene encoding the synaptic scaffolding protein SHANK3 are associated with autism spectrum disorders. *Nat Genet* **39**, 25–27 (2007).

222. Gauthier, J. *et al.* Novel de novo SHANK3 mutation in autistic patients. *American Journal of Medical Genetics, Part B: Neuropsychiatric Genetics* **150**, 421–424 (2009).

223. Jamain, S. *et al.* Mutations of the X-linked genes encoding neuroligins NLGN3 and NLGN4 are associated with autism. *Nat Genet* **34**, 27–29 (2003).

224. Laumonnier, F. *et al.* X-Linked Mental Retardation and Autism Are Associated with a Mutation in the NLGN4 Gene, a Member of the Neuroligin Family. *Am J Hum Genet* **74**, 552–557 (2004).

225. Kim, J. W. *et al.* Pharmacological modulation of AMPA receptor rescues social impairments in animal models of autism. *Neuropsychopharmacology* **44**, 314–323 (2019).

226. Erickson, C. A. *et al.* A retrospective study of memantine in children and adolescents with pervasive developmental disorders. *Psychopharmacology (Berl)* **191**, 141–147 (2007).

227. Erickson, C. A. *et al.* An Open-Label Naturalistic Pilot Study of Acamprosate in Youth with Autistic Disorder. *J Child Adolesc Psychopharmacol* **21**, 565–569 (2011).

228. Thimerosal and Vaccines | FDA. https://www.fda.gov/vaccines-blood-biologics/safety-availability-biologics/thimerosal-and-vaccines.

229. Price, C. S. *et al.* Prenatal and infant exposure to thimerosal from vaccines and immunoglobulins and risk of autism. *Pediatrics* **126**, 656–664 (2010).

230. Cohen, J. T., Bellinger, D. C. & Shaywitz, B. A. A Quantitative Analysis of Prenatal Methyl Mercury Exposure and Cognitive Development. *Am J Prev Med* **29**, 353–365 (2005).

231. Axelrad, D. A., Bellinger, D. C., Ryan, L. M. & Woodruff, T. J. Dose-response relationship of prenatal mercury exposure and IQ: An integrative analysis of epidemiologic data. *Environ Health Perspect* **115**, 609–615 (2007).

232. Charman, T. *et al.* IQ in children with autism spectrum disorders: data from the Special Needs and Autism Project (SNAP). *Psychol Med* **41**, 619–627 (2011).

233. Geier, D. A., Audhya, T., Kern, J. K. & Geier, M. R. Blood mercury levels in autism spectrum disorder: Is there a threshold level? *Acta Neurobiol Exp (Wars)* **70**, 177–186 (2010).

234. Blaurock-Busch, E., Amin, O. R. & Rabah, T. Heavy Metals and Trace Elements in Hair and Urine of a Sample of Arab Children with Autistic Spectrum Disorder. *Maedica (Bucur)* **6**, 247–257 (2011).

235. Lakshmi Priya, M. D. & Geetha, A. Level of trace elements (copper, zinc, magnesium and selenium) and toxic elements (lead and mercury) in the hair and nail of children with autism. *Biol Trace Elem Res* **142**, 148–158 (2011).

236. Fido, A. & Al-Saad, S. Toxic trace elements in the hair of children with autism. *Autism* **9**, 290–298 (2005).

237. Elsheshtawy, E., Tobar, S., Sherra, K., Atallah, S. & Elkasaby, R. Study of some biomarkers in hair of children with autism. *Middle East Current Psychiatry* **18**, 6–10 (2011).

238. El-baz, F., Elhossiny, R. M., Elsayed, A. B. & Gaber, G. M. Hair mercury measurement in Egyptian autistic children. *Egyptian Journal of Medical Human Genetics* **11**, 135–141 (2010).

239. Al-Ayadhi, L. Y. Heavy metals and trace elements in hair samples of autistic children in central Saudi Arabia. *Neurosciences Journal* **10**, 213–218 (2005).

240. Adams, J. B., Romdalvik, J., Ramanujam, V. M. S. & Legator, M. S. Mercury, lead, and zinc in baby teeth of children with autism versus controls. *J Toxicol Environ Health A* **70**, 1046–1051 (2007).

241. Hertz-Picciotto, I. *et al.* Blood mercury concentrations in CHARGE study children with and without autism. *Environ Health Perspect* **118**, 161–166 (2010).

242. Stamova, B. *et al.* Correlations between gene expression and mercury levels in blood of boys with and without autism. *Neurotox Res* **19**, 31–48 (2011).

243. Albizzati, A., Morè, L., Di Candia, D., Saccani, M. & Lenti, C. Normal concentrations of heavy metals in autistic spectrum disorders. *Minerva Pediatr* **64**, 27–31 (2012).

244. Wright, B. *et al.* A comparison of urinary mercury between children with autism spectrum disorders and control children. *PLoS One* **7**, (2012).

245. Adams, J. B., Holloway, C. E., George, F. & Quig, D. Analyses of toxic metals and essential minerals in the hair of Arizona children with autism and associated conditions, and their mothers. *Biol Trace Elem Res* **110**, 193–209 (2006).

246. Adams, J. B., Romdalvik, J., Levine, K. E. & Hu, L. W. Mercury in first-cut baby hair of children with autism versus typically-developing children. *Toxicol Environ Chem* **90**, 739–753 (2008).

247. de Palma, G., Catalani, S., Franco, A., Brighenti, M. & Apostoli, P. Lack of correlation between metallic elements analyzed in hair by ICP-MS and autism. *J Autism Dev Disord* **42**, 342–353 (2012).

248. Ip, P., Wong, V., Ho, M., Lee, J. & Wong, W. Mercury exposure in children with autistic spectrum disorder: Case-control study. *J Child Neurol* **19**, 431–434 (2004).

249. Williams, P. G., Hersh, J. H., Allard, A. M. & Sears, L. L. A controlled study of mercury levels in hair samples of children with autism as compared to their typically developing siblings. *Res Autism Spectr Disord* **2**, 170–175 (2008).

250. Wecker, L., Miller, S. B., Cochran, S. R., Dugger, D. L. & Johnson, W. D. Trace element concentrations in hair from autistic children. *J Ment Defic Res* **29 (Pt 1)**, 15–22 (1985).

251. Kern, J. K., Grannemann, B. D., Trivedi, M. H. & Adams, J. B. Sulfhydryl-reactive metals in autism. *J Toxicol Environ Health A* **70**, 715–721 (2007).

252. Abdullah, M. M. *et al.* Heavy metal in children's tooth enamel: Related to autism and disruptive behaviors? *J Autism Dev Disord* **42**, 929–936 (2012).

253. Sajdel-Sulkowska, E. M., Lipinski, B., Windom, H., Audhya, T. & McGinnis, W. Oxidative Stress in Autism: Elevated Cerebellar 3-nitrotyrosine Levels. *Am J Biochem Biotechnol* **4**, 73–84 (2008).

254. Holmes, A. S., Blaxill, M. F. & Haley, B. E. Reduced levels of mercury in first baby haircuts of autistic children. *Int J Toxicol* **22**, 277–285 (2003).

255. Obrenovich, M. E., Shamberger, R. J. & Lonsdale, D. Altered heavy metals and transketolase found in autistic spectrum disorder. *Biol Trace Elem Res* **144**, 475–486 (2011).

256. Majewska, M. D., Urbanowicz, E., Rok-Bujko, P., Namysłowska, I. & Mierzejewski, P. Age-dependent lower or higher levels of hair mercury in autistic children than in healthy controls. *Acta Neurobiol Exp (Wars)* **70**, 196–208 (2010).

257. Bose-O'Reilly, S., McCarty, K. M., Steckling, N. & Lettmeier, B. Mercury Exposure and Children's Health. *Curr Probl Pediatr Adolesc Health Care* **40**, 186–215 (2010).

258. Oken, E. *et al.* Associations of maternal fish intake during pregnancy and breastfeeding duration with attainment of developmental milestones in early childhood: a study from the Danish National Birth Cohort. *Am J Clin Nutr* **88**, 789–796 (2008).

259. Al-Mazroua, H. A. *et al.* Methylmercury chloride exposure exacerbates existing neurobehavioral and immune dysfunctions in the BTBR T+ Itpr3tf/J mouse model of autism. *Immunol Lett* **244**, 19–27 (2022).

260. Attia, S. M. *et al.* Multiple exposure to methylmercury aggravates DNA damage in the BTBR T + Itpr3 tf/J autistic mouse model: The role of DNA repair efficiency. *Toxicology* **477**, 153277 (2022).

261. James, S. J. *et al.* Metabolic biomarkers of increased oxidative stress and impaired methylation capacity in children with autism. *Am J Clin Nutr* **80**, 1611–1617 (2004).

262. Castejon, A. M. *et al.* Improving Antioxidant Capacity in Children With Autism: A Randomized, Double-Blind Controlled Study With Cysteine-Rich Whey Protein. *Front Psychiatry* **12**, 669089 (2021).

263. Chen, L. *et al.* Oxidative stress marker aberrations in children with autism spectrum disorder: a systematic review and meta-analysis of 87 studies (N = 9109). *Transl Psychiatry* **11**, 1–10 (2021).

264. James, S. J. *et al.* Cellular and mitochondrial glutathione redox imbalance in lymphoblastoid cells derived from children with autism. *The FASEB Journal* **23**, 2374–2383 (2009).

265. Barcelos, G. R. M. *et al.* Evaluation of Glutathione S-transferase GSTM1 and GSTT1 Polymorphisms and Methylmercury Metabolism in an Exposed Amazon Population. *J Toxicol Environ Health A* **75**, 960–970 (2012).

266. Lee, B.-E. *et al.* Interaction between GSTM1/GSTT1 polymorphism and blood mercury on birth weight. *Environ Health Perspect* **118**, 437–443 (2010).

267. Rahbar, M. H. *et al.* Associations of Metabolic Genes (GSTT1, GSTP1, GSTM1) and Blood Mercury Concentrations Differ in Jamaican Children with and without Autism Spectrum Disorder. *Int J Environ Res Public Health* **18**, 1–20 (2021).

268. Hodgson, N. W. *et al.* Decreased glutathione and elevated hair mercury levels are associated with nutritional deficiency-based autism in Oman. *Exp Biol Med (Maywood)* **239**, 697–706 (2014).

269. Engström, K. S. *et al.* Genetic variation in glutathione-related genes and body burden of methylmercury. *Environ Health Perspect* **116**, 734–739 (2008).

270. He, L. & Wondisford, F. E. Metformin action: concentrations matter. *Cell Metab* **21**, 159–162 (2015).

271. Nasri, H. & Rafieian-Kopaei, M. Metformin: Current knowledge. *J Res Med Sci* **19**, 658–664 (2014).

272. Shirasaka, Y. *et al.* Multiple Transport Mechanisms Involved in the Intestinal Absorption of Metformin: Impact on the Nonlinear Absorption Kinetics. *J Pharm Sci* **111**, 1531–1541 (2022).

273. Szymczak-Pajor, I., Wenclewska, S. & Śliwińska, A. Metabolic Action of Metformin. *Pharmaceuticals* **15**, 810 (2022).

274. Gong, L., Goswami, S., Giacomini, K. M., Altman, R. B. & Klein, T. E. Metformin pathways: pharmacokinetics and pharmacodynamics. *Pharmacogenet Genomics* **22**, 820–827 (2012).

275. Zake, D. M. *et al.* Physiologically based metformin pharmacokinetics model of mice and scale-up to humans for the estimation of concentrations in various tissues. *PLoS One* **16**, (2021).

276. Łabuzek, K. *et al.* Quantification of metformin by the HPLC method in brain regions, cerebrospinal fluid and plasma of rats treated with lipopolysaccharide. *Pharmacological Reports* **62**, 956–965 (2010).

277. Sluggett, J. K. *et al.* Metformin and Risk of Alzheimer's Disease Among Community-Dwelling People With Diabetes: A National Case-Control Study. *J Clin Endocrinol Metab* **105**, (2020).

278. Westphal, L. P. *et al.* Association of prestroke metformin use, stroke severity, and thrombolysis outcome. *Neurology* **95**, e362–e373 (2020).

279. Hervás, D. *et al.* Metformin intake associates with better cognitive function in patients with Huntington's disease. *PLoS One* **12**, (2017).

280. Wang, J. *et al.* Metformin activates an atypical PKC-CBP pathway to promote neurogenesis and enhance spatial memory formation. *Cell Stem Cell* **11**, 23–35 (2012).

281. Jin, Q. *et al.* Improvement of functional recovery by chronic metformin treatment is associated with enhanced alternative activation of microglia/macrophages and increased angiogenesis and neurogenesis following experimental stroke. *Brain Behav Immun* **40**, 131–142 (2014).

282. Liu, Y., Tang, G., Zhang, Z., Wang, Y. & Yang, G. Y. Metformin promotes focal angiogenesis and neurogenesis in mice following middle cerebral artery occlusion. *Neurosci Lett* **579**, 46–51 (2014).

283. Lin, C. J. *et al.* Cellular localization of the organic cation transporters, OCT1 and OCT2, in brain microvessel endothelial cells and its implication for MPTP transport across the blood-brain barrier and MPTP-induced dopaminergic toxicity in rodents. *J Neurochem* **114**, 717–727 (2010).

284. Chaves, C. *et al.* An Interspecies Molecular and Functional Study of Organic Cation Transporters at the Blood-Brain Barrier: From Rodents to Humans. *Pharmaceutics* **12**, 308 (2020).

285. Vanky, E., Zahlsen, K., Spigset, O. & Carlsen, S. M. Placental passage of metformin in women with polycystic ovary syndrome. *Fertil Steril* **83**, 1575–1578 (2005).

286. Charles, B. G. *et al.* Metformin crosses the placenta: A modulator for fetal insulin resistance? *Br Med J* **327**, 880–881 (2004).

287. Lee, N. *et al.* Organic Cation Transporter 3 Facilitates Fetal Exposure to Metformin during Pregnancy. *Mol Pharmacol* **94**, 1125–1131 (2018).

288. Syal, C. *et al.* Ectopic expression of aPKC-mediated phosphorylation in p300 modulates hippocampal neurogenesis, CREB binding and fear memory differently with age. *Sci Rep* **8**, 1–9 (2018).

289. Gouveia, A. *et al.* The aPKC-CBP Pathway Regulates Adult Hippocampal Neurogenesis in an Age-Dependent Manner. *Stem Cell Reports* **7**, 719–734 (2016).

290. UniProt. https://www.uniprot.org.

291. He, L. *et al.* Activation of the cAMP-PKA pathway Antagonizes Metformin Suppression of Hepatic Glucose Production. *J Biol Chem* **291**, 10562 (2016).

292. Wang, F. & Marshall, C. B. Cellular and Molecular Life Sciences Transcriptional/epigenetic regulator CBP/p300 in tumorigenesis: structural and functional versatility in target recognition. *Cell. Mol. Life Sci* **70**, 3989–4008 (2013).

293. McGinnis, C. S. *et al.* MULTI-seq: sample multiplexing for single-cell RNA sequencing using lipid-tagged indices. *Nat Methods* **16**, 619–626 (2019).

294. Bolger, A. M., Lohse, M. & Usadel, B. Trimmomatic: a flexible trimmer for Illumina sequence data. *Bioinformatics* **30**, 2114–2120 (2014).

295. Trapnell, C. *et al.* The dynamics and regulators of cell fate decisions are revealed by pseudotemporal ordering of single cells. *Nat Biotechnol* **32**, 381–386 (2014).

296. Yuzwa, S. A. *et al.* Developmental Emergence of Adult Neural Stem Cells as Revealed by Single-Cell Transcriptional Profiling. *Cell Rep* **21**, 3970–3986 (2017).

297. Loo, L. *et al.* Single-cell transcriptomic analysis of mouse neocortical development. *Nat Commun* **10**, 1–11 (2019).

298. Terao, A., Greco, M. A., Davis, R. W., Heller, H. C. & Kilduff, T. S. Region-specific changes in immediate early gene expression in response to sleep deprivation and recovery sleep in the mouse brain. *Neuroscience* **120**, 1115–1124 (2003).

299. Corbett, B. F. *et al.* ΔFosB Regulates Gene Expression and Cognitive Dysfunction in a Mouse Model of Alzheimer's Disease. *Cell Rep* **20**, 344–355 (2017).

300. Joo, J. Y., Schaukowitch, K., Farbiak, L., Kilaru, G. & Kim, T. K. Stimulus-specific combinatorial functionality of neuronal c-fos enhancers. *Nat Neurosci* **19**, 75–83 (2015).

301. Vogel, A. P., Tsanas, A. & Scattoni, M. L. Quantifying ultrasonic mouse vocalizations using acoustic analysis in a supervised statistical machine learning framework. *Sci Rep* **9**, 1–10 (2019).

302. Qian, X. *et al.* Timing of CNS cell generation: A programmed sequence of neuron and glial cell production from isolated murine cortical stem cells. *Neuron* **28**, 69–80 (2000).

303. Wang, J. *et al.* CBP Histone Acetyltransferase Activity Regulates Embryonic Neural Differentiation in the Normal and Rubinstein-Taybi Syndrome Brain. *Dev Cell* **18**, 114–125 (2010).

304. Jovic, D. *et al.* Single-cell RNA sequencing technologies and applications: A brief overview. *Clin Transl Med* **12**, (2022).

305. Bergen, V., Lange, M., Peidli, S., Wolf, F. A. & Theis, F. J. Generalizing RNA velocity to transient cell states through dynamical modeling. *Nat Biotechnol* **38**, 1408–1414 (2020).

306. Ishii, S. & Hashimoto-Torii, K. Impact of prenatal environmental stress on cortical development. *Frontiers in Cellular Neuroscience* vol. 9 Preprint at https://doi.org/10.3389/fncel.2015.00207 (2015).

307. Thompson, B. L., Levitt, P. & Stanwood, G. D. Prenatal exposure to drugs: effects on brain development and implications for policy and education. *Nat Rev Neurosci* **10**, 303 (2009).

308. Sokolowski, K., Falluel-Morel, A., Zhou, X. & DiCicco-Bloom, E. Methylmercury (MeHg) elicits mitochondrial-dependent apoptosis in developing hippocampus and acts at low exposures. *Neurotoxicology* **32**, 535–544 (2011).

309. Falluel-Morel, A. *et al.* Developmental mercury exposure elicits acute hippocampal cell death, reductions in neurogenesis, and severe learning deficits during puberty. *J Neurochem* **103**, 1968–1981 (2007).

310. Sokolowski, K. *et al.* Neural stem cell apoptosis after low-methylmercury exposures in postnatal hippocampus produce persistent cell loss and adolescent memory deficits. *Dev Neurobiol* **73**, 936–949 (2013).

311. Schafer, S. T. *et al.* Pathological priming causes developmental gene network heterochronicity in autistic subject-derived neurons. *Nat Neurosci* **22**, 243–255 (2019).

312. Radyushkin, K. *et al.* Neuroligin-3-deficient mice: Model of a monogenic heritable form of autism with an olfactory deficit. *Genes Brain Behav* **8**, 416–425 (2009).

313. Bergmann, O., Spalding, K. L. & Frisén, J. Adult Neurogenesis in Humans. *Cold Spring Harb Perspect Biol* **7**, 30–37 (2015).

314. Sanai, N., Berger, M. S., Garcia-Verdugo, J. M. & Alvarez-Buylla, A. Comment on 'human neuroblasts migrate to the olfactory bulb via a lateral ventricular extension'. *Science (1979)* **318**, 1243 (2007).

315. Curtis, M. A. *et al.* Human neuroblasts migrate to the olfactory bulb via a lateral ventricular extension. *Science (1979)* **315**, 1243–1249 (2007).

316. Ernst, A. *et al.* Neurogenesis in the striatum of the adult human brain. *Cell* **156**, 1072–1083 (2014).

317. Zhu, G. *et al.* Pten deletion causes mTorc1-dependent ectopic neuroblast differentiation without causing uniform migration defects. *Development (Cambridge)* **139**, 3422–3431 (2012).

318. Grasselli, C. *et al.* Neural Stem Cells from Shank3-ko Mouse Model Autism Spectrum Disorders. *Mol Neurobiol* **57**, 1502–1515 (2020).

319. Kempermann, G., Jessberger, S., Steiner, B. & Kronenberg, G. Milestones of neuronal development in the adult hippocampus. *Trends Neurosci* **27**, 447–452 (2004).

320. Altman, J. & Das, G. D. Autoradiographic and histological evidence of postnatal hippocampal neurogenesis in rats. *Journal of Comparative Neurology* **124**, 319–335 (1965).

321. Knoth, R. *et al.* Murine features of neurogenesis in the human hippocampus across the lifespan from 0 to 100 years. *PLoS One* **5**, (2010).

322. Mathews, K. J. *et al.* Evidence for reduced neurogenesis in the aging human hippocampus despite stable stem cell markers. *Wiley Online Library* **16**, 1195–1199 (2017).

323. Spalding, K. *et al.* Dynamics of hippocampal neurogenesis in adult humans. *Cell* **153**, 1219–1227 (2013).

324. Stephenson, D. T. *et al.* Histopathologic characterization of the BTBR mouse model of autistic-like behavior reveals selective changes in neurodevelopmental proteins and adult hippocampal neurogenesis. *Mol Autism* **2**, 7 (2011).

325. Amiri, A. *et al.* Pten deletion in adult hippocampal neural stem/progenitor cells causes cellular abnormalities and alters neurogenesis. *J Neurosci* **32**, 5880–5890 (2012).

326. Matsuzaki, F. & Shitamukai, A. Cell division modes and cleavage planes of neural progenitors during mammalian cortical development. *Cold Spring Harb Perspect Biol* **7**, (2015).

327. Polioudakis, D. *et al.* A Single-Cell Transcriptomic Atlas of Human Neocortical Development during Mid-gestation. *Neuron* **103**, 785–801 (2019).

328. Caruso, A., Ricceri, L. & Scattoni, M. L. Ultrasonic vocalizations as a fundamental tool for early and adult behavioral phenotyping of Autism Spectrum Disorder rodent models. *Neurosci Biobehav Rev* **116**, 31–43 (2020).

329. Sungur, A. Ö., Schwarting, R. K. W. & Wöhr, M. Early communication deficits in the Shank1 knockout mouse model for autism spectrum disorder: Developmental aspects and effects of social context. *Autism Research* **9**, 696–709 (2016).

330. Fröhlich, H., Rafiullah, R., Schmitt, N., Abele, S. & Rappold, G. A. Foxp1 expression is essential for sex-specific murine neonatal ultrasonic vocalization. *Hum Mol Genet* **26**, 1511–1521 (2017).

331. Fujita, E., Tanabe, Y., Imhof, B. A., Momoi, M. Y. & Momoi, T. Cadm1-Expressing Synapses on Purkinje Cell Dendrites Are Involved in Mouse Ultrasonic Vocalization Activity. *PLoS One* **7**, (2012).

332. Moy, S. S. *et al.* Mouse Behavioral Tasks Relevant to Autism: Phenotypes of Ten Inbred Strains. *Behavioural brain research* **176**, 4–20 (2007).

333. Chih, B., Afridi, S. K., Clark, L. & Scheiffele, P. Disorder-associated mutations lead to functional inactivation of neuroligins. *Hum Mol Genet* **13**, 1471–1477 (2004).

334. Dahlhaus, R. *et al.* Overexpression of the cell adhesion protein neuroligin-1 induces learning deficits and impairs synaptic plasticity by altering the ratio of excitation to inhibition in the hippocampus. *Hippocampus* **20**, 305–322 (2010).

335. Lieberwirth, C., Pan, Y., Liu, Y., Zhang, Z. & Wang, Z. Hippocampal Adult Neurogenesis: Its Regulation And Potential Role In Spatial Learning And Memory. *Brain Res* **1644**, 127 (2016).

336. Wu, Z. *et al.* Gating TrkB switch by methylglyoxal enables GLO1 as a target for depression. *bioRxiv* (2018) doi:10.1101/435867.

337. Yang, G. *et al.* A Glo1-Methylglyoxal Pathway that Is Perturbed in Maternal Diabetes Regulates Embryonic and Adult Neural Stem Cell Pools in Murine Offspring. *Cell Rep* **17**, 1022–1036 (2016).

338. Myers, G. J., Davidson, P. W. & Strain, J. J. Nutrient and Methyl Mercury Exposure from Consuming Fish. *J Nutr* **137**, 2805–2808 (2007).

339. Bradley, M. A., Barst, B. D. & Basu, N. A review of mercury bioavailability in humans and fish. *Int J Environ Res Public Health* **14**, (2017).

340. Tikhonov, C. *et al.* Regionally representative hair mercury levels in Canadian First Nations adults living on reserves. *Can J Public Health* **112**, 97–112 (2021).

341. Schartup, A. T. *et al.* Climate change and overfishing increase neurotoxicant in marine predators. *Nature* **572**, 648–650 (2019).

Appendix

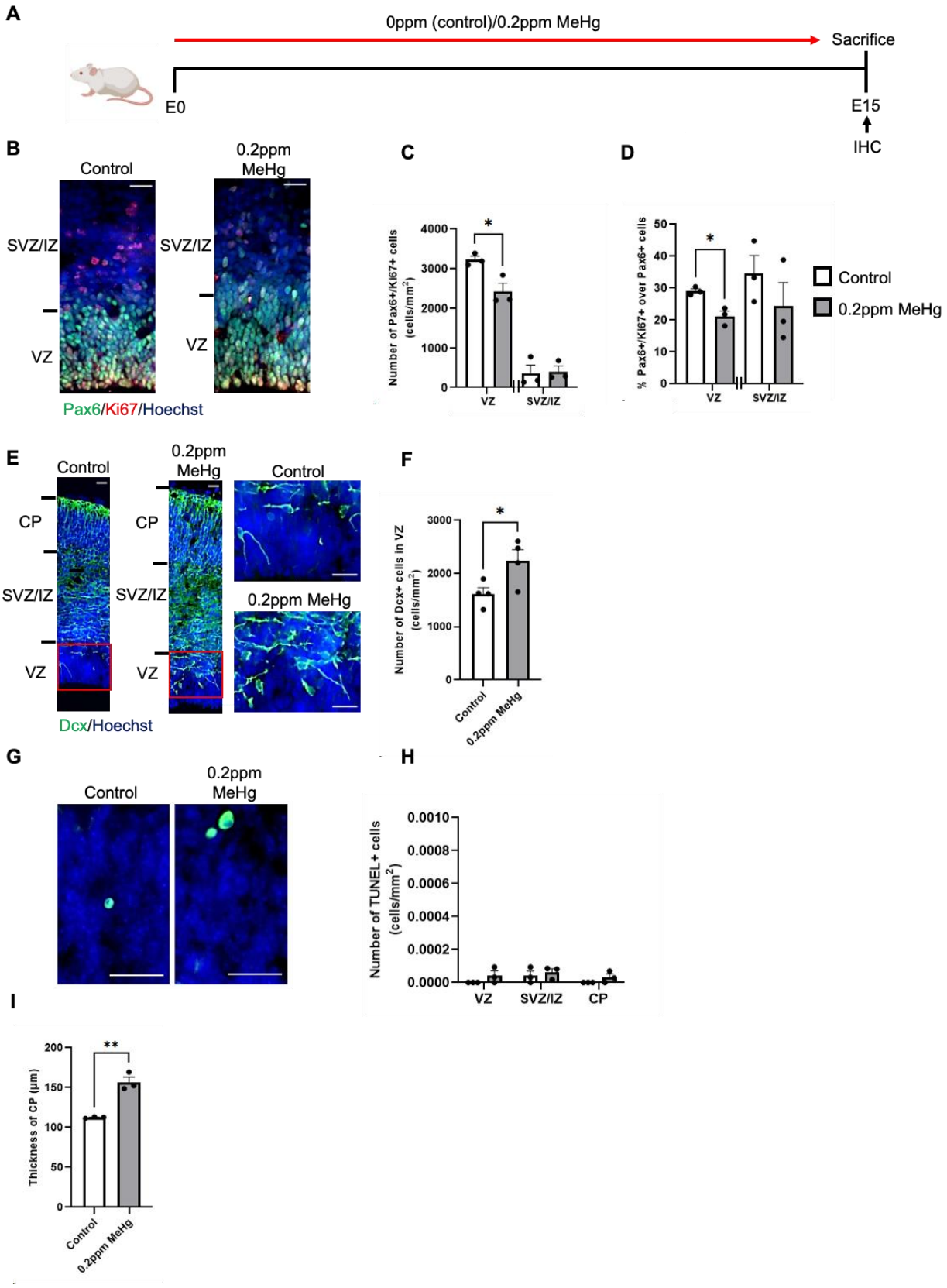
A
0ppm (control)/0.2ppm MeHg
Sacrifice
E0
E15
IHC
B
Control
0.2ppm MeHg
SVZ/IZ
VZ
Pax6/Ki67/Hoechst
C
Number of Pax6+/Ki67+ cells (cells/mm2)
VZ
SVZ/IZ
D
% Pax6+/Ki67+ over Pax6+ cells
Control
0.2ppm MeHg
E
CP
SVZ/IZ
VZ
Dcx/Hoechst
F
Number of Dcx+ cells in VZ (cells/mm2)
G
H
Number of TUNEL+ cells (cells/mm2)
CP
I
Thickness of CP (μm)

Appendix Figure 1. Prenatal exposure to MeHg increases neuronal differentiation of cortical precursors at the expense of their proliferation. (A) Schematic of prenatal exposure to MeHg in pregnant mice, created with BioRender.com. 0ppm (control) and 0.2ppm MeHg were administered through drinking water to pregnant mice starting at E0 until E15. At E15, brains were collected for immunohistochemistry. (B, E) Images of E15 cerebral cortex sections from embryos receiving 0ppm and 0.2ppm MeHg treatment, immunostained for Pax6 (B, green), and Ki67 (B, red) and counterstained for Hoechst (blue). Scale bar: 25 µm. (C-D) Quantitative analysis of the number and proportion of $Ki67^{+}/Pax6^{+}$ proliferating cortical precursors within VZ and SVZ/IZ, determined from sections similar to those shown in (B). n=3 embryos/group, student t-test * $p<0.05$. (G) Images of E15 cerebral cortex sections from embryos receiving 0ppm and 0.2ppm MeHg treatment, immunostained for DCX (E, green) and counterstained for Hoechst (blue). Scale bar: 25 µm. (F) Quantitative analysis of the number of DCX^{+} immature neurons within VZ, determined from sections similar to those shown in (E). n=4 embryos/group, student t-test, * $p<0.05$. (G) Images of E15 cerebral cortex sections from embryos receiving 0ppm and 0.2ppm MeHg treatment were detected for TUNEL+ cells (green), and counterstained for Hoechst (blue). Scale bar: 25 µm. (H) Quantitative analysis of the number of TUNEL+ cells within VZ, SVZ/IZ, and CP, determined from sections similar to those shown in (G). (I) Quantitative analysis of thickness for the CP was determined from coronal sections similar to those shown in (E). n=3 embryos/group, student t-test, ** $p<0.01$. Error bars indicate the SEM.

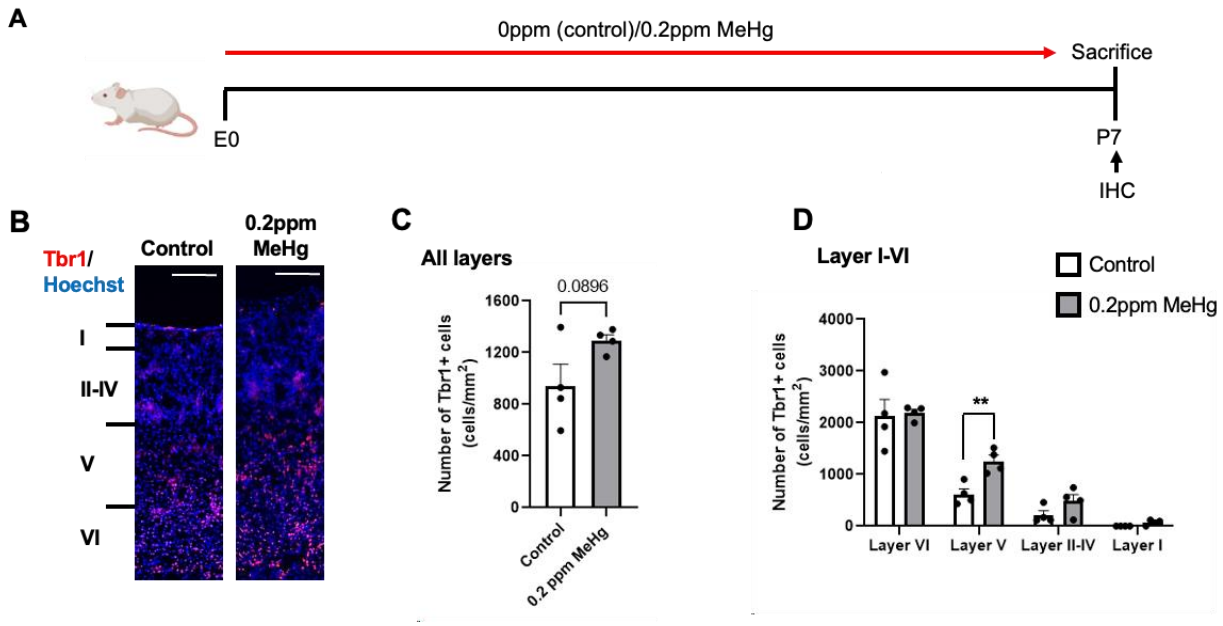

Appendix Figure 2. Perinatal exposure to MeHg increases the genesis of deep-layer cortical neurons *in vivo*. (A) Schematic of perinatal exposure to MeHg in pregnant mice, created with BioRender.com. 0ppm (control) and 0.2ppm MeHg were administered through drinking water to pregnant mice starting at E0 until P7. At P7, brains were collected for immunohistochemistry Images of P7 cerebral cortex sections from pups receiving 0ppm and 0.2ppm MeHg treatment since E0, immunostained for Tbr1 (B, red) and counterstained for Hoechst (blue). Scale bar: 50 µm. (C-D) Quantitative analysis of the number of $Tbr1^+$ deep layer neurons (layer I-layer VI), determined from sections similar to those shown in (B). n=4 animals/group, student t-test, ** $p<0.01$. Error bars indicate the standard error of the mean (SEM).